Title	Temperature dependence of spin-dependent tunneling conductance of magnetic tunnel junctions with half-metallic Co2MnSi electrodes
Author(s)	胡, 兵
Degree Grantor	北海道大学
Degree Name	博士(工学)
Dissertation Number	甲第12484号
Issue Date	2016-12-26
DOI	https://doi.org/10.14943/doctoral.k12484
Doc URL	https://hdl.handle.net/2115/64456
Type	doctoral thesis
File Information	Hu_Bing.pdf

Temperature dependence of spin-dependent tunneling conductance of magnetic tunnel junctions with half-metallic Co_2MnSi electrodes

Bing Hu

Division of Electronics for Informatics
Graduate School of Information Science and Technology
Hokkaido University

December 2016

Abstract

Spintronic devices, which utilize the spin degree of freedom in addition to the charge of the electron, have attracted much interest as future-generation electron devices. This is because of their potential advantages of nonvolatility, decreased power consumption, and reconfigurable logic function capabilities. Half-metallic ferromagnets (HMFs) are one of the most suitable spin source materials because of their complete spin polarization (P) at the Fermi level (E_F) arising from an energy gap for one spin direction. Co-based Heusler alloys (Co_2YZ, where Y is usually a transition metal and Z is a main group element) are among the most extensively applied to spintronic devices. This is because of the HMF nature theoretically predicted for many of these alloys and because of their high Curie temperatures, which are well above room temperature.

Co_2MnSi (CMS) is one of the most extensively investigated ferromagnetic electrode materials among the Co_2YZ family. This is because of its theoretically predicted half-metallic nature with a large half-metal gap of 0.81 eV for its minority-spin band and its high Curie temperature of 985 K. Liu *et al*. from our research group demonstrated giant tunneling magnetoresistance (TMR) ratios of up to 1995% at 4.2 K and up to 354% at 290 K for CMS/MgO/CMS (CMS MTJs) having Mn-rich CMS electrodes and up to 2610% at 4.2 K and 429% at 290 K for Co_2(Mn,Fe)Si (CMFS)/MgO/CMFS MTJs (CMFS MTJs) with Mn-rich, lightly Fe-doped CMFS electrodes.

To take full advantage of the half-metallic nature of Co-based Heusler alloys as spin source materials at room temperature, it is important to clarify the origin of the temperature (T) dependence of spin-dependent tunneling conductance (G) of MTJs. The T dependence of G for the parallel and antiparallel magnetization alignments, G_P and G_{AP}, of MTJs has been discussed on the basis of models proposed by Zhang *et al*. and by Shang *et al*. Zhang *et al*. accounted for the T dependence of G_P and G_{AP} by spin-flip inelastic tunneling via a thermally excited magnon while assuming a T-independent P, and predicted that both G_P and G_{AP} increase with increasing T. On the other hand, Shang *et al*. took into consideration only spin-conserving elastic tunneling with a decaying P with increasing T. The Shang model predicts that G_{AP} increases with T, of which the effect on $G_{AP}(T)$ is apparently in agreement with that of the Zhang model. However, note that the tunneling mechanisms that determine the T dependence are intrinsically different

between these two models. On the other hand, the Shang model predicts that G_{P} decreases, which is opposed to the prediction of the Zhang model. Thus, a more systematic experimental study is essential to get a deeper understanding of the origin of the T dependence of spin-dependent G_{P} and G_{AP}.

A promising approach would be to investigate half-metal-based MTJs with systematically varied P values at 0 K, as MTJs with highly spin-polarized electrodes arising from half-metallicity would show most typical T dependence of G_{P} and G_{AP}. In addition, it is a particularly desirable approach to extract how the T dependence of G_{P} and G_{AP} changes with P at 0 K by investigating a series of high-quality MTJs with systematically varied P at 0 K. Furthermore, development of a more comprehensive model for the T dependence of G_{P} and G_{AP} is requisite as the predictions of the Zhang and Shang models for $G_{\mathrm{P}}(T)$ are opposite. This difference in the predictions also suggests that an analysis of the experimental $G_{\mathrm{P}}(T)$ would be critical to revealing the origin of the T dependence of spin-dependent G.

The purpose of this research is to elucidate the origin of the T dependence of G_{P} and G_{AP} of MTJs through analyzing the experimental $G_{\mathrm{P}}(T)$ and $G_{\mathrm{AP}}(T)$ of high-quality MTJs showing giant TMR ratios and to provide a unified picture of how the T dependence of G_{P} and G_{AP} changes with P. To do so, we experimentally investigated the T dependences of G_{P} and G_{AP} of CMS MTJs having systematically varied spin polarizations at 4.2 K by varying the Mn composition α in $\mathrm{Co_2Mn_{\alpha}Si}$ electrodes. Notable features in $G_{\mathrm{P}}(T)$ were found; i.e., it decreased with increasing T from T_1 of about 30 K to T_2 ranging from about 162 K to 237 K depending on α; then it increased for T over T_2. Furthermore, as P at 4.2 K increased, T_2 increased and the maximum decrease in the normalized G_{P} [1] at T_2 increased. To clarify the origin of the characteristic T dependence of G_{P}, we developed a model that took into account both spin-conserving elastic tunneling in which P decays with increasing T and spin-flip inelastic tunneling via a magnon by extending the original Zhang model.

This dissertation consists of five chapters and the main content of each chapter is as follows:

Chapter 1 introduces the background, purpose and approach of the present study.

Chapter 2 describes our experimental methods, including the preparation of MTJs, the estimation of the barrier height, and the measurement of the T dependence of spin-dependent tunneling conductance.

Chapter 3 presents the results and discussion for the T dependence of spin-dependent tunneling conductance of CMS MTJs. At first, it describes the overall features of $G_P(T)$ and $G_{AP}(T)$ of CMS MTJs with various α values that showed a high TMR ratio. Then, it describes the notable, nonmonotonic T dependence of $G_P(T)$ of CMS MTJs that exhibited a giant TMR ratio. It also describes how the $G_P(T)$ changed with P at 4.2 K. To explain these features of $G_P(T)$, we devised an extension of the original Zhang model, in which only spin-flip inelastic tunneling was considered as the origin of the T dependence of G_P and $G_{AP,}$ by introducing a T-dependent P. By analyzing these features of the $G_P(T)$ with the extended Zhang model, it was revealed that both spin-flip inelastic tunneling via a magnon and spin-conserving elastic tunneling wherein P decreases with increasing T play key roles. Finally, the experimental $G_{AP}(T)$, including its stronger T dependence for higher P at 4.2 K, was also consistently explained with the extended Zhang model.

Chapter 4 describes the results of the T dependence of G_P and G_{AP} of CMFS MTJs with $Co_2Mn_{\alpha'}Fe_{\beta'}Si_{0.84}$ electrodes having a fixed Mn composition of $\alpha' = 0.73$ and various Fe compositions of β' ranging from 0 to 0.62. We found that the magnon lower cut-off energy, E_c^P and E_c^{AP}, of (Mn + Fe)-rich CMFS MTJs with the Fe compositions, β', being comparable to α', i.e., CMFS with ($\beta' = 0.57$, $\alpha' + \beta' = 1.30$) and ($\beta' = 0.62$, $\alpha' + \beta' = 1.35$), were larger than those of Mn-rich CMS MTJs with $Co_2Mn_\alpha Si_{0.84}$ electrodes with $\alpha = 1.30$. Thus, it was revealed that the magnon lower cut-off energy, which influences the T dependence of the TMR ratio, depends on the constituent transition-metal element Y in half-metallic Co_2YSi Heusler alloys.

Chapter 5 summarizes and concludes this dissertation.

In summary, it was clarified that both spin-flip inelastic tunneling via a thermally excited magnon and spin-conserving elastic tunneling in which P decays with increasing T play key roles as the origins of the T dependence of the spin-dependent tunneling conductance of MTJs. Our findings provide a unified picture for understanding the origin of the T dependence of G of MTJs with a wide range of P, including MTJs with high P close to a half-metallic value.

Content

Abstract .... **III**

1. Introduction **1**

1.1. Background 1
1.1.1. Spintronics 1
1.1.2. Magnetic tunnel junctions 2
1.1.3. Highly spin-polarized spin source 4
1.1.3.1. Half-metallic ferromagnets 6
1.1.3.2. Co-based Heusler alloys 7
1.1.4. Temperature dependence of spin-dependent tunneling conductance of magnetic tunnel junctions 11
1.2. Purpose 16
1.3. Approach 16

2. Experimental Methods **19**

2.1. Preparation of the magnetic tunnel junctions 19
2.1.1. Layer structure 19
2.1.2. Device fabrication process 22
2.2. Tunneling magnetoresistance characteristics 24
2.3. Estimation of the MgO barrier height 26
2.4. Measurement of temperature dependence of spin-dependent tunneling conductance 27

3. Results and discussion on the temperature dependence of spin-dependent tunneling conductance of magnetic tunnel junctions with Co_2MnSi electrodes **29**

3.1. Overall features of the temperature dependence of spin-dependent tunneling conductance 29
3.2. Temperature dependence of spin-dependent tunneling conductance for parallel alignment 36
3.2.1. Theoretical model for analysis 36

3.2.2. Analysis and discussion 39
3.2.3. Influence of smearing of the Fermi distribution function . 45
3.2.4. Summary 50
3.3. Temperature dependence of spin-dependent tunneling conductance for antiparallel alignment 51
3.3.1. Theoretical model for analysis 51
3.3.2. Analysis and discussion 52
3.3.3. Summary 60

4. Temperature dependence of spin-dependent tunneling conductance of magnetic tunnel junctions with Co_2(Mn,Fe)Si electrodes 61
4.1. Motivation 61
4.2. Temperature dependence of spin-dependent tunneling conductance of magnetic tunnel junctions with $Co_2Mn_{0.73}Fe_{\beta'}Si_{0.84}$ electrodes . 63
4.2.1. Layer structure 63
4.2.2. Experimental results 64
4.2.3. Analysis and discussion 66
4.3. Effect of MgO tunnel barrier thickness on the temperature dependence of G_P and G_{AP} of high-quality MTJs 75
4.3.1. Experimental results 75
4.3.2. Analysis and discussion 78
4.4. Summary 82

5. Conclusion 83

Acknowledgements 85

Reference 87

Appendix 93

Chapter 1

Introduction

1.1. Background

1.1.1. Spintronics

Spintronics, which is based on a novel device concept of utilizing the spin degree of freedom in addition to the charge of the conduction electrons, has attracted much interest recently. This is because of their potential advantages of nonvolatility, high-speed operation, low power consumption, and reconfigurable logic function capabilities [1,2]. One of the typical spintronic devices is a magnetoresistive random access memory (MRAM), which features nonvolatility along with high-speed operation and unlimited read/write endurance. Thus, MRAMs are highly expected as future-generation high-performance nonvolatile memories. An MRAM cell consists of a magnetic tunnel junction (MTJ) and a transistor. Products of 256Mb MRAM with perpendicular MTJs (pMTJs) and spin-transfer-torque technology (STT-MRAM) have been recently developed.

A highly efficient spin source is essential for constructing spintronic devices. Half-metallic ferromagnets (HMFs) are one of the most suitable spin source materials because of their complete spin polarization at the Fermi level (E_F) arising from an energy gap for one spin direction (mostly the minority-spin band) [3]. Co-based Heusler alloys (Co_2YZ, where Y is usually a transition metal and Z is a main group element) [4] are among the most extensively applied to spintronic devices, including MTJs [5-17] and giant magnetoresistance (GMR) devices [18-22], and for spin injection into semiconductors [23-27]. This is because of the HMF nature theoretically predicted for many of these alloys [28-31] and because of their high Curie temperatures, which are well above room temperature (RT) [32].

1.1.2. Magnetic tunnel junctions

The most extensive applications of spintronic devices have been done for MTJs. Indeed, MTJs have been applied for nonvolatile, high-speed MRAMs, magnetic read heads of hard disk drives, and highly sensitive magnetic-field sensors. Highly spin-polarized ferromagnetic electrodes are critical to obtaining high-performance spintronic devices, including MTJs. A basic MTJ layer structure consists of two ferromagnetic electrodes sandwiching an ultrathin insulating layer as illustrated in Fig. 1.1 (a). When the insulator layer is thin enough (a few nanometers), a quantum phenomenon that electrons can tunnel through the potential barrier will occur, resulting in electrical conduction. The tunneling conductance ($G = I/V$) of an MTJ depends on the relative magnetization configuration between the two electrodes, resulting in that G for parallel alignment, G_{P}, is larger than that for antiparallel alignment, G_{AP}, which is called the tunnel magnetoresistance (TMR) effect (Fig. 1.1). This is because, according to the Julliere model for the TMR effect [33] in which the tunneling matrix elements from $\boldsymbol{k}$ to $\boldsymbol{k'}$ are assumed to be constant for any $\boldsymbol{k}$ and $\boldsymbol{k'}$ where $\boldsymbol{k}$ to $\boldsymbol{k'}$ are the wave vectors of the incident and transmitted electron states, when both temperature (T) and bias voltage (V) are close to 0, the G_{P} and G_{AP} showed a correlation with the spin-dependent density of states at the Fermi level (E_{F}) of these two ferromagnetic electrodes as

$$G_{\mathrm{P}} \propto \rho_{\mathrm{M1}} \cdot \rho_{\mathrm{M2}} + \rho_{\mathrm{m1}} \cdot \rho_{\mathrm{m2}}, \qquad (1.1)$$

$$G_{\mathrm{AP}} \propto \rho_{\mathrm{M1}} \cdot \rho_{\mathrm{m2}} + \rho_{\mathrm{m1}} \cdot \rho_{\mathrm{M2}}, \qquad (1.2)$$

where ρ_{M} and ρ_{m} are the majority-spin and minority-spin density of states (DOS) at E_{F} while the subscript 1 and 2 represent the emitter (electrode 1) and collector (electrode 2), respectively.

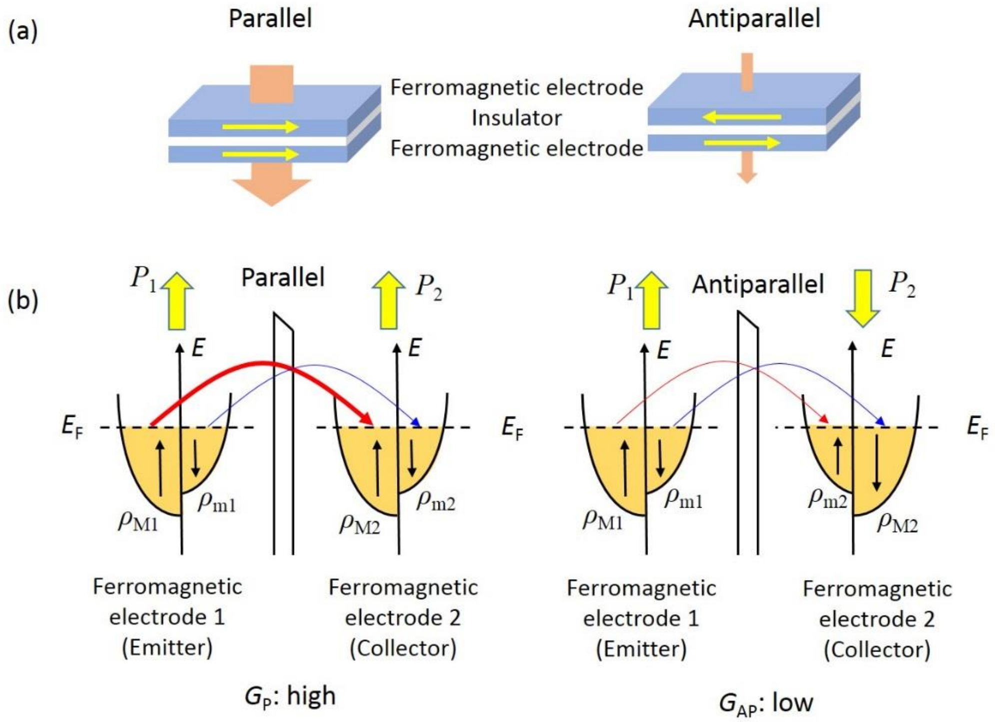

Fig. 1.1. (a) Schematic of a magnetic tunnel junction which consists of two ferromagnetic electrodes sandwiching an ultrathin insulating layer. The tunneling conductance (G) of an MTJ depends on the relative magnetization configuration between the two ferromagnetic electrodes. (b) Schematic of the spin-dependent density-of-states for the ferromagnetic electrodes. The tunneling conductance is the highest for the parallel alignment and the lowest for the antiparallel alignment.

As an important parameter for the evaluation of the performance of an MTJ, the TMR ratio is defined by the following equation:

$$\mathrm{TMR\,ratio} = \frac{G_{\mathrm{P}} - G_{\mathrm{AP}}}{G_{\mathrm{AP}}} = \frac{R_{\mathrm{AP}} - R_{\mathrm{P}}}{R_{\mathrm{P}}}, \qquad (1.3)$$

where G_{P} (R_{P}) and G_{AP} (R_{AP}) are the tunneling conductances (resistances) for the parallel and antiparallel magnetization alignments between these two electrodes. According to the Julliere model, the TMR ratio is expressed using the spin polarizations, P_1 and P_2, at E_{F} of the two ferromagnetic electrodes as

$$\mathrm{TMR\,ratio} = \frac{2P_1P_2}{1-P_1P_2}, \qquad (1.4)$$

where the spin polarization at E_{F}, P, is defined with ρ_{M} and ρ_{m} as

$$P = \frac{\rho_{\mathrm{M}} - \rho_{\mathrm{m}}}{\rho_{\mathrm{M}} + \rho_{\mathrm{m}}}. \qquad (1.5)$$

Equation 1.4 suggested that a highly spin-polarized ferromagnetic electrode is essential for obtaining high TMR ratios or good device performance.

In the Julliere model, the wave-vector dependence of the tunneling probability is ignored as described above. However, it is highly important in single-crystalline MTJs. The transversal crystal momentum is conserved for tunneling in single-crystalline MTJs, which is called coherent tunneling [34]. Due to the coherent tunneling nature, the tunneling probability is dependent on the transversal crystal momentum for electrons with the same total energy, E. Electrons that have a smaller transversal kinetic energy with a given total energy E show the higher tunneling probability. Due to the coherent tunneling, the tunneling probability is strongly influenced by the symmetry of the wave function of the tunneling electron for single-crystalline, epitaxial MTJs.

The electron energy E in the emitter electrode consists of two terms, i.e., the kinetic energy perpendicular to the plane, $\hbar^2 k_z^2/2\mathrm{m}^*$, and the transversal kinetic energy parallel to the plane, $\hbar^2 k_\parallel^2/2\mathrm{m}^*$,

$$E = \frac{\hbar^2 k_z^2}{2m^*} + \frac{\hbar^2 k_\parallel^2}{2m^*}. \qquad (1.6)$$

On the other hand, the electron energy E in the barrier consists of the following three terms:

$$E = V_b - \frac{\hbar^2 \kappa^2}{2m^*} + \frac{\hbar^2 k_\parallel^2}{2m^*}, \qquad (1.7)$$

where $E - V_{\mathrm{b}} < 0$, V_{b} is the barrier height measured from the bottom of the conduction band in the emitter (Fig. 1.2), $-\hbar^2\kappa^2/2m^* < 0$ is the negative kinetic energy in the barrier. Due to the conservation of the transversal kinetic energy in coherent tunneling, the transversal kinetic energy $\hbar^2 k_{\parallel}^2/2m^*$ in the barrier is equal to that in the emitter electrode. Then, the effective barrier height, V_{eff}, which is the energy difference from the bottom of the conduction band of the barrier to E_F of the emitter, is given as

$$V_{\mathrm{eff}} = V_b - \frac{\hbar^2 k_z^2}{2m^*} = V_b - E + \frac{\hbar^2 k_{\parallel}^2}{2m^*}. \qquad (1.8)$$

Thus, the effective barrier height is lower for the smaller transversal kinetic energy for a given total energy E in the emitter, resulting in a higher tunneling probability. This is a key point for coherent tunneling. Equivalently, Eq. (1.7) indicates the decaying factor κ (> 0) of the wave function $\psi(z) \sim e^{-\kappa z}$ in the barrier becomes smaller for the smaller transversal kinetic energy for the given E and V_b, resulting in a higher tunneling probability. For example, the magnitude relative relation in the transversal crystal momentum $k_{\parallel}$ of electrons in single-crystalline Fe is as follows,

$$k_{\parallel}(\Delta_1) << k_{\parallel}(\Delta_5) << k_{\parallel}(\Delta_2), k_{\parallel}(\Delta_{2'}).$$

The tunneling probability of the electron having Δ_1 symmetry is relatively high. In contrast, the tunneling probability of the electron having Δ_5, Δ_2 or $\Delta_{2'}$ symmetries is several orders lower. The Δ_1 symmetry exists at E_F of the majority-spin band, while it doesn't exist at E_F of the minority-spin band. This results in a high tunnel conductance for the parallel magnetization configuration, while a significantly lower tunnel conductance for the antiparallel configuration, leading a high TMR ratio.

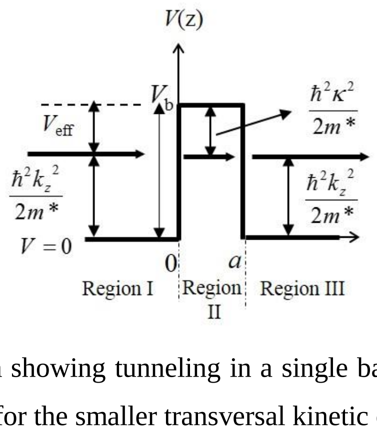

Fig. 1.2. Schematic diagram showing tunneling in a single barrier structure. The effective barrier height, V_{eff}, is lower for the smaller transversal kinetic energy, $\hbar^2 k_{\parallel}^2/2m^*$, for a given total energy E in the emitter, resulting in a higher tunneling probability.

1.1.3. Highly spin-polarized spin source

1.1.3.1. Half-metallic ferromagnets

As discussed in the former sections, a highly efficient spin source is essential for constructing spintronic devices. Half-metallic ferromagnets (HMFs) are one of the most suitable spin source materials because of their complete spin polarization at the Fermi level (E_F) arising from the existence of an energy gap for one spin direction (mostly the minority-spin band), as shown in Fig. 1.3. The concept of half-metallic ferromagnet was first introduced by de Groot *et al*. for a half-Heusler alloy NiMnSb by first-principles calculations [3].

After that, half-metallic nature was predicted for several materials, such as Co-based full-Heusler alloys (Co_2YZ, where Y is usually a transition metal and Z is a main group element) [28-31], (La,Ca)MnO_3 [35], and so on. However, the low Curie temperature around room temperature of (La,Ca)MnO_3 makes it unsuitable for the practical applications. Different from that, many of Co-based Heusler alloys feature relatively high Curie temperatures, thus they attracted much interest.

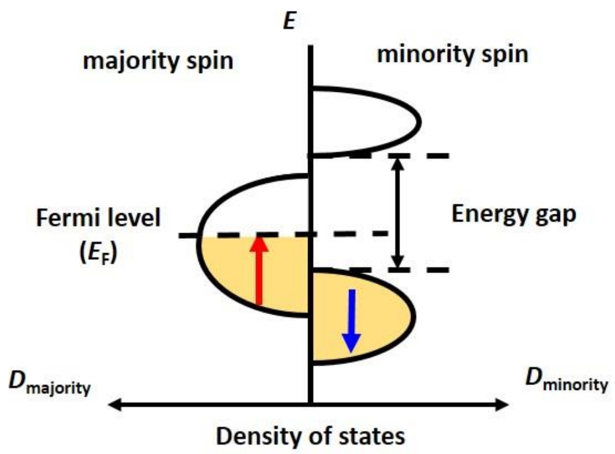

Fig. 1.3. Schematic of the spin-dependent density of states of a half-metallic ferromagnet (HMF) which shows 100% spin polarization at E_F.

1.1.3.2. Co-based Heusler alloys

As described in Section 1.1.1, Co-based Heusler alloys (Co_2YZ, where Y is usually a transition metal (such as Fe, Mn, and Cr) and Z is a main group element (such as Si, Ge, Al, and Ga)) [4]are among the most extensively applied to spintronic devices, including MTJs [5-17] and giant magnetoresistance (GMR) devices [18-22], and for spin injection into semiconductors [23-27]. This is because of the HMF nature theoretically predicted for many of these alloys [28-31] and because of their high Curie temperatures, which are well above room temperature [32]. As shown in Fig. 1.4, the $L2_1$ cubic structure is a typical crystal structure for stoichiometric Co_2YZ that it consists of four different fcc sub-lattices, two of which are occupied by Co atoms and the other two by the Y and Z atoms, respectively. The Co atoms are positioned at the positions (1/4,1/4,1/4) and (3/4,3/4,3/4) of the cubic unit cell, while the Y and Z atoms occupy the 4*a* (0,0,0) and 4*b* (1/2,1/2,1/2) positions, respectively.

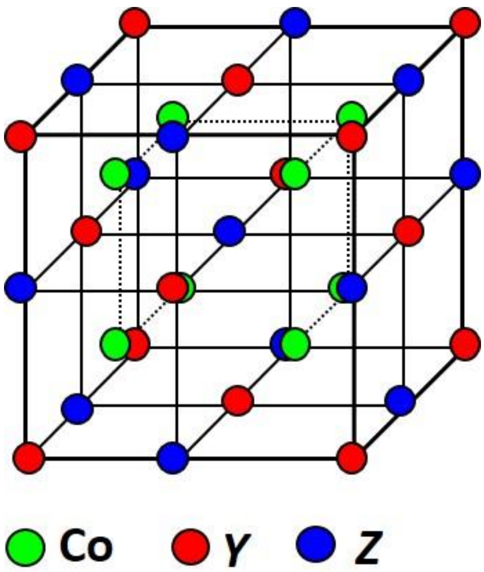

Fig. 1.4. Schematic of the $L2_1$ crystal structure of Co-based Heusler alloy Co_2YZ. The lattice consists of four different fcc sub-lattices, two of which are occupied by Co atoms and the other two by the Y and Z atoms, respectively.

Among the Co_2YZ family, Co_2MnSi (CMS) is one of the most extensively investigated ferromagnetic electrode materials[6-12,18,20,23,26,27,36-48]. This is because of its theoretically predicted half-metallic nature with a large half-metal gap of 0.81 eV for its minority-spin band [30] and its high Curie temperature of 985 K [32]. In practice, to various degrees, off-stoichiometry in Co_2YZ thin films prepared by magnetron sputtering or molecule beam epitaxy is inevitable, leading to structural defects. Picozzi *et al*. predicted from first principles that half-metallicity in CMS and Co_2MnGe (CMG) is lost for Co_{Mn} antisites, where a Mn site is replaced by a Co atom, because of the appearance of minority-spin in gap states near E_F, while half-metallicity is retained for Mn_{Co} antisites, where a Co site is replaced by a Mn atom [36]. The effect of off-stoichiometry on the half-metallicity of CMS and CMG has been systematically investigated recently using various experimental approaches, including the tunneling magnetoresistance (TMR) ratios of MTJs [9-12], the saturation magnetization per formula unit of thin films [12], the surface spin polarization [45], the magnetic states as investigated by x-ray absorption spectroscopy and x-ray magnetic circular dichroism [46,49,50], and the electronic states as investigated through spin-resolved low-energy and hard x-ray photoelectron spectroscopy [47,48,51]. These experimental studies, along with first-principles calculations, demonstrated that Co_{Mn} antisites induced by a Mn-deficient composition (the Mn composition $\alpha < 2 - \beta$ in the composition expression of $Co_2Mn_{\alpha}Si_{\beta}$) are detrimental to the half-metallicity of CMS. Furthermore, it was shown that harmful Co_{Mn} antisites can be suppressed and half-metallicity enhanced by preparing CMS thin films with a Mn-rich composition [9-12]. It was also shown that (Mn + Fe)-rich compositions are critical to suppressing these harmful antisites and to retaining the half-metallic electronic states for Co_2(Mn,Fe)Si (CMFS) quaternary alloys [16,17]. Given these findings, we demonstrated giant TMR ratios of up to 2110% at 4.2 K and up to 366% at 290 K for CoFe-buffered CMS/MgO/CMS MTJs (CMS MTJs) having Mn-rich CMS electrodes and up to 2610% at 4.2 K and 429% at 290 K for CoFe-buffered CMFS/MgO/CMFS MTJs (CMFS MTJs) with Mn-rich, lightly Fe-doped CMFS electrodes [16]. The corresponding film composition dependences of the TMR ratios were shown in Figs. 1.5 (CMS MTJs) and 1.6 (CMFS MTJs of series B in [16]), respectively.

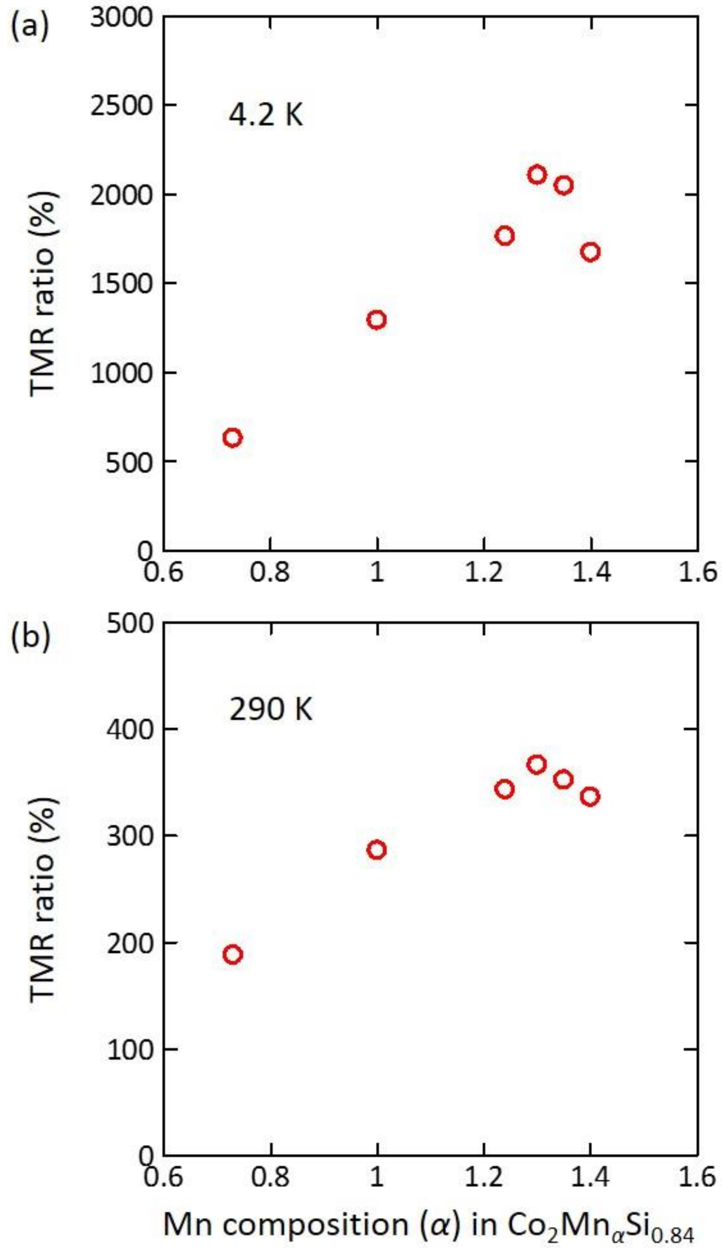

Fig. 1.5. TMR ratios at (a) 4.2 K and (b) 290 K for Co_2MnSi (CMS)/MgO/CMS MTJs (CMS MTJs) as a function of Mn composition α in $Co_2Mn_\alpha Si_{0.84}$ electrodes [16].

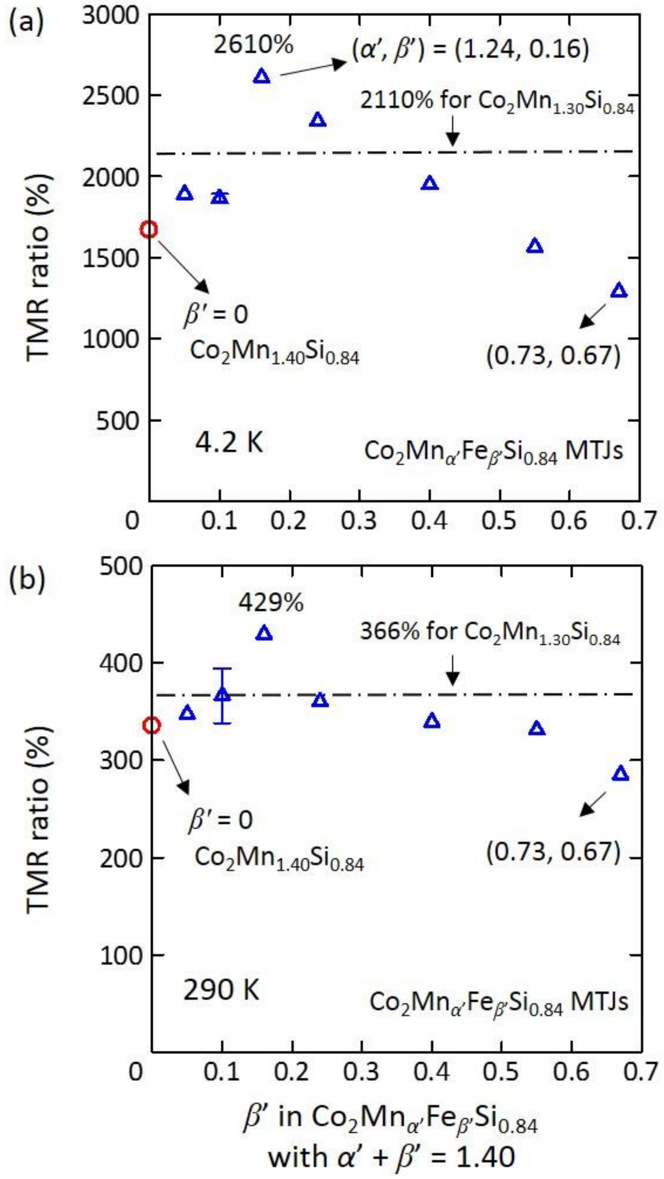

Fig. 1.6. TMR ratios at (a) 4.2 K and (b) 290 K for Co_2(Mn,Fe)Si (CMFS)/MgO/CMFS MTJs (CMFS MTJs) with $Co_2Mn_{\alpha'}Fe_{\beta'}Si_{0.84}$ electrodes as a function of β' ranging from β' = 0 (α' = 1.40) to β' = 0.67 (α' = 0.73) for a fixed $\delta = \alpha' + \beta'$ = 1.40 (CMFS MTJ of series B in [16]). The β' = 0 MTJ corresponds to the $Co_2Mn_{1.40}Si_{0.84}$ MTJ (open red circle). The TMR ratios at 4.2 K and 290 K of $Co_2Mn_{1.30}Si_{0.84}$ MTJ were plotted (dashed lines) for comparison.

1.1.4. Temperature dependence of spin-dependent tunneling conductance of magnetic tunnel junctions

To take full advantage of the half-metallic nature of Co-based Heusler alloys as spin source materials at room temperature, it is important to clarify the origin of the temperature (T) dependence of spin-dependent tunneling conductance (G) of MTJs.

The T dependence of G for the parallel and antiparallel magnetization alignments, G_P and G_{AP}, of MTJs has been discussed on the basis of models proposed by Zhang *et al*. [52] and by Shang *et al*. [53]. Zhang *et al*. accounted for the T dependence of G_P and G_{AP} by spin-flip inelastic tunneling via a thermally excited magnon while assuming a T-independent spin polarization, P [52]. On the other hand, Shang *et al.* took into consideration only the decaying P with increasing T for spin-conserving elastic tunneling, and did not take into account spin-flip inelastic tunneling process.

Thus, according to the original Zhang model, G_P at V = 0 and at finite T is given by the sum of the T-independent spin-conserving elastic tunneling term, $G_{P,el}$, and the T-dependent spin-flip inelastic tunneling term, $G_{P,in}(T)$, and is expressed as

$$G_{\mathrm{P}}(T) = G_{\mathrm{P,el}} + G_{\mathrm{P,in}}(T), \qquad (1.9)$$

$$G_{\mathrm{P,el}} = \frac{4\pi e^2}{\hbar}(|T^d|^2 + 2S^2|T^J|^2)({\rho_{\mathrm{M}}}^2 + {\rho_{\mathrm{m}}}^2), \qquad (1.10)$$

$$G_{\mathrm{P,in}}(T) = \frac{4\pi e^2}{\hbar}\frac{2S}{E_m}|T^J|^2\, k_{\mathrm{B}}T \cdot f(T) \cdot 2\rho_{\mathrm{M}}\rho_{\mathrm{m}}, \qquad (1.11)$$

$$f(T) = -\ln[1 - \exp(-\frac{E_{\mathrm{c}}}{k_{\mathrm{B}}T})], \qquad (1.12)$$

where T^d and T^J are direct and spin-dependent tunneling matrix elements, respectively, S is the spin parameter, $E_m = 3k_BT_C/(S + 1)$, E_c is the lower magnon cutoff energy, k_B is the Boltzmann constant, and T_C is the Curie temperature of the ferromagnetic electrode. In the Zhang model, T^d and T^J are assumed to be independent of the wave vectors of $\boldsymbol{k}$ of the incident wave function and $\boldsymbol{k}$' of the transmitted wave function as in the Julliere model. Thus, $G_{P,el}$ is directly proportional to $\rho_M^2 + \rho_m^2$. This is because the tunneling paths for spin-conserving elastic tunneling in the parallel configuration are from the majority-spin band of the emitter to the majority-spin band of the collector and from the minority-spin band of the emitter to the minority-spin band of the collector. While $G_{P,in}$ due to spin-flip inelastic tunneling is proportional to $2\rho_M\rho_m$. This is because the tunneling paths for spin-flip inelastic tunneling in the parallel configuration are from the majority-spin band of the emitter to the minority-spin band of the collector and from the minority-spin band of the emitter to the majority-spin band of the collector. Schematics of the tunneling processes for the parallel alignment in the Zhang model are shown in Fig. 1.7. Note that spin-dependent density of states at E_F, ρ_M and ρ_m are assumed to be independent of T, and equivalently P is assumed to be independent of T in the original Zhang model.

Similarly, G_{AP} at $V = 0$ and at finite T is given by the sum of the T-independent spin-conserving elastic tunneling term, $G_{AP,el}$, and the T-dependent spin-flip inelastic tunneling term, $G_{AP,in}(T)$, and is expressed as

$$G_{AP}(T) = G_{AP,el} + G_{AP,in}(T), \qquad (1.13)$$

$$G_{AP,el} = \frac{4\pi e^2}{\hbar}(|T^d|^2 + 2S^2|T^J|^2)\cdot 2\rho_M\rho_m, \qquad (1.14)$$

$$G_{AP,in}(T) = \frac{4\pi e^2}{\hbar}\frac{2S}{E_m}|T^J|^2 k_B T\cdot f(T)(\rho_M{}^2 + \rho_m{}^2). \qquad (1.15)$$

$G_{AP,el}$ is proportional to $2\rho_M\rho_m$. This is because the tunneling paths for spin-conserving elastic tunneling in the antiparallel configuration are from the majority-spin band of the emitter to the minority-spin band of the collector and from the minority-spin band of the emitter to the majority-spin band of the collector. While $G_{AP,in}$ due to spin-flip inelastic tunneling is proportional to $\rho_M{}^2 + \rho_m{}^2$. This is because the tunneling paths for spin-flip inelastic tunneling in the antiparallel configuration are from the majority-spin band of the emitter to the majority-spin band of the collector and from the minority-spin band of the emitter to the minority-spin band of the collector. Schematics of the tunneling processes for the antiparallel alignment in the Zhang model are shown in Fig. 1.8.

Note that the T-dependent terms in both G_P and G_{AP} are positive and increasing with increasing T due to the T dependence of $T\cdot f(T)$. This behavior is due to the increase in the number and energy of thermally excited magnons involved in spin-flip tunneling.

Next, let's normalize $G_P(T)$ and $G_{AP}(T)$ by the respective values at $T = 0$, i.e. $G_P(T = 0) = G_{P,el}$ and $G_{AP}(T = 0) = G_{AP,el}$. The thus normalized $G_P(T)$ is given as

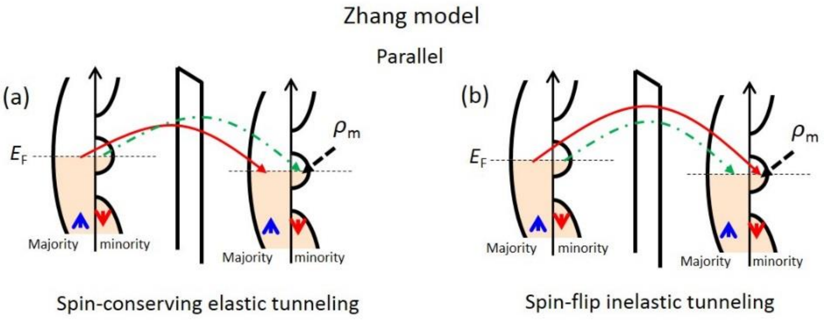

Fig. 1.7. Schematics of tunneling processes for the parallel alignment in the Zhang model [52]. (a) Spin-conserving elastic tunneling process, including tunneling from the majority-spin band (the minority-spin band) of the emitter electrode to the majority-spin band (the minority-spin band) of the collector. (b) Spin-flip inelastic tunneling process via a thermally excited magnon, including tunneling from the majority-spin band (the minority-spin band) of the emitter to the minority-spin band (the majority-spin band) of the collector via a thermally excited magnon.

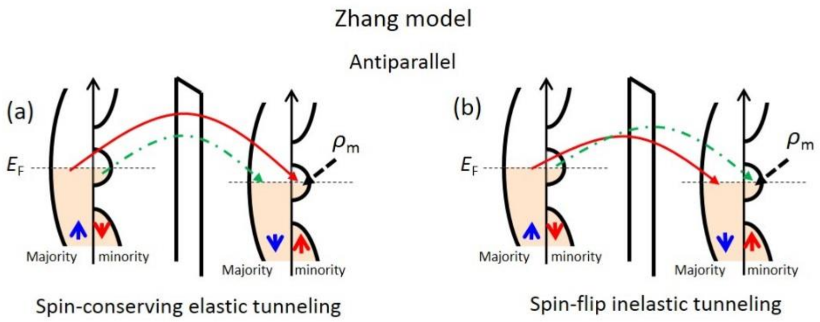

Fig. 1.8. Schematics of tunneling processes for the antiparallel alignment in the Zhang model [52]. (a) Spin-conserving elastic tunneling process, including tunneling from the majority-spin band (the minority-spin band) of the emitter electrode to the minority-spin band (the majority-spin band) of the collector. (b) Spin-flip inelastic tunneling process via a thermally excited magnon, i.e., tunneling from the majority-spin band (the minority-spin band) of the emitter to the majority-spin band (the minority-spin band) of the collector via a thermally excited magnon.

$$\frac{G_{\mathrm{P}}(T)}{G_{\mathrm{P}}(T=0)}=1+\frac{\frac{2S}{E_{\mathrm{m}}}k_{\mathrm{B}}T\cdot f(T)\cdot 2\rho_{\mathrm{M}}\rho_{\mathrm{m}}}{(\frac{|T^{d}|^{2}}{|T^{j}|^{2}}+2S^{2})(\rho_{\mathrm{M}}{}^{2}+\rho_{\mathrm{m}}{}^{2})}=1+a(\frac{1-P^{2}}{1+P^{2}})k_{\mathrm{B}}T\cdot f(T), \qquad (1.16)$$

$$a=Q\frac{2S}{E_{\mathrm{m}}}, \qquad (1.17)$$

$$Q=\frac{1}{\frac{|T^{d}|^{2}}{|T^{j}|^{2}}+2S^{2}}. \qquad (1.18)$$

Thus, according to the original Zhang model, the increase in the normalized $G_{\mathrm{P}}(T)$ is larger for a lower P and smaller for a higher P. While the normalized $G_{\mathrm{AP}}(T)$ given by the original Zhang model is

$$\frac{G_{\mathrm{AP}}(T)}{G_{\mathrm{AP}}(T=0)}=1+\frac{\frac{2S}{E_{\mathrm{m}}}(\rho_{\mathrm{M}}{}^{2}+\rho_{\mathrm{m}}{}^{2})k_{\mathrm{B}}T\cdot f(T)}{(\frac{|T^{d}|^{2}}{|T^{J}|^{2}}+2S^{2})\cdot 2\rho_{\mathrm{M}}\rho_{\mathrm{m}}}=1+a(\frac{1+P^{2}}{1-P^{2}})k_{\mathrm{B}}T\cdot f(T). \qquad (1.19)$$

Thus, the increase in the normalized $G_{\mathrm{AP}}(T)$ is smaller for a lower P and larger for a higher P.

On the other hand, Shang *et al.* took into consideration only spin-conserving elastic tunneling with a decaying P with increasing T. The decay in P with increasing T inevitably occurs due to spin fluctuations at finite temperatures. By assuming the Julliere model, G_{P} and G_{AP} are expressed using P as

$$G_{\mathrm{P}}=A(\rho_{\mathrm{M}}{}^{2}+\rho_{\mathrm{m}}{}^{2})=\frac{1}{2}A(\rho_{\mathrm{M}}+\rho_{\mathrm{m}})^{2}(1+P^{2}), \qquad (1.20)$$

$$G_{\mathrm{AP}}=A(2\rho_{\mathrm{M}}\rho_{\mathrm{m}})=\frac{1}{2}A(\rho_{\mathrm{M}}+\rho_{\mathrm{m}})^{2}(1-P^{2}), \qquad (1.21)$$

where A is a constant. Let's introduce the T dependence of P, i.e., P decreases with increasing T, to Eq. (1.20) and Eq. (1.21) (the Shang model). The T dependence of P is due to spin fluctuations at finite T. This leads to a decrease in P, in which the main factor is the decrease in ($\rho_{\mathrm{M}} - \rho_{\mathrm{m}}$) along with ($\rho_{\mathrm{M}} + \rho_{\mathrm{m}}$) being almost constant with respect to T. Thus, it is reasonable to assume ($\rho_{\mathrm{M}} + \rho_{\mathrm{m}}$) being independent of T. Then, it is predicted from Eq. (1.20) and Eq. (1.21) with a decaying P with increasing T (the Shang model) that G_{P} decreases and G_{AP} increases with increasing T. A schematic of the Shang model is shown in Fig. 1.9. In comparison, the latter prediction for G_{AP} is apparently in agreement with that of the Zhang model, while the former prediction for G_{P} is in contrast with that of the Zhang model.

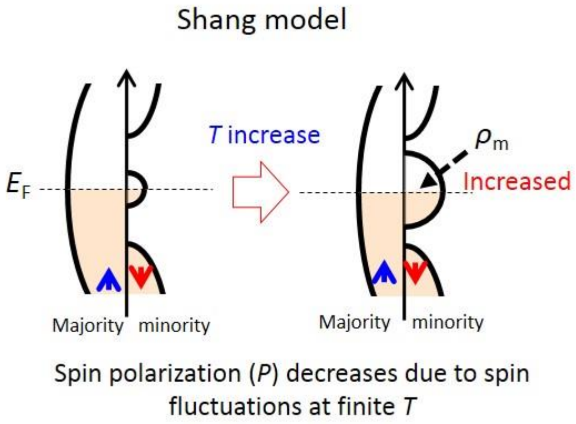

Fig. 1.9. Schematics of the T dependence of the spin-dependent density of states around E_F in the Shang model [53]. In this model, the spin polarization (P) at E_F decays with T due to spin fluctuation at finite T.

Indeed, the experimental $G_{AP}(T)$ had been explained and fitted by the original Zhang model in [54,55] or by the Shang model in [56]. However, note that the tunneling mechanisms that determine the T dependence are intrinsically different between these two models. On the other hand, the predictions for $G_P(T)$ by the Zhang model and the Shang model are opposed to each other as described above, i.e., the former predicts an increase in G_P(T) with T while the latter predicts a decrease. Previous studies on MTJs with an amorphous AlO_x tunnel barrier reported an increase in G_P with increasing T up to room temperature [53,54]. Most of the epitaxial MTJs with an MgO or $MgAl_2O_4$ tunnel barrier that have been reported so far have also shown an increase in G_P [8,55-60], while some epitaxial MTJs showed a decrease [61-63]. The increase in G_P with T for MTJs, including epitaxial MTJs, has been mostly explained by spin-flip inelastic tunneling via a thermally excited magnon, i.e., the Zhang model with an evidence of the role played by magnons indicated by tunneling spectroscopy [54,55,59]. Alternatively, the increase in G_P with T for an epitaxial MTJ has been explained within the framework of the Shang model by taking into account the smearing effect of the Fermi distribution function at finite temperatures [56], which increases G as T increases [64]. Note, however, that the influence of spin-flip inelastic tunneling was ignored in the Shang-model-based analysis. On the other hand, the origin of the decrease in G_P with increasing T observed for some epitaxial MTJs [61-63] is not yet fully understood. Thus, a more systematic experimental study is essential to get a deeper understanding of the origin of the T dependence of spin-dependent G_P and G_{AP}.

A promising approach would be to investigate half-metal-based MTJs with systematically varied P values at 0 K, as MTJs with highly spin-polarized electrodes arising from half-metallicity would show most typical T dependence of G_P and G_{AP}. In addition, it is a particularly desirable approach to extract how the T dependence of G_P and G_{AP} changes with P at 0 K by investigating a series of high-quality MTJs with systematically varied P at 0 K. Furthermore, development of a more comprehensive model for the T dependence of G_P and G_{AP} is requisite as the predictions of the Zhang and Shang models for $G_P(T)$ are opposite. This difference in the predictions for $G_P(T)$ also suggests that an analysis of the experimental $G_P(T)$ would be critical to revealing the origin of the T dependence of spin-dependent G.

1.2. Purpose

The purpose of the present study is to elucidate the origin of the T dependence of G_P and G_{AP} of MTJs through analyzing the experimental $G_P(T)$ and $G_{AP}(T)$ of high-quality MTJs showing giant TMRs and to provide a unified picture of how the T dependence of G_P and G_{AP} changes with P.

1.3. Approach

We experimentally investigated the T dependences of G_P and G_{AP} of CMS MTJs having systematically varied spin polarizations at 4.2 K by varying the Mn composition α in $Co_2Mn_\alpha Si$ electrodes that exhibited a giant TMR ratio of up to 2110% at 4.2 K (up to 366% at 290 K) [11,16]. Notable features in $G_P(T)$ were found; i.e., it decreased with increasing T from T_1 of about 30 K to T_2 ranging from about 162 K to 237 K depending on α; then it increased for $T > T_2$. Furthermore, as P at 4.2 K increased, T_2 increased and the maximum decrease in the normalized G_P [= $G_P(T)/G_P(4.2\text{ K})$] at T_2 increased. To clarify the origin of the characteristic T dependence of G_P, we developed a model that took into account both spin-conserving elastic tunneling in which P decays with increasing T and spin-flip inelastic tunneling via a magnon by extending the original Zhang model [52]. The extension of the

Zhang model was possible because of its generality in the sense that its expressions of $G_P(T)$ and $G_{AP}(T)$ include both elastic and inelastic tunneling terms, although P is assumed to be independent of T. Accordingly, we showed that the proposed model could reproduce the nonmonotonic behavior of the experimental $G_P(T)$. Furthermore, the dependence of the experimental $G_P(T)$ on P at 4.2 K was well explained by the proposed model. The model also consistently explained the experimental $G_{AP}(T)$, including a stronger T dependence for higher P at 4.2 K. Thus, it was found that elastic tunneling with decaying P with increasing T and inelastic tunneling via a magnon are two key factors that determine the T dependence of spin-dependent tunneling conductance of MTJs. This finding is generally applicable to MTJs with a wide range of P. It was also indicated that an analysis of the experimental $G_P(T)$ is critical to revealing the origin of the T dependence of G_P and G_{AP}.

Chapter 2

Experimental Methods

2.1. Preparation of the magnetic tunnel junctions

2.1.1. Layer structure

The $G_P(T)$ and $G_{AP}(T)$ mainly of two series of $Co_{50}Fe_{50}$ (CoFe)-buffered CMS MTJs having $Co_2Mn_\alpha Si_{0.84}$ electrodes of $Co_2Mn_\alpha Si_{0.96}$ electrodes were measured and analyzed in this study. The series had various α values ranging from a Mn-deficient composition of $\alpha < 2 - \beta$, where β is the Si composition expression of $Co_2Mn_\alpha Si_\beta$, to a Mn-rich one of $\alpha > 2 - \beta$. The MTJ layer structure was as follows: (from the substrate side) MgO buffer (10 nm)/CoFe buffer (30 nm)/CMS lower electrode (3 nm)/MgO barrier (1.4−3.2 nm)/CMS upper electrode (3 nm)/CoFe (1.1 nm)/$Ir_{22}Mn_{78}$ (10 nm)/Ru cap (5 nm), grown on a MgO(001) substrate, as shown in Fig. 2.1(a). The fabrication procedure of the CoFe-buffered CMS MTJs has been reported elsewhere [11]. Briefly, each layer was successively deposited in an ultrahigh-vacuum chamber equipped with magnetron cathodes and an electron beam evaporator. The CMS upper and lower electrodes were prepared by magnetron cosputtering from a nearly stoichiometric CMS target and Mn target (with a base pressure of about 6×10^{-8} Pa). The composition of the CMS film was determined by inductively coupled plasma analysis with an accuracy of 2−3% for Co and Mn, and 5% for Si. The film composition was systematically varied by adjusting the relative amounts of sputtered Mn.

The MgO tunnel barrier in the MTJ layer structure had a wedge shape, and its nominal thickness was varied from 1.4 to 3.2 nm on each 20 × 20 mm^2 MgO(001) substrate by linearly moving the shutter during the deposition by electron beam evaporation. The CoFe buffer, CMS lower electrode, MgO barrier, CMS upper electrode, and IrMn layer were all deposited at room temperature. The MTJ layer structure was annealed *in situ* at 400 ˚C for $Co_2Mn_\alpha Si_{0.84}$ MTJ series [16] or 500 ˚C for $Co_2Mn_\alpha Si_{0.96}$ MTJ series [11] just after deposition of the CoFe buffer and at 600 ˚C for $Co_2Mn_\alpha Si_{0.84}$ MTJ series [16] or 550 ˚C for $Co_2Mn_\alpha Si_{0.96}$ MTJ series [11] immediately after the deposition of the CMS lower electrode and fairly soon after the deposition of the CMS upper electrode for 15 minutes. The 30-nm-thick CoFe buffer was used to improve the interfacial structural properties [11]. This is because that the lattice mismatch between CoFe and MgO with a 45˚ in-plane rotation is −4.3% which is smaller than that of −5.1% between the fully relaxed CMS lower electrode and MgO. Furthermore, the lattice mismatch between CMS and CoFe is as small as −0.8%. Thus the ultrathin CMS lower electrode (3 nm) grown on the CoFe buffer was lattice matched with the CoFe buffer, leading to a small lattice mismatch in the MTJ trilayer. This resulted in a larger misfit dislocation spacing at the interfaces between CMS electrodes and the MgO barrier in the CoFe-buffered CMS/MgO/CMS MTJs (CMS MTJs) than that in the MgO-buffered CMS MTJs [11]. The smaller misfit dislocation densities at the interfaces between the CMS electrodes and the MgO barrier in the CoFe-buffered CMS MTJs significantly enhanced the TMR ratios compared with those of the MgO-buffered CMS MTJs [11]. The CoFe (1.1 nm)/IrMn (10 nm) bilayer was prepared for exchange biasing. Thus, the upper CMS electrode worked as the magnetically pinned layer while the lower CMS electrode as the free layer.

Figure 2.1(b) shows a cross-sectional high-resolution transmission electron microscopy (HRTEM) image of a CoFe-buffered CMS MTJ. It was shown that all layers were grown epitaxially and were single crystalline. It was also confirmed that atomically flat and abrupt interfaces were formed. Importantly, there were no clear lattice misfit dislocations between CoFe buffer and the lower CMS electrode. All these results indicated that the T dependence of G was investigated for CMS MTJs with high-quality layer structures.

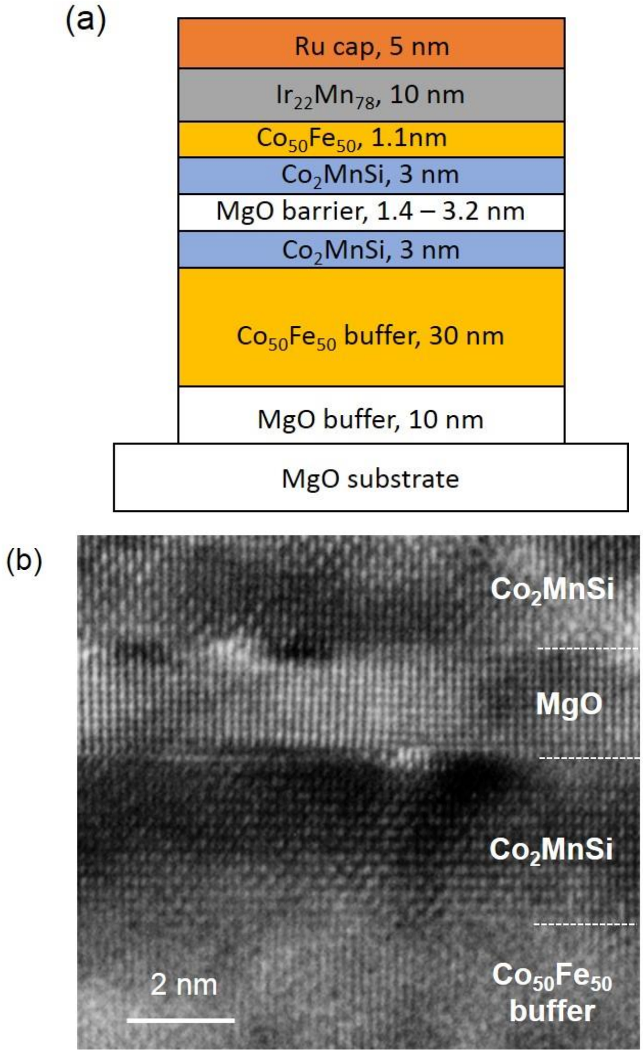

Fig. 2.1. (a) Schematic diagram of the layer structure of $Co_{50}Fe_{50}$ (CoFe)-buffered $Co_2Mn_{\alpha}Si$ (CMS)/MgO/CMS MTJ (CMS MTJ) consisting of (from the substrate side) MgO buffer (10 nm)/CoFe buffer (30 nm)/CMS lower electrode (3 nm)/MgO barrier (1.4−3.2 nm)/CMS upper electrode (3 nm)/CoFe (1.1 nm)/$Ir_{22}Mn_{78}$ (10 nm)/Ru cap (5 nm), grown on a MgO(001) single-crystal substrate. (b) Cross-sectional HRTEM lattice image of a CoFe-buffered Co_2MnSi MTJ layer structure consisting of (from the lower side) $Co_{50}Fe_{50}$ (CoFe) buffer/lower Co_2MnSi (3 nm)/MgO barrier (~2.5 nm)/upper Co_2MnSi (3 nm)/Ru (0.8 nm)/ $Co_{90}Fe_{10}$ (2 nm)/$Ir_{22}Mn_{78}$ (10 nm)/Ru cap (5 nm) with Mn-rich $Co_2Mn_{1.29}Si_{1.0}$ electrodes; it was taken along the [1-10] direction of the Co_2MnSi [11].

2.1.2. Device fabrication process

MTJs with the fully epitaxial layer structures described above were fabricated using photolithography and Ar ion milling. A schematic view of the MTJ process was shown in Fig. 2.2. To be brief, there are generally three steps in fabricating the MTJs. In the first process (M1), the layer structure was electrically isolated into systematically aligned M1 patterns on the wafer by argon ion milling using M1 photoresist pattern in which the layer structure was etched down to the MgO buffer layer (or to the MgO substrate). Then, in the second process (M2), the MTJs with a junction size of $10 \times 10\ \mu\mathrm{m}^2$ were patterned by argon ion milling with the resist patterns for a $10 \times 10\ \mu\mathrm{m}^2$ junction, in which the layer structure was etched down to the MgO barrier layer. Then, a SiO_2 layer was deposited and patterned by self-aligning lift-off technique using the resist pattern for the M2 ion milling process to obtain the planarization and the electrical isolation between the metallic layers. In the third process (M3), a 200-nm-thick gold layer was patterned for wiring by photolithography, electron beam evaporation of gold, and lift-off technique. After the microfabrication, the MTJs were annealed *ex-situ* at 350 ˚C in a vacuum of 5×10^{-2} Pa and magnetic field of 5 kOe to enable exchange biasing on the upper CMS electrode.

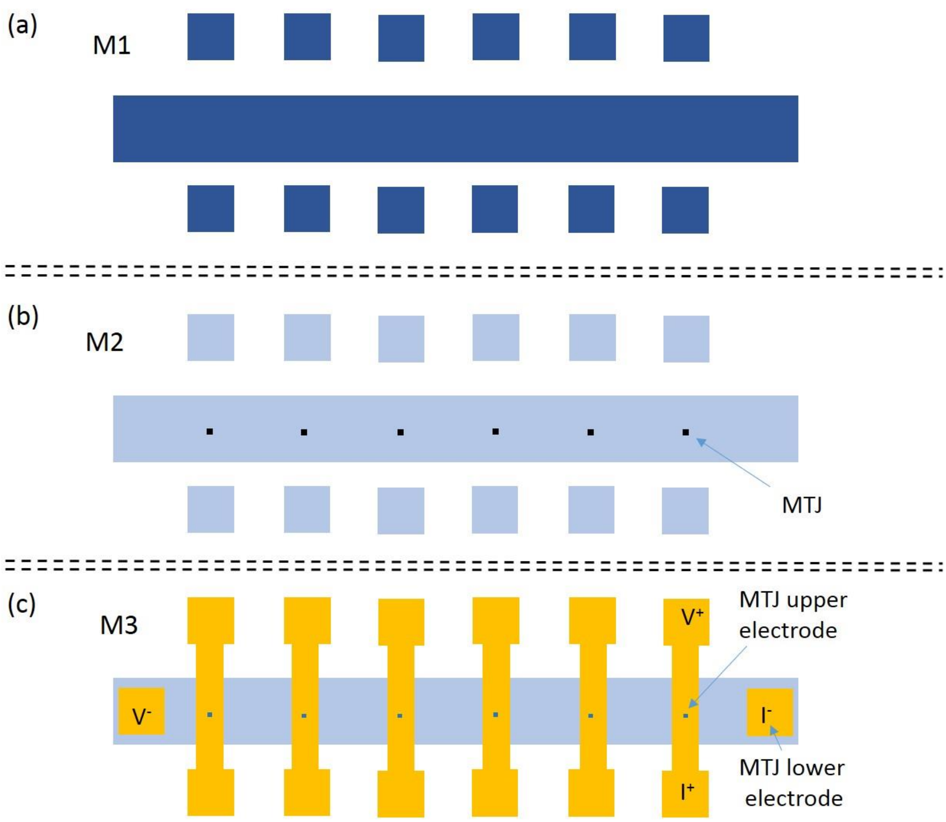

Fig. 2.2. A schematic view of the MTJ process. (a) In the first process (M1), the layer structure was electrically isolated into systematically aligned M1 patterns on the wafer by argon ion milling using the M1 photoresist patterns in which the layer structure was etched down to the MgO buffer layer (or to the MgO substrate). (b) In the second process (M2), the MTJs with a junction size of $10 \times 10\ \mu m^2$ were patterned by argon ion milling with the resist patterns for a $10 \times 10\ \mu m^2$ junction, in which the layer structure was etched down to the MgO barrier layer. Then, a SiO_2 layer was deposited and patterned by self-aligning lift-off technique using the resist pattern for the M2 ion milling process to obtain the planarization and electrical isolation between the metallic layers. There were six MTJs on each lower electrode. (c) In the third process (M3), a 200-nm-thick gold layer was patterned for wiring by photolithography, electron beam evaporation of gold, and lift-off technique.

2.2. Tunneling magnetoresistance characteristics

The TMR characteristics of MTJs were measured using a dc four-probe method with a bias voltage of 5 mV at 290 K and 1 mV at 4.2 K by swapping the external magnetic field. To measure the TMR characteristics at low temperature, the wafer with fabricated MTJs was diced into small chips and then a diced chip was attached to a dual in-line package (DIP). Then, wire bonding was done between the pads prepared on a chip and those on the DIP using gold wires. Typical major-loop TMR curves at 290 K for a CMS MTJ with Mn-rich $Co_2Mn_{1.30}Si_{0.84}$ electrodes are shown in Fig. 2.3. The MTJ exhibited clear exchange-biased TMR characteristics with a giant TMR ratio of 335% at 290 K. The magnetization configurations between the lower and upper electrodes at different magnetic fields were also shown in Fig. 2.3.

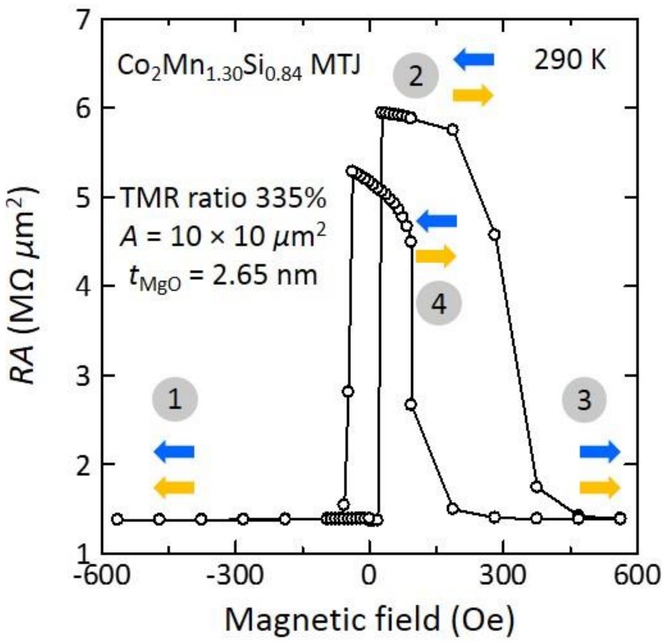

Fig. 2.3. Typical major-loop TMR curves of a CMS MTJ with Mn-rich $Co_2Mn_{1.30}Si_{0.84}$ electrodes and t_{MgO} = 2.65 nm showing a TMR ratio of 335% at 290 K. The magnetization configurations between the lower and upper electrodes at different magnetic fields were also shown.

The major-loop TMR characteristics shown in Fig. 2.3 are obtained by the following procedure. At first, the magnetization configuration was initialized at state 1 in which the magnetizations of the lower and upper electrodes were aligned parallel. When the magnetic field was increased to be larger than the coercive force of the free layer (the lower electrode), the configuration changed into state 2, i.e., antiparallel. With further increasing the magnetic field to be larger than the pinning force between the antiferromagnetic IrMn layer and the CoFe/CMS upper electrode, the direction of the magnetization of the CoFe/CMS upper electrode also switched, thus another parallel alignment, state 3, was obtained. Then, the magnetic field was decreased, resulting in the reversal of the magnetization of the pinned layer first and the associated antiparallel alignment (state 4). Further decreasing the magnetic field, the magnetization direction of the free layer switched to be parallel to the magnetic field, resulting in the parallel alignment between the lower and upper electrodes.

Figure 2.4 shows typical minor-loop TMR curves for a CMS MTJ at 4.2 K and 290 K. The MTJ is the same as that shown in Fig. 2.3. Giant TMR ratios of 2010% at 4.2 K and 335% at 290 K were obtained.

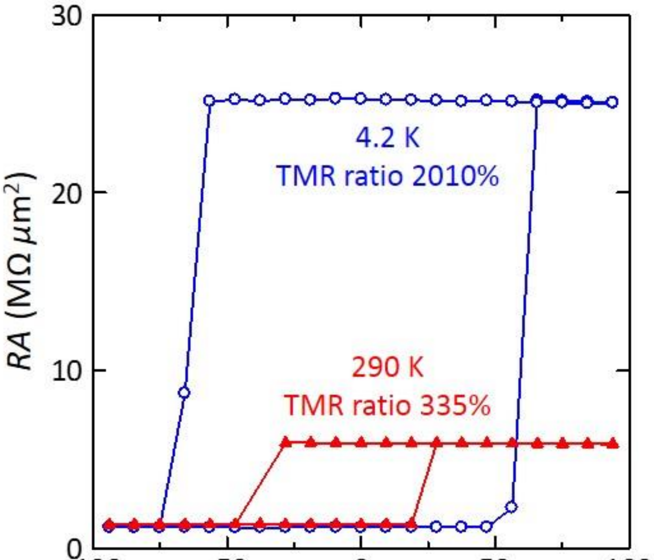

Fig. 2.4. Typical minor-loop TMR curves of a CMS MTJ with Mn-rich $Co_2Mn_{1.30}Si_{0.84}$ electrodes and t_{MgO} = 2.65 nm at 4.2 K and 290 K. The MTJ is the same as that shown in Fig. 2.3. Giant TMR ratios of 2010% at 4.2 K and 335% at 290 K were obtained.

2.3. Estimation of the MgO barrier height

Figure 2.5 plots typical dependence on t_{MgO} of R_PA, $R_{AP}A$, and the TMR ratio at 290 K for CMS MTJs with $Co_2Mn_{1.30}Si_{0.84}$ electrodes fabricated on a 20 × 20 mm^2 substrate over a t_{MgO} range from 2.2 to 3.1 nm, where A is the nominal junction area of 10 × 10 μm^2. We have reported TMR ratios of up to 2110% at 4.2 K and 366% at 290 K for these MTJs [16]. The dependences of R_PA and $R_{AP}A$ on t_{MgO} were exponential with almost identical slopes, resulting in nearly constant TMR ratios from 2.2 to 3.1 nm of t_{MgO}. Furthermore, TMR ratios over 350% were obtained for a wide t_{MgO} range from 2.3 to 3.0 nm, with the maximum TMR ratio being 366% at 290 K.

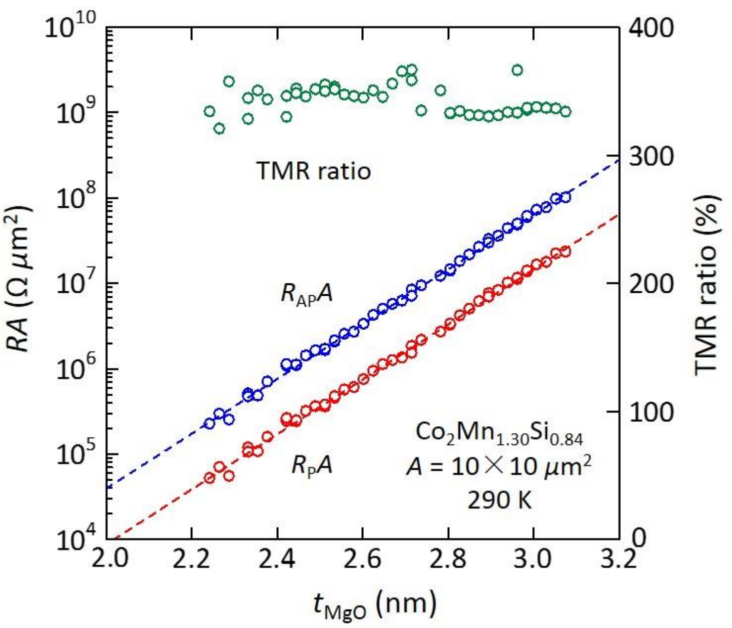

Fig. 2.5. A typical dependence of R_PA, $R_{AP}A$, and TMR ratio on MgO barrier thickness (t_{MgO}) at 290 K for CMS MTJs with $Co_2Mn_{1.30}Si_{0.84}$ electrodes fabricated on a 20 × 20 mm^2 substrate over a t_{MgO} range from 2.2 to 3.1 nm, where A is the nominal junction area of 10 × 10 μm^2. The MgO tunnel barrier had a wedge structure, and its nominal thickness was varied from 1.4 to 3.2 nm on each 20 × 20 mm^2 substrate by linearly moving the shutter during the deposition by electron beam evaporation.

According to quantum mechanics, the transmission coefficient D for a single tunnel barrier structure is approximately given as

$$D \propto \exp(-\frac{2\sqrt{2m\varphi_0}}{\hbar}t), \qquad (2.1)$$

where t is the tunnel barrier thickness, φ_0 is the effective tunnel barrier height, i.e., the energy difference between the E_F of the emitter electrode and the bottom of the conduction band in the tunnel barrier, and m is the effective mass of the conduction electron. The tunneling conductance G is proportional to D, and the tunneling resistance R is inversely proportional to D [65]. Then, G is given as

$$G \propto \exp(-\frac{2\sqrt{2m\varphi_0}}{\hbar}t), \qquad (2.2)$$

and R is given as

$$R \propto \exp(\frac{2\sqrt{2m\varphi_0}}{\hbar}t). \qquad (2.3)$$

Thus, the experimentally obtained linear dependence of $\ln(R_PA)$ on t_{MgO} and that of $\ln(R_PA)$ on t_{MgO} are consistent with the prediction of quantum mechanics for tunneling, i.e., Eq. (2.2). The value of $m^*\varphi_0$ (0.51 eV) was determined from the slope of the $\ln(R_PA)$ versus t_{MgO}, where m^* is the effective mass normalized by the electron rest mass. This value was close to that of 0.32 eV for epitaxial $Co_2Cr_{0.6}Fe_{0.4}Al$/MgO/CoFe MTJs [66] and 0.39 eV for epitaxial Fe/MgO/Fe MTJs [67].

2.4. Measurement of temperature dependence of spin-dependent tunneling conductance

The tunneling conductances $G_P(T)$ and $G_{AP}(T)$ were measured using a dc four-probe method at temperatures from 4.2 to 290 K at both positive and negative bias voltages of ±2 mV. Both polarities for the bias voltage were used to cancel the small thermoelectric force, which is particularly important for accurately measuring G_P values. In the measurement of G, we supplied a constant voltage of ±2 mV from a voltage source of a source-measure unit, and measured both the voltage across the MTJ using a high-precision digital voltmeter and the current flowing through the MTJ using a high-precision current measurement function of the source-measure unit. The measured voltages V_+ and V_- across the MTJ for the positive and negative bias voltages, respectively, are expressed as

$$V_+ = I_+ R + V_0, \qquad (2.4)$$

$$V_- = I_- R + V_0, \qquad (2.5)$$

where I_+ and I_- are the measured currents for the positive and negative bias voltages, V_0 is the thermoelectric force generated in the closed loop circuit. Then, the junction resistance R is given as

$$R = \frac{1}{G} = \frac{V_+ - V_-}{I_+ - I_-}. \qquad (2.6)$$

Thus, the tunneling resistance and equivalently conductance were measured by suppressing the influence of the small thermoelectric force.

The T dependence of the TMR ratio, which is defined in Eq. (1.3), was obtained from the values of G_P and G_{AP} at T.

Chapter 3

Results and discussion on the temperature dependence of spin-dependent tunneling conductance of magnetic tunnel junctions with Co_2MnSi electrodes

3.1. Overall features of the temperature dependence of spin-dependent tunneling conductance

In this chapter, we will first describe the overall features of the experimental T dependences of G_P and G_{AP} of CoFe-buffered CMS MTJs with $Co_2Mn_\alpha Si_{0.84}$ electrodes with various α values ranging from a Mn-deficient α = 0.73 to Mn-rich α = 1.24 and 1.30. Then we will describe the features of the experimental $G_P(T)$ in detail. Given the experimental results, we devise an extension of the Zhang model by introducing a T-dependent spin polarization and use it to discuss the origin of the observed T dependence of G_P through analyzing the experimental $G_P(T)$. The $Co_2Mn_\alpha Si_{0.96}$ MTJs with various α showed almost identical T dependences for G_P and G_{AP}. The α dependence of the TMR ratio of the

$Co_2Mn_{\alpha}Si_{0.84}$ MTJ series has been reported, and a TMR ratio of up to 2110% at 4.2 K (366% at 290 K) has been demonstrated for this MTJ series [16]. Figure 3.1(a) shows typical T dependence of G_P and G_{AP} from 4.2 to 290 K of a CMS MTJ with α = 1.30 ($Co_2Mn_{1.30}Si_{0.84}$ electrodes) that showed TMR ratios of 2010% at 4.2 K and 335% at 290 K. Here, G_{AP} showed a strong T dependence (G_{AP} at 290 K was 4.6 times higher than that at 4.2 K), while G_P changed only about 3% and could be regarded as being almost independent of T compared with the strong variation in G_{AP}. Because of these characteristics, the T dependence of the TMR ratio was determined mostly by that of G_{AP}, resulting in a strong T dependence of the TMR ratio [Fig. 3.1(b)].

Figure 3.2(a) plots the experimental $G_P(T)$ normalized by the respective values at 4.2 K, $G_{P,N}(T) = G_P(T)/G_P(4.2\ \mathrm{K})$, of the CMS MTJs with various α values. Furthermore, Fig. 3.2(b) plots the experimental $G_{AP}(T)$ normalized by the respective values at 4.2 K, $G_{AP,N}(T) = G_{AP}(T)/G_{AP}(4.2\ \mathrm{K})$. The TMR ratio at 4.2 K of these CMS MTJs increased with increasing α from 0.73 to 1.30 (Table I). The increase in the TMR ratio has been explained by the enhancement of half-metallicity due to the suppression of Co_{Mn} antisites for a Mn-rich composition [10,12]. As a basis for the characterization and analysis of the experimental $G_P(T)$ and $G_{AP}(T)$, we deduced the spin polarization at 4.2 K, P(4.2 K), for these MTJs from the TMR ratios at 4.2 K by assuming the Julliere model [33], i.e.,

$$\mathrm{TMR\ \ ratio} = \frac{2P^2}{1-P^2}, \qquad (3.1)$$

where P is defined using the majority-spin and minority-spin density of states (DOS) at E_F, ρ_M and ρ_m as $P = (\rho_M - \rho_m)/(\rho_M + \rho_m)$. We also assumed that the lower and upper electrodes had an identical P. Table I summarizes the deduced P(4.2 K) for the CMS MTJs. As demonstrated by their high TMR ratios at 4.2 K, the CMS MTJs exhibited significantly high P values of up to 0.954 at 4.2 K corresponding to the experimentally obtained TMR ratio of 2010% at 4.2 K. We approximated P at 0 K, P_0, by P(4.2 K) in the following analysis. The crucial role of coherent tunneling [34,68] has been experimentally [11] and theoretically [69] demonstrated in CMS MTJs. Thus, the P deduced from Eq. (3.1) is the value determined by ρ_M and ρ_m arising from the electronic states contributing to coherent tunneling [11,17]. In this sense, the deduced P should be called the tunneling spin polarization, although we will still refer to it as the tunneling spin polarization or spin polarization without distinguishing the meanings.

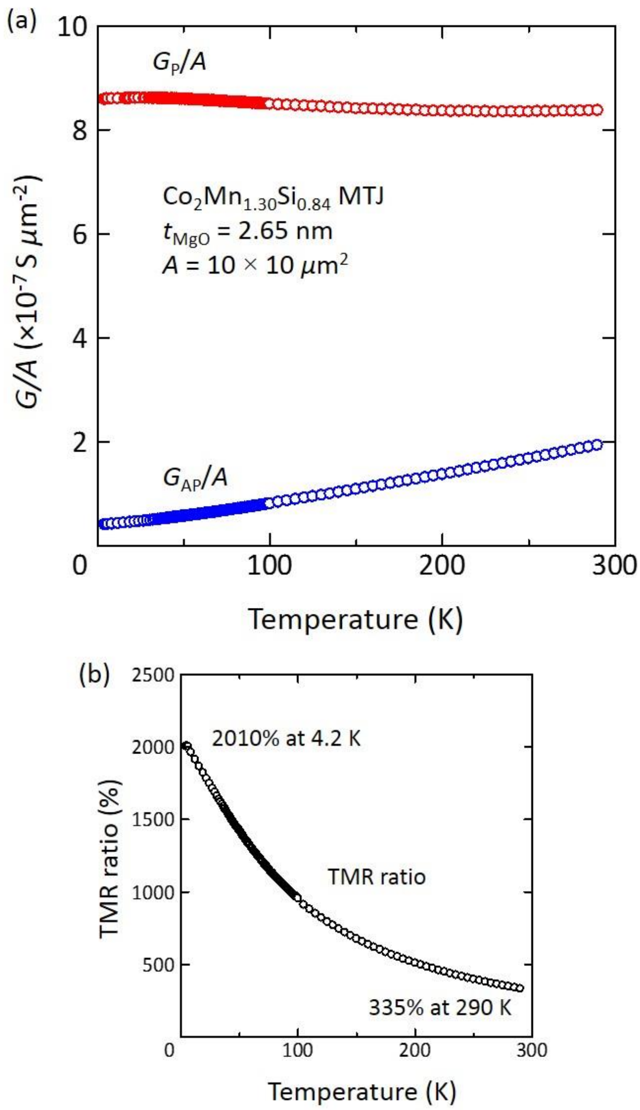

Fig. 3.1. (a) Typical temperature dependence of G_P/A and G_{AP}/A of a CMS MTJ with Mn-rich $Co_2Mn_{1.30}Si_{0.84}$ electrodes and t_{MgO} = 2.65 nm from 4.2 to 290 K showing TMR ratios of 2010% at 4.2 K and 335% at 290 K, where G_P and G_{AP} are the tunneling conductances for the parallel and antiparallel magnetization alignments between the lower and upper electrodes, and A is the nominal junction area of $10 \times 10\ \mu m^2$. The bias voltage was 2 mV. (b) Resulting T dependence of the TMR ratio.

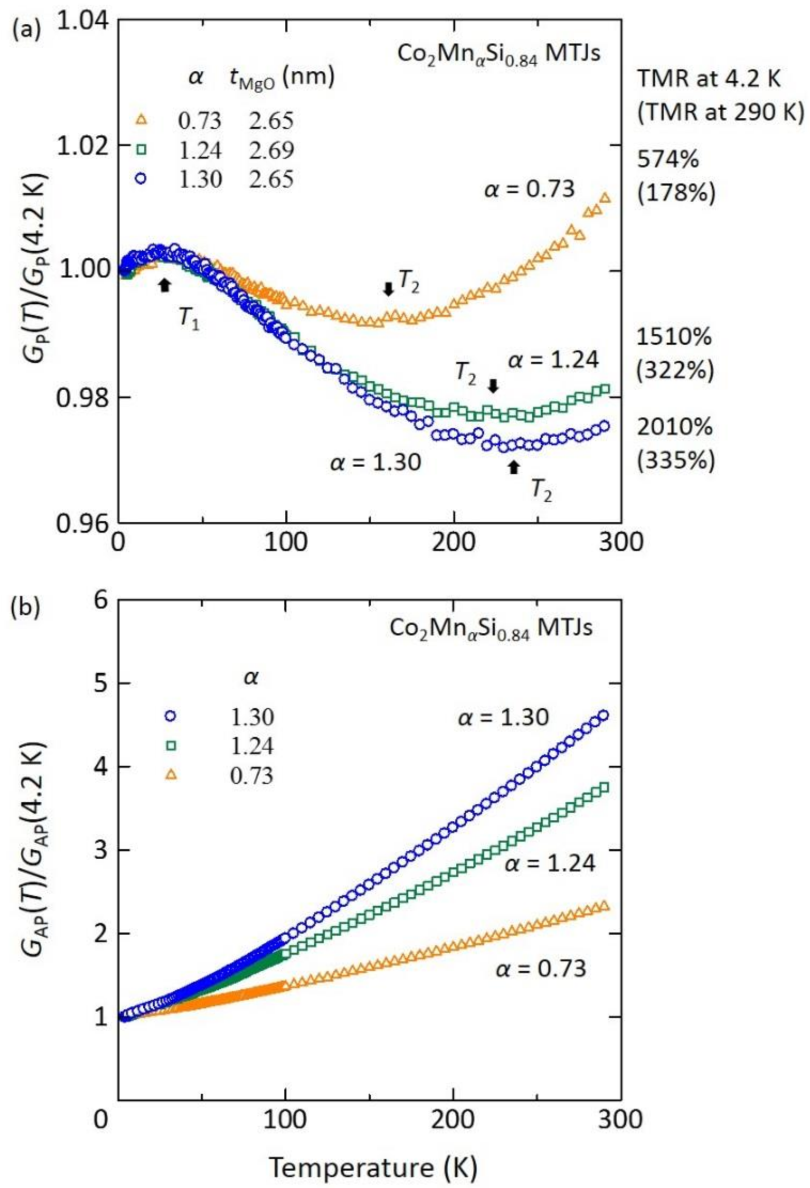

Fig. 3.2. (a) Normalized G_P and (b) G_{AP} as a function of T from 4.2 to 290 K for CMS MTJs with various α ranging from Mn-deficient α = 0.73 to Mn-rich α = 1.30 in $Co_2Mn_\alpha Si_{0.84}$ electrodes, where G_P and G_{AP} are normalized by the respective values at 4.2 K. The data of α = 1.30 MTJ are the same as those shown in Fig. 3.1.

TABLE I. TMR ratios at 4.2 and 290 K of CMS MTJs with various α in $Co_2Mn_\alpha Si_{0.84}$ electrodes of which $G_{P,N}(T)$ and $G_{AP,N}(T)$ are shown in Fig. 3.2 along with the respective nominal MgO barrier thicknesses (t_{MgO}). The tunneling spin polarizations at 4.2 K, P(4.2 K), deduced from the Julliere model [Eq. (3.1)] with the respective TMR ratios at 4.2 K, are also shown. The tunneling spin polarizations at 0 K, P_0, could be approximated by the respective P(4.2 K) and could be used in the analysis.

α in $Co_2Mn_\alpha Si_{0.84}$	t_{MgO} (nm)	TMR ratio at 4.2 K	TMR ratio at 290 K	P(4.2 K)
0.73	2.65	574%	178%	0.861
1.24	2.69	1510%	322%	0.940
1.30	2.65	2010%	335%	0.954

Note that the normalized $G_P(T)$ and $G_{AP}(T)$ data plotted in Fig. 3.2 are for MTJs having almost identical nominal t_{MgO} values of 2.66 nm ± 1% (Table I). Thus, the smearing effect of the Fermi distribution function at finite temperatures to the tunneling conductance [53,55,64] can be regarded as almost identical for these MTJs.

As shown in Fig. 3.2(a), the $G_{P,N}(T)$ of these MTJs exhibited distinct features, even though it can be regarded to be almost independent of T compared with the strong T dependence of $G_{AP,N}(T)$. The first feature is that the $G_{P,N}$ decreased with increasing T from $T = T_1$ of about 30 K to $T = T_2$ ranging from about 162 K for $\alpha = 0.73$ to 237 K for $\alpha = 1.30$. Then, it increased for $T > T_2$. The second feature is that T_2 increased as the TMR ratio at 4.2 K increased or equivalently P(4.2 K) increased, as shown in Fig. 3.3(a). The third feature is that the maximum decrease in the experimental $G_{P,N}$ at T_2, defined as $\Delta G_{P,N}(T_2) = G_{P,N}(T_2) - 1$ increased in magnitude as P(4.2 K) increased, as shown in Fig. 3.3(b).

On the other hand, the degree of the T dependence of $G_{AP,N}$ increased as P(4.2 K) increased. A previous paper discussed the T dependence of G_{AP} for CMS MTJs with various tunneling spin polarizations in terms of G_{AP}(290 K)/G_{AP}(4.2 K) according to the original Zhang model [12]. In this dissertation, we will discuss the key factors that determine the T dependences of G_P and G_{AP} from a wider point of view.

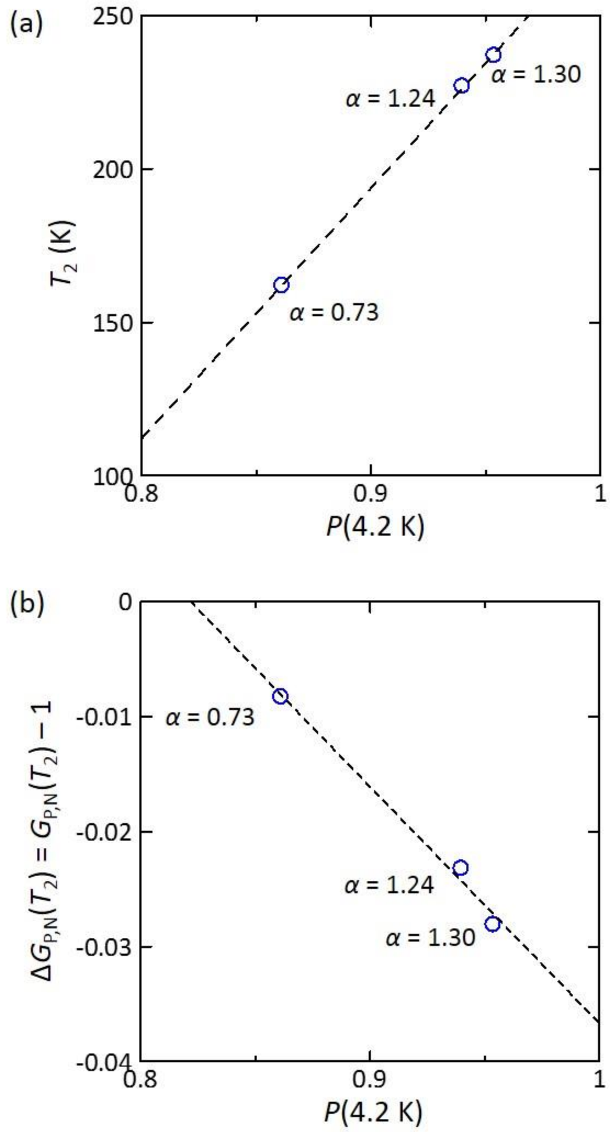

Fig. 3.3. Dependence of (a) the characteristic temperature T_2 and (b) the maximum decrease in the normalized G_P ($G_{P,N}$) at T_2, defined as $\Delta G_{P,N}(T_2) = G_{P,N}(T_2) - 1$, on the tunneling spin polarization at 4.2 K, P(4.2 K). The straight lines are guides for the eye.

3.2. Temperature dependence of spin-dependent tunneling conductance for parallel alignment

3.2.1. Theoretical model for analysis

Now let us discuss how these features of $G_{P,N}(T)$ and $G_{AP,N}(T)$ can be explained consistently. We will first analyze the experimental T dependence of $G_{P,N}$. The comparison of the experimental $G_{P,N}(T)$ with the predictions clearly indicates that neither the Shang model nor the Zhang model can explain the experimental $G_{P,N}(T)$. Thus, an analysis of $G_{P,N}(T)$ is crucial to clarifying the origin of the T dependence of spin-dependent tunneling conductance in MTJs with highly spin-polarized electrodes. We will focus on the decrease in $G_{P,N}$ as T increases from T_1 to T_2 and the increase in $G_{P,N}$ as T increases for $T > T_2$. Furthermore, taking into consideration that the variation in $G_{P,N}$ for $T < T_1$ was smaller than that for $T > T_1$ by one order of magnitude, we will ignore the small increase in G_P for 4.2 K $< T < T_1$. Regarding the experimental $G_{P,N}(T)$, the prediction of the Shang model for G_P, i.e., the negative dG_P/dT, is qualitatively in agreement with the experimental decrease in G_P for the T range from T_1 to T_2, whereas the prediction of the Zhang model, i.e., the positive dG_P/dT, is qualitatively in agreement with the experimental increase in G_P in the T range above T_2. Furthermore, the original Zhang model is more general than the Shang model in the sense that its expression for the tunneling conductance consists of both a spin-conserving elastic tunneling term and a spin-flip inelastic tunneling term, while the Shang expression consists only of a spin-conserving elastic tunneling term. Given its greater generality, we developed an extension of the original Zhang model by introducing a T dependence of P, i.e., a T dependence of ρ_M and ρ_m. This extension leads to a T dependence in the elastic tunneling term. We also took into consideration the effect of the broadening of the Fermi distribution, i.e., the smearing effect [53,55,64], on $G_P(T)$. In such a case, the elastic and inelastic tunneling conductance terms for the parallel alignment at a finite T are multiplied by a factor

$$S_e(T) = CT / \sin(CT), \qquad (3.2)$$

where $C = 1.387 \times 10^{-3} t/\varphi^{1/2}$, t is the thickness of the barrier (in nanometers), and φ is the barrier height (in electron volts) [64]. We assumed a φ of 3.5 eV, which corresponds to half the MgO band gap [55]. The validity of this value will be described later in this section. A typical value of $S_e(T)$ at 290 K is 1.056 for a t_{MgO} of 2.65 nm. The introduction of this small factor is required to fit the $G_P(T)$ of the CMS MTJs that had high spin polarization. This is because its variation as a function of T became small, i.e., being comparable to the variation in $S_e(T)$ as P_0 increases. Accordingly, $G_P(T)$ in the extended Zhang model for $k_BT > E_c$ is

$$G_{\mathrm{P}}(T) = G_{\mathrm{P,el}}(T) + G_{\mathrm{P,in}}(T), \qquad (3.3a)$$

$$G_{\mathrm{P,el}}(T) = S_{\mathrm{e}}(T) Q_1 \{[\rho_{\mathrm{M}}(T)]^2 + [\rho_{\mathrm{m}}(T)]^2\}, \qquad (3.3b)$$

$$G_{\mathrm{P,in}}(T) = S_{\mathrm{e}}(T) Q_2 k_{\mathrm{B}} T \cdot f(T) \cdot 2\rho_{\mathrm{M}}(T)\rho_{\mathrm{m}}(T), \qquad (3.3c)$$

where Q_1, Q_2, and $f(T)$ are

$$Q_1 = \frac{4\pi e^2}{\hbar}(|T^d|^2 + 2S^2 |T^J|^2), \qquad (3.3d)$$

$$Q_2 = \frac{4\pi e^2}{\hbar}\frac{2S}{E_{\mathrm{m}}}|T^J|^2, \qquad (3.3e)$$

$$f(T) = -\ln\left[1 - \exp\left(-\frac{E_{\mathrm{c}}}{k_{\mathrm{B}}T}\right)\right]. \qquad (3.3f)$$

The definitions of the parameters T^d, T^J, S, E_m, and E_c are given elsewhere[52]. Briefly, T^d and T^J are tunneling matrix elements for direct tunneling and for tunneling under the *s-d* exchange interaction between local and itinerant electrons at the interface, respectively, S is the spin parameter, $E_m = 3k_BT_C/(S + 1)$, E_c is the lower magnon cut-off energy, k_B is the Boltzmann constant, and T_C is the Curie temperature of the ferromagnetic electrode. The only difference between this and the original model is that ρ_M and ρ_m are dependent on T in the former and they are independent of T in the latter. The first term of Eq. (3.3a), $G_{P,el}(T)$, represents the spin-conserving elastic tunneling process, and the second term, $G_{P,in}(T)$, represents the spin-flip inelastic tunneling process via a thermally excited magnon. The first term is equivalent to the Shang model, and also to the Julliere model, although the latter does not consider the T dependence of P. Here, G_P at $T = 0$ consists of spin-conserving elastic tunneling, which from Eq. (3.3) can be expressed as

$$G_{\mathrm{P}}(T=0) = Q_1\{[\rho_{\mathrm{M}}(T=0)]^2 + [\rho_{\mathrm{m}}(T=0)]^2\}, \qquad (3.4)$$

[note $S_e(T = 0) = 1$]. Thus, $G_P(T)$ normalized by its value at $T = 0$, $G_{P,N}(T)$, is

$$G_{\mathrm{P,N}}(T) = \frac{G_{\mathrm{P}}(T)}{G_{\mathrm{P}}(T=0)} = S_{\mathrm{e}}(T)\left\{1 - \frac{{P_0}^2 - [P(T)]^2}{1+{P_0}^2}\right\}$$
$$+ S_{\mathrm{e}}(T) a \left\{\frac{1-[P(T)]^2}{1+{P_0}^2}\right\} k_{\mathrm{B}} T \cdot f(T), \qquad (3.5\mathrm{a})$$

where $P(T)$ is the spin polarization at T, defined as

$$P(T) = \frac{\rho_{\mathrm{M}}(T) - \rho_{\mathrm{m}}(T)}{\rho_{\mathrm{M}}(T) + \rho_{\mathrm{m}}(T)}, \qquad (3.5\mathrm{b})$$

$$a = Q\frac{2S}{E_{\mathrm{m}}}, \qquad (3.5\mathrm{c})$$

$$Q = \frac{1}{\dfrac{|T^d|^2}{|T^J|^2} + 2S^2}, \qquad (3.5\mathrm{d})$$

and the relations $(\rho_M)^2 + (\rho_m)^2 = (1/2)(\rho_M + \rho_m)^2(1 + P^2)$ and $2\rho_M\rho_m = (1/2)(\rho_M + \rho_m)^2(1 - P^2)$ are used along with an assumption of $(\rho_M + \rho_m)$ being independent of T. To fit the experimental $G_P(T)$, we introduced the following Bloch type $T^{3/2}$ dependence for P as in the Shang model [53]:

$$P(T) = P_0(1 - \eta T^{3/2}), \qquad (3.6)$$

where η is a material-dependent constant. Note that Eq. (3.5) does not include a T-dependent term to explain the small decrease in G_P as T decreases from T_1 of about 30 K to 4.2 K. Thus, the fitted curve for a T range below T_1 becomes extrapolated from a T range above T_1. Because of this disagreement between the experimental and calculated $G_{P,N}$ for 4.2 K < T < T_1, a small constant c_0 was added to Eq. (3.5) for fitting. The final form of the normalized $G_P(T)$ in the extended Zhang model is thus

$$G_{\mathrm{P,N,fitting}}(T) = G_{\mathrm{P,N,el}}(T) + G_{\mathrm{P,N,in}}(T) + c_0, \qquad (3.7\mathrm{a})$$

$$G_{\mathrm{P,N,el}}(T) = S_{\mathrm{e}}(T)\left\{1 - \frac{P_0^2[1-(1-\eta_{\mathrm{P}}T^{3/2})^2]}{1+P_0^2}\right\}, \qquad (3.7\mathrm{b})$$

$$G_{\mathrm{P,N,in}}(T) = S_{\mathrm{e}}(T) a \left[\frac{1-P_0^2(1-\eta_{\mathrm{P}}T^{3/2})^2}{1+P_0^2}\right] k_{\mathrm{B}} T \cdot f(T). \qquad (3.7\mathrm{c})$$

3.2.2. Analysis and discussion

Figure 3.4 plots the fitting curves of Eq. (3.7) for the $G_{P,N}(T)$ shown in Fig. 3.2(a). The extended Zhang model reproduced the apparently complicated $G_{P,N}(T)$ for a wide T range except for $T < T_1$. The parameters giving the best fit, including η_P, $a = Q \cdot 2S/E_m$, and E_c^P, where η_P and E_c^P are η and E_c for the parallel alignment, and the resulting f(290 K) and $a \cdot f$(290 K) are summarized in Table II. The η_P value deduced from fitting, for example, for α =1.30 MTJ was 3.29×10^{-5} $K^{-3/2}$ ±5%. This relatively narrow error range was needed to reproduce the decreasing experimental $G_{P,N}(T)$ with increasing T for $T_1 < T < T_2$. The values of a deduced for the CMS MTJs with various α values are almost equal. The value of a in Eq. (3.7c) [and which is defined by Eq. (3.5c)] as calculated using the T_C of 985 K for CMS [32], a spin parameter S from 1/2 to 5/2, and $|T^d|^2/|T^J|^2$ from 10 to 100 (according to Ref. [52]) ranged from 0.059 to 3.06 eV^{-1}. Thus, the deduced value of 3.01 eV^{-1} for these MTJs was in a reasonable range. Here, E_c^P slightly increased with α from E_c^P = 0.31 meV for Mn-deficient α = 0.73 to E_c^P = 0.42 meV for Mn-rich α = 1.30. Regarding η_P, although the values deduced for the CMS MTJs with various α were within ±5%, they decreased with increasing α from $\eta_P = 3.70 \times 10^{-5}$ $K^{-3/2}$ for α = 0.73 to $\eta_P = 3.29 \times 10^{-5}$ $K^{-3/2}$ for α = 1.30, suggesting an increase in spin wave stiffness [70], or equivalently an increase in the energy of a spin wave with increasing α.

We also checked the validity of the deduced η_P values. To do so, we estimated the P(290 K) values from the respective η_P values for various α by using Eq. (3.6). Here, we call the thus-estimated P(290 K) values P^{TD}(290 K) and compare them with the corresponding P(290 K) values estimated from the respective TMR ratios at 290 K using the Julliere model of Eq. (3.1) [P^{TMR}(290 K)]. The P^{TD}(290 K) values ranged from P^{TD}(290 K) = 0.704 for α = 0.73 to P^{TD}(290 K) = 0.799 for α = 1.30, which are comparable with the P^{TMR}(290 K) values ranging from P^{TMR}(290 K) = 0.686 for α = 0.73 to P^{TMR}(290 K) = 0.791 for α = 1.30. This comparison suggests the deduced η_P values are in a reasonable range even though the estimated P^{TD}(290 K) values should not be regarded as rigorous.

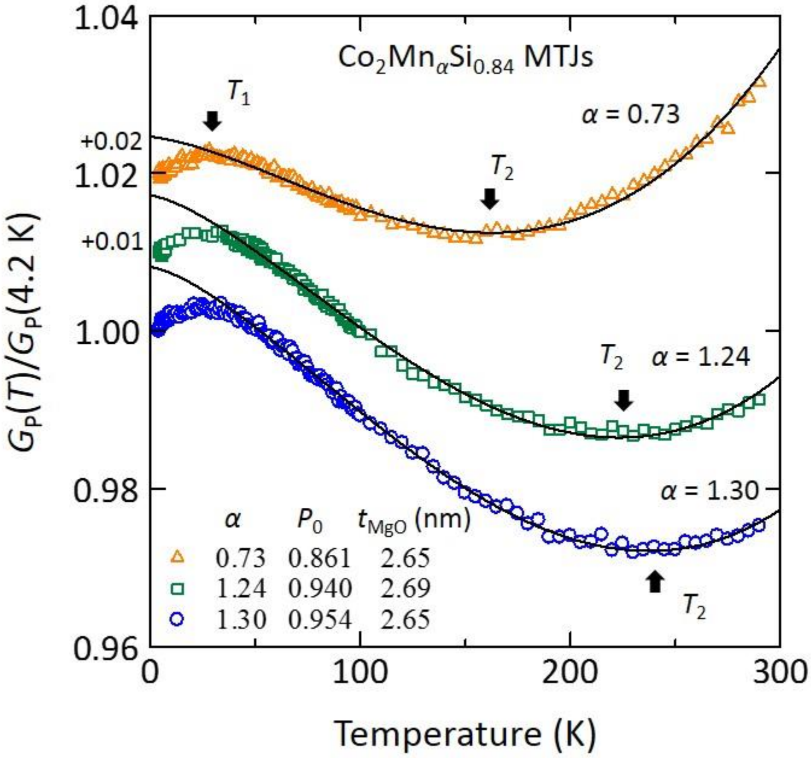

Fig. 3.4. Fitting curves of the extended Zhang model (solid lines) [Eq. (3.7)] for the experimental $G_P(T)$ normalized by the respective values at 4. 2 K of the CMS MTJs with α = 0.73 (open triangles), 1.24 (open squares), and 1.30 (open circles) in $Co_2Mn_\alpha Si_{0.84}$ electrodes. The experimental data of $G_P(T)$ are the same as shown in Fig. 3.2(a). The data of the normalized $G_P(T)$ for α = 0.73 and 1.24 have respective offsets of +0.02 and +0.01.

TABLE II. Parameters of η ($K^{-3/2}$), $a = Q\cdot 2S/E_m$ (eV^{-1}), E_c (meV), and c_0 for the CMS MTJs with various α shown in Table I deduced from fitting their respective normalized $G_P(T)$ [= $G_P(T)/G_P(4.2\ K)$] by the proposed extended Zhang model, and the resulting $f(290\ K)$ [Eq. (3.3f)] and $a\cdot f(290\ K)$. The thus-obtained parameters η and E_c for the parallel alignment are represented as η_P and E_c^P.

α in $Co_2Mn_\alpha Si_{0.84}$	Fitting model	η_P ($K^{-3/2}$)	$a = Q\cdot 2S/E_m$ (eV^{-1})	E_c^P (meV)	f(290 K)	$a\cdot f$(290 K)	c_0
0.73	Extended Zhang model	3.699×10^{-5}	3.004	0.311	4.392	13.2	0.005
1.24		3.319×10^{-5}	3.006	0.408	4.122	12.4	0.007
1.30		3.294×10^{-5}	3.008	0.415	4.105	12.3	0.008

Given the good agreement between the experimental and calculated $G_{P,N}(T)$ given by the extended Zhang model, we can now discuss the origin of the features in the experimental $G_P(T)$ for the CMS MTJs with various α based on this model. The calculated $G_{P,N}(T)$ consists of basically two terms; one is the elastic tunneling term, and the other is the inelastic tunneling term. The variation with T in the elastic tunneling term $\Delta G_{P,N,el}(T)$ which is defined as $G_{P,N,el}(T) - G_{P,N,el}(0)$ is given as

$$\Delta G_{\mathrm{P,N,el}}(T) = S_{\mathrm{e}}(T)\left\{1 - \frac{P_0^2[1-(1-\eta_{\mathrm{P}}T^{3/2})^2]}{1+P_0^2}\right\} - 1, \qquad (3.8)$$

and the variation with T in the inelastic tunneling term $\Delta G_{P,N,in}(T)$, which is identical to $G_{P,N,in}(T)$, is given by Eq. (3.7c).

Figure 3.5(a) plots the variations from the respective values at $T = 0$ K in these two terms. Here, $G_{P,N,el}(T)$ decreases ($\Delta G_{P,N,el}(T)$ is negative) and $G_{P,N,in}(T)$ increases ($\Delta G_{P,N,in}(T)$ is positive) as T increases. The latter feature is due to $f(T) > 0$. Note that the former and latter features are those predicted by the original Shang and Zhang models, respectively. In the extended Zhang model, there is a competition between these two terms, resulting in a complicated T dependence. Note that $\Delta G_{P,N,in}(T)$ is smaller for higher P_0, which arises from the P_0 dependence of the factor $[1 - P_0^2(1 - \eta_P T^{3/2})^2]/(1 + P_0^2) = C_P(T)$ in $\Delta G_{P,N,in}(T)$. The factor can be approximated as $C_P(T) \approx [1 - P_0^2(1 - 2\eta_P T^{3/2})]/(1 + P_0^2)$, and the term of $2\eta_P T^{3/2}$ can be neglected when discussing the α dependence of $\Delta G_{P,N,in}(T)$ because $2\eta_P T^{3/2}$ is much smaller than 1 even at 290 K. Accordingly, we can replace the factor $C_P(T)$ by a constant $(1 - P_0^2)/(1 + P_0^2) = \xi$, which decreases as P_0 increases and gets close to 0 as P_0 gets close to 1. Thus, the positive $\Delta G_{P,N,in}(T)$ is smaller for higher P_0 and gets close to 0 as P_0 gets close to 1. This dependence originates from that $G_{P,in}(T)$, which is due to spin-flip inelastic tunneling, is proportional to the product of $2\rho_M\rho_m$ (ρ_m gets close to 0 for P_0 being close to 1) while the G_P at $T = 0$ is proportional to the sum of $\rho_M^2 + \rho_m^2$ ($\approx \rho_M^2$ for highly spin-polarized electrodes). On the other hand, the dominant term of $\Delta G_{P,N,el}(T)$ [Eq. (3.8)] is approximated as $-2P_0^2\eta_P T^{3/2}/(1 + P_0^2)$ because $\eta_P T^{3/2} << 1$ and $S_e(T)$ can be replaced with 1 when discussing the α dependence of $\Delta G_{P,N,el}(T)$. Thus, the dependence of $\Delta G_{P,N,el}(T)$ on P_0 is determined by the coefficient, $-2P_0^2/(1 + P_0^2) = B_P$. Because B_P is negative, $G_{P,N,el}(T)$ decrease as T increases. Furthermore, B_P increases in magnitude as P_0 increases and gets close to -1 as P_0

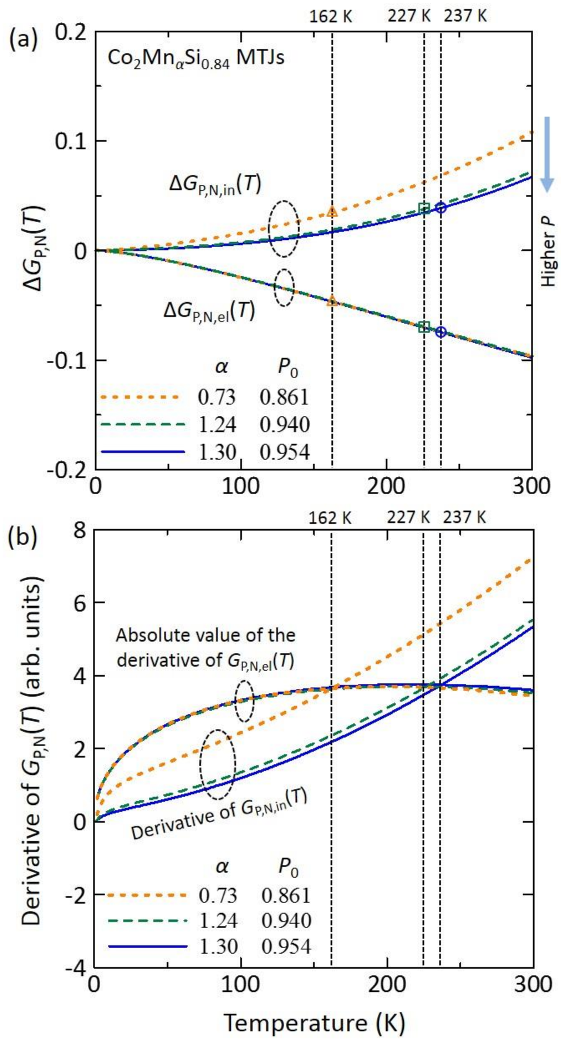

Fig. 3.5. (a) Variations with T from the values at T = 0 K of the elastic tunneling term $\Delta G_{P,N,el}(T)$ [Eq. (3.8)] and the inelastic tunneling term $\Delta G_{P,N,in}(T)$ [Eq. (3.7c)] obtained by fitting the experimental $G_{P,N}(T)$ by the extended Zhang model for CMS MTJs with α = 0.73 (dotted line), 1.24 (dashed line), and 1.30 (solid line). (b) Absolute values of the derivatives of $G_{P,N,el}(T)$ and derivatives of $G_{P,N,in}(T)$ for the CMS MTJs with α = 0.73 to 1.30. The intersection of the $-dG_{P,N,el}(T)/dT$ and $dG_{P,N,in}(T)/dT$ lines for each α in (b) determines T_2 to be 162 K for α = 0.73, 227 K for α = 1.24, and 237 K for α = 1.30. Then the $\Delta G_{P,N,in}(T_2)$ and $\Delta G_{P,N,el}(T_2)$ values for the α = 0.73, 1.24 and 1.30 MTJs were obtained in (a). These values for the α = 0.73, 1.24, and 1.30 MTJs are shown by triangles, squares, and circles, respectively.

gets close to 1. This behavior of B_P is in contrast to that of the coefficient ξ, which gets close to 0 as P_0 gets close to 1. Thus, the negative $\Delta G_{P,N,el}(T)$ increases in magnitude as P_0 increases and gets close to a finite value as P_0 gets close to 1. This P_0 dependence of $\Delta G_{P,N,el}(T)$ is in contrast to that of the positive $\Delta G_{P,N,in}(T)$ that gets close to 0 as P_0 gets close to 1. Note the values of $\Delta G_{P,N,el}(T)$ for P_0 ranging from 0.861 to 0.954 are almost equal. This is because (i) the magnitude in $dG_{P,N,el}(T)/dP_0$ is smaller than that in $dG_{P,N,in}(T)/dP_0$ (the former magnitude is half the latter), and (ii) although its magnitude is smaller, a further increase in the magnitude of $dG_{P,N,el}(T)/dP_0$ with increasing P_0 caused by the increase in α was mostly canceled by the smaller η_P for the larger α. In summary, the negative $\Delta G_{P,N,el}(T)$ becomes a more dominant factor in determining $G_P(T)$ because $\Delta G_{P,N,in}(T)$ becomes smaller at higher P_0.

Next, let us discuss the origin of the P_0 dependence of T_2 shown in Fig. 3.3(a). The characteristic temperature T_2 corresponds to $dG_P(T)/dT = 0$. Figure 3.5(b) plots the numerically obtained derivatives with respect to T of the elastic tunneling terms, $G_{P,N,el}(T)$ [Eq. (3.7b)], and the inelastic term, $G_{P,N,in}(T)$ [Eq. (3.7c)], for various α values, where $-dG_{P,N,el}(T)/dT$ is plotted instead of $\mathrm{d}G_{P,N,el}(T)/\mathrm{d}T$ because it is negative. The intersection of the $-dG_{P,N,el}(T)/dT$ and $dG_{P,N,in}(T)/dT$ lines for each α determines T_2 to be 162 K for P_0 = 0.861 (α = 0.73) to 237 K for P_0 = 0.954 (α = 1.30). The determined T_2 values agree with the corresponding experimental T_2 values because the experimental T_2 values were similarly determined from the $dG_P(T)/dT = 0$ point for the experimental G_P. Because the derivative of $G_{P,N,in}(T)$ decreased with increasing P_0, while $-dG_{P,N,el}(T)/dT$ remained almost constant for various P_0 values, the intersection point moved to a higher T as P_0 increased from 0.861 to 0.954. The decrease in the magnitude of $dG_{P,N,in}(T)/dT$ with increasing P_0 originated from the coefficient $C_P(T) = [1 - P_0^2(1 - \eta_P T^{3/2})^2]/(1 + P_0^2)$ in $G_{P,N,in}(T)$.

Now let us turn to the P_0 dependence of the maximum decrease in $G_{P,N}$ at T_2 [Fig. 3.3(b)]. Figure 3.5(a) plots straight lines corresponding to the respective T_2 values obtained from the intersection points in Fig. 3.5(b). The intersections of these straight lines with $\Delta G_{P,N,in}(T)$ and $\Delta G_{P,N,el}(T)$ for each α are their values at $T = T_2$. These plots show that $\Delta G_{P,N,el}(T_2)$ increases in magnitude as P_0 increases from P_0 = 0.861 (for Mn-deficient α = 0.73) to P_0 = 0.954 (for Mn-rich α = 1.30), while $\Delta G_{P,N,in}(T_2)$ is almost constant for various P_0. The larger increase in the magnitude of $\Delta G_{P,N}(T_2)$ for higher P_0 is explained as follows. Here, $\Delta G_{P,N,in}(T)$ decreased in the whole T range as P_0 increased. Thus, the contribution of $\Delta G_{P,N,in}(T)$ basically decreased as P_0 increased. However, because each $\Delta G_{P,N,in}(T)$ increased with increasing T and T_2 increased as P_0 increased, $\Delta G_{P,N,in}(T_2)$ was almost constant for various P_0. On the other hand, because (i) $\Delta G_{P,N,el}(T)$ was almost independent of P_0 in the whole T range, (ii) the magnitude of $\Delta G_{P,N,el}(T)$ increased with increasing T, and (iii) T_2 increased as P_0 increased, the magnitude of $\Delta G_{P,N,el}(T_2)$ increased with increasing P_0. Thus, the main factor that led to the P_0 dependence of the maximum decrease in $G_{P,N}$ at T_2 was $\Delta G_{P,N,in}(T)$ decreasing with increasing P_0.

3.2.3. Influence of smearing of the Fermi distribution function

We will now discuss the influence of the smearing effect on the T dependence of $G_{P,N}$ by analyzing two identical CMS MTJs with $Co_2Mn_{1.24}Si_{0.84}$ electrodes prepared in the same device fabrication process on the same MTJ epitaxial layer structure but having different nominal t_{MgO} values of 2.31 and 2.69 nm, where the t_{MgO} = 2.69 nm MTJ (α = 1.24) is the same as that analyzed above. Figure 3.6 compares the experimental $G_{P,N}(T)$ of the t_{MgO} = 2.31 nm MTJ (α = 1.24) with that of the t_{MgO} = 2.69 nm MTJ (α = 1.24) shown in Figs. 3.2(a) and 3.4. Here, the t_{MgO} = 2.31 nm MTJ (α = 1.24) showed a larger TMR ratio of 1690% at 4.2 K (328% at 290 K) compared with 1510% at 4.2 K (322% at 290 K) for the t_{MgO} = 2.69 nm MTJ (α = 1.24), resulting in a larger P(4.2 K) of 0.946 for the t_{MgO} = 2.31 nm MTJ (α = 1.24) compared with the P(4.2 K) of 0.940 for the t_{MgO} = 2.69 nm MTJ (α = 1.24). Moreover, the experimental $G_{P,N}(T)$ of the t_{MgO} = 2.31 nm MTJ (α = 1.24) had a larger T_2 and a larger decrease at T_2.

These features can be explained by the extended Zhang model, in particular by the two factors involved in the model: one is the larger P_0, leading to a further reduction in $G_{P,N,in}(T)$ compared with that for the t_{MgO} = 2.69 nm MTJ (α = 1.24); the other is a smaller $S_e(T)$ value arising from the smaller t_{MgO}, leading to a decrease in the unperturbed term with respect to the T-dependent P in the elastic tunneling term, i.e., the first term of $S_e(T)\cdot 1$ in Eq. (3.7b). Indeed, the extended Zhang model reproduced the experimental $G_{P,N}(T)$ of the t_{MgO} = 2.31 nm MTJ (α = 1.24; Fig. 3.6) as well as it did for the t_{MgO} = 2.69 nm MTJ (α = 1.24) [Fig. 3.4].

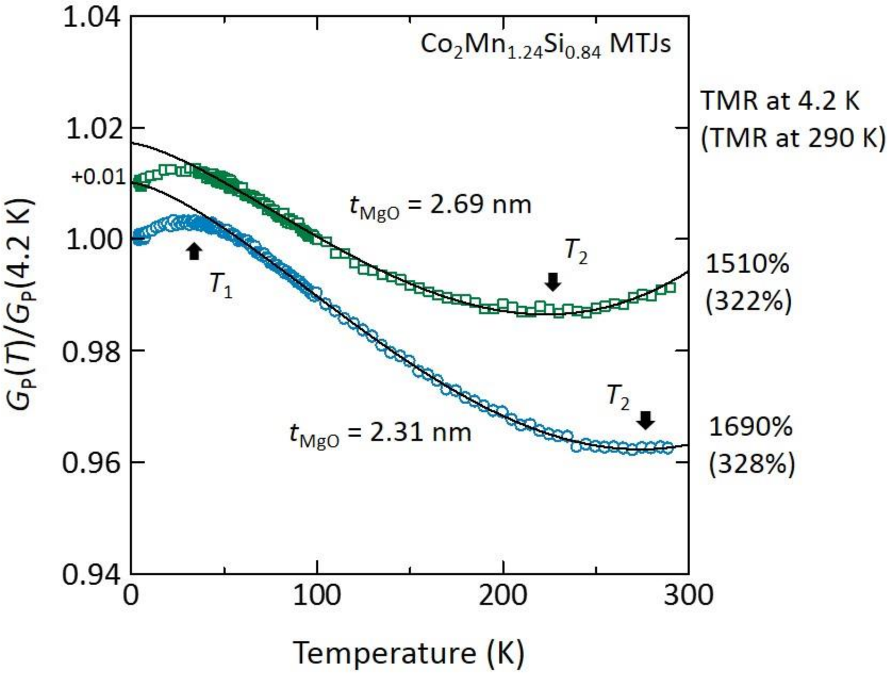

Fig. 3.6. Experimental $G_P(T)$ normalized by its value at 4.2 K, $G_P(T)/G_P(4.2\ \mathrm{K})$, of the t_{MgO} = 2.31 nm CMS MTJ with $Co_2Mn_{1.24}Si_{0.84}$ electrodes (α = 1.24; open circles) along with that of the t_{MgO} = 2.69 nm CMS MTJ (α = 1.24; open squares) for comparison. The fitting curve of the extended Zhang model for the t_{MgO} = 2.31 nm CMS MTJ is also shown along with that for the t_{MgO} = 2.69 nm CMS MTJ for comparison. The experimental $G_{P,N}(T)$ data and fitting curve of the extended Zhang model for the t_{MgO} = 2.69 nm MTJ (α = 1.24) are the same as those shown in Fig. 3.4. The data of the $G_{P,N}(T)$ for the t_{MgO} = 2.69 nm MTJ have an offset of +0.01.

TABLE III. Parameters of η_{P} ($\mathrm{K}^{-3/2}$), $a = Q\cdot 2S/E_{\mathrm{m}}$ (eV^{-1}), $E_{\mathrm{c}}^{\mathrm{P}}$ (meV), and c_0 deduced from fitting $G_{\mathrm{P,N}}(T)$ by the extended Zhang model, and the resulting f(290 K) and $a\cdot f$(290 K) for $\alpha = 1.24$ CMS MTJ ($Co_2Mn_{1.24}Si_{0.84}$) with t_{MgO} of 2.31 nm are shown along with those values for $\alpha = 1.24$ CMS MTJ with t_{MgO} of 2.69 nm (Table II) for comparison. The parameters of η_{P} ($\mathrm{K}^{-3/2}$), the barrier height φ, and the constant c_0 tentatively deduced from the fitting by the Shang model with the smearing factor for these two MTJs with t_{MgO} of 2.31 and 2.69 nm are also shown. The t_{MgO} = 2.31 nm CMS MTJ ($\alpha = 1.24$) had TMR ratios of 1690% at 4.2 K [corresponding to P(4.2 K) of 0.946] and 328% at 290 K.

t_{MgO} (nm)	Fitting model	η_{P} ($\mathrm{K}^{-3/2}$)	φ (eV)	S_{e}(290 K)	$a = Q\cdot 2S/E_{\mathrm{m}}$ (eV^{-1})	$E_{\mathrm{c}}^{\mathrm{AP}}$ (meV)	f(290 K)	$a\cdot f$(290 K)	c_0
2.31	Extended Zhang model	3.420×10^{-5}	3.5	1.042	3.009	0.486	3.951	11.9	0.010
	Shang model with smearing factor	4.087×10^{-5}	1.08	1.147	−	−	−	−	0.012
2.69	Extended Zhang model	3.319×10^{-5}	3.5	1.058	3.006	0.408	4.122	12.4	0.007
	Shang model with smearing factor	3.890×10^{-5}	1.34	1.162	−	−	−	−	0.009

As listed in Table III, the deduced-η_P, a, and E_c^P and resulting $a\cdot f(290\text{ K})$ for t_{MgO} = 2.31 nm MTJ (α = 1.24) are close to those deduced for the t_{MgO} = 2.69 nm MTJ (α = 1.24; Table II). This indicates that the different behaviors of these two MTJs can be reasonably explained by the P_0-dependent factor $\xi = (1 - P_0^2)/(1 + P_0^2)$ (ξ = 0.056 and 0.062 for the t_{MgO} = 2.31 and 2.69 nm MTJs, respectively) and t_{MgO}-dependent factor $S_e(T)$ in the extended Zhang model.

To reveal the problem associated with fitting $G_P(T)$ by the Shang model with the smearing effect, we tentatively fitted the experimental $G_{P,N}(T)$ of the two MTJs analyzed above. We then compared the fitting results of the Shang model, in particular the deduced parameters, with those of the extended Zhang model. In the analysis of $G_{P,N}(T)$ of the Shang model, we fitted the experimental $G_{P,N}(T)$ by using three free parameters, i.e., η, the barrier height φ in the smearing factor and the additional small constant c_0. The fitting function for the normalized experimental $G_{P,N}(T)$ is

$$G_{\mathrm{P,N,Shang}}(T) = S_e(T)\left\{1 - \frac{P_0^2[1-(1-\eta_P T^{3/2})^2]}{1+P_0^2}\right\} + c_0. \qquad (3.9)$$

The fitting curves for both MTJs (not shown, but they are similar to that shown in Fig. 3.6) apparently reproduced the experimental $G_{P,N}(T)$ with the fitting parameters shown in Table III. On the other hand, the deduced barrier heights φ in the factor $S_e(T)$ of the Shang model, φ_{Shang}, for these MTJs were quite small (Table III) compared with the φ = 3.5 eV assumed in the extended Zhang model. Furthermore, the φ_{Shang} value of 1.08 eV for the t_{MgO} = 2.31 nm MTJ was much smaller than the φ_{Shang} value of 1.34 eV of the t_{MgO} = 2.69 nm MTJ that was needed to reproduce the $G_{P,N}(T)$ of the former MTJ featuring the larger T_2 and the larger decrease at T_2 in the experimental $G_{P,N}(T)$ than that of the latter MTJ. Such a significant difference in the deduced φ values in the Shang model was caused because only the $S_e(T)$ term is responsible for the increased component with increasing T in the experimental $G_{P,N}(T)$ in the Shang model. However, such a significant difference is unreasonable because these MTJs were prepared from the same epitaxial layer structure. Furthermore, the linear relation in $\log R_PA$ versus t_{MgO} for the CMS MTJs prepared on the epitaxial MTJ layer structure indicated that these MTJs are characterized by an identical barrier height. Thus, it is difficult to validate the fitting of the experimental $G_{P,N}(T)$ by the Shang model with the smearing effect even though the fitting apparently reproduced the experimental result.

Finally, we should note that the barrier height φ was not definitely determined in this paper. However, its minimum value is estimated to be about 1.34 eV or larger. This value is the same as the value deduced from fitting the $G_{\mathrm{P,N}}(T)$ of the t_{MgO} = 2.69 nm MTJ (α = 1.24) by the Shang model with the smearing factor in which the contribution of inelastic tunneling is ignored, as described above. Even if we assume a wide φ range of 3.5 ± 1.5 eV, the factor S_{e}(290 K) for a typical t_{MgO} value of 2.65 nm is weakly dependent on φ in this range, and it only slightly changes from 1.10 for φ = 2.0 eV to 1.04 for φ = 5.0 eV. Furthermore, S_{e}(290 K) decreases with decreasing t_{MgO}. Thus, although the smearing factor calculated with φ = 3.5 eV corresponding to half the MgO energy gap has a certain margin of error, it would only slightly influence the results of the analysis in this paper, in particular by making a slight modification of the values of the deduced parameters.

3.2.4. Summary

In summary, our analysis of the experimental $G_{P,N}(T)$ of the CMS MTJs characterized by the systematically varied $P(4.2\ K)$ showed that the extended Zhang model could consistently explain the complicated behavior of $G_{P,N}(T)$. According to this model, the spin-flip inelastic tunneling conductance term in $G_P(T)$ is much larger than the T-dependent part of the spin-conserving elastic tunneling conductance term for MTJs characterized by a relatively low P_0. This results in an increase in $G_P(T)$ with increasing T from 4.2 K to room temperature. Thus, the analysis of the experimental $G_P(T)$ of MTJs with a relatively low P_0 by the original Zhang model that ignores the decaying P with T could be a good approximation [54,55]. On the other hand, the contribution of the inelastic tunneling conductance term decreases with increasing P_0 because of the decrease in the coefficient of $C_P(T)$ or the effectively equivalent parameter $\xi = (1 - P_0^2)/(1 + P_0^2)$, resulting in a relative increase in the T-dependent term of the elastic tunneling conductance term. This leads to competition between the elastic tunneling term $\Delta G_{P,N,el}(T)$ and the inelastic tunneling term $\Delta G_{P,N,el}(T)$. This competition caused the non-monotonic T dependence of $G_P(T)$. Thus, the proposed model provides a comprehensive understanding of the T dependence of G_P of MTJs ranging from those characterized by a relatively low P value to those characterized by a significantly high P arising from half-metallicity.

3.3. Temperature dependence of spin-dependent tunneling conductance for antiparallel alignment

3.3.1. Theoretical model for analysis

Now let us analyze the T dependence of G_{AP} of the CMS MTJs with various α values by using the extended Zhang model. For the antiparallel alignment, the smearing effect can be neglected for MTJs with high spin polarization. This is because the variation of $S_e(T)$ from 4.2 to 290 K is about several percents which is much smaller than the relative variation in G_{AP} as T increases from 4.2 to 290 K. For the CMS MTJs, the normalized variation in $S_e(T)$ at 290 K, i.e., $[S_e(290\text{ K}) - S_e(0\text{ K})]/S_e(0\text{ K})$, is 0.056 for a t_{MgO} value of 2.65 nm, as described above, while the normalized variation in $G_{AP}(T)$ at 290 K, i.e., $[G_{AP}(290\text{ K}) - G_{AP}(4.2\text{ K})]/G_{AP}(4.2\text{ K})$, ranged from 1.33 for $\alpha = 0.73$ to 3.60 for $\alpha = 1.30$, as shown in Fig. 3.2(b). Thus, the smearing factor was ignored in the analysis of $G_{AP}(T)$. Accordingly, the extended Zhang model for $G_{AP}(T)$ is

$$G_{\mathrm{AP}}(T) = G_{\mathrm{AP,el}}(T) + G_{\mathrm{AP,in}}(T), \qquad (3.10a)$$

$$G_{\mathrm{AP,el}}(T) = Q_1 \cdot 2\rho_{\mathrm{M}}(T)\rho_{\mathrm{m}}(T), \qquad (3.10b)$$

$$G_{\mathrm{AP,in}}(T) = Q_2 k_{\mathrm{B}} T \cdot f(T) \cdot \{[\rho_{\mathrm{M}}(T)]^2 + [\rho_{\mathrm{m}}(T)]^2\}, \qquad (3.10c)$$

where the coefficients Q_1 and Q_2 are given by Eqs. (3.3d) and (3.3e), respectively, the first term, $G_{AP,el}(T)$, of Eq. (3.10a) corresponds to spin-conserving elastic tunneling, and the second term, $G_{AP,in}(T)$, corresponds to spin-flip inelastic tunneling. Here, G_{AP} at $T = 0$ consists of spin-conserving elastic tunneling, which is expressed as

$$G_{\mathrm{AP}}(T=0) = Q_1 \cdot 2\rho_{\mathrm{M}}(T=0)\rho_{\mathrm{m}}(T=0). \qquad (3.11)$$

By assuming the T-dependent P expressed by Eq. (3.6) with $\eta = \eta_{AP}$ for the antiparallel alignment, $G_{AP}(T)$ normalized by its value at $T = 0$, $G_{AP,N}(T)$, is

$$G_{\mathrm{AP,N}}(T) = \frac{G_{\mathrm{AP}}(T)}{G_{\mathrm{AP}}(T=0)} = G_{\mathrm{AP,N,}el}(T) + G_{\mathrm{AP,N,in}}(T), \qquad (3.12a)$$

$$G_{\mathrm{AP,N,el}}(T) = 1 + \frac{P_0{}^2[1-(1-\eta_{\mathrm{AP}}T^{3/2})^2]}{1-P_0{}^2} = 1 + \Delta G_{\mathrm{AP,N,el}}(T), \qquad (3.12b)$$

$$G_{\mathrm{AP,N,in}}(T) = a\left[\frac{1+P_0{}^2(1-\eta_{\mathrm{AP}}T^{3/2})^2}{1-P_0{}^2}\right]k_{\mathrm{B}}T \cdot f(T) = \Delta G_{\mathrm{AP,N,in}}(T), \qquad (3.12c)$$

where the coefficient a is given by Eq. (3.5c). We also included variations with T in $G_{\mathrm{AP,N,el}}$ and $G_{\mathrm{AP,N,in}}$ from the values at $T = 0$, i.e., $\Delta G_{\mathrm{AP,N,el}}$ and $\Delta G_{\mathrm{AP,N,in}}$, in Eqs. (3.12b) and (3.12c). If we assume a T-independent spin polarization, corresponding to $\eta_{\mathrm{AP}} = 0$, Eq. (3.10) reduces to the original Zhang model, while if we ignore the second term of Eq. (3.10a), Eq. (3.10) reduces to the Shang model.

3.3.2. Analysis and discussion

Figure 3.7(a) plots the fitting curves of the extended Zhang model of Eq. (3.12) for the experimental $G_{\mathrm{AP,N}}(T)$ of the $\alpha = 1.30$ CMS MTJ that had a giant TMR ratio of 2010% at 4.2 K; the fitting curves of the original Zhang and Shang models are also plotted for comparison. The best fit parameters deduced from these fittings are listed in Table IV.

It was found that all these fittings could reproduce the $G_{\mathrm{AP,N}}(T)$. Among them, those of the original Zhang model and the extended Zhang model reproduced the experimental $G_{\mathrm{AP,N}}(T)$ for a wide T range from 4.2 to 290 K, while the Shang model gave a fitting curve that showed slight but systematic deviations from the experimental $G_{\mathrm{AP,N}}(T)$ for the entire T range investigated. Furthermore, the Shang model's neglecting the contribution of spin-flip inelastic tunneling via a magnon could not be validated in light of our findings for the experimental $G_{\mathrm{P,N}}(T)$ in Sec. 3.2.3. The essential point of the Shang model is that it explains the T dependence of spin-dependent tunneling conductances, G_{P} and G_{AP}, by only decreasing the spin polarization with increasing T within a framework of spin-conserving elastic tunneling. Thus, the dynamic effect, i.e., the spin-flip inelastic tunneling via a magnon, at finite temperatures is effectively incorporated into the T dependence of the spin polarization, meaning that the Shang model can roughly reproduce the experimental $G_{\mathrm{AP,N}}(T)$ but with slight and systematic deviations. Similarly, the original Zhang model's neglecting the effect of the T dependence of P on elastic tunneling could not be validated even though it could reproduce the experimental $G_{\mathrm{AP,N}}(T)$ as well as the extended Zhang model could do. Regarding the validity of the deduced parameters shown in Table IV, both coefficients a deduced by the extended and original Zhang models are in the expected range, as described in Sec. 3.2.3.

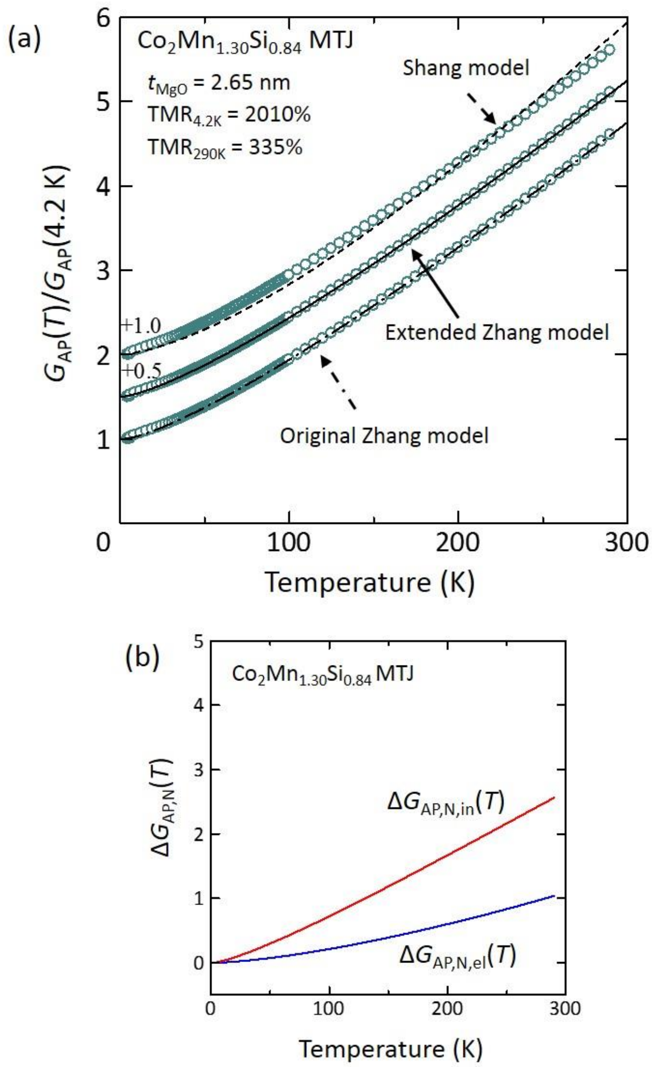

Fig. 3.7. (a) Comparison of fitting curves for $G_{AP}(T)$ normalized by the value at 4.2 K of the CMS MTJ with $Co_2Mn_{1.30}Si_{0.84}$ electrodes (α = 1.30) by the original Zhang model (dashed-dotted line), the extended Zhang model (solid line), and the Shang model (dashed line). The experimental data (open circles) are the same as those of α = 1.30 shown in Figs. 3.1(a) and 3.2(b). The experimental $G_{AP,N}(T)$ data with the fitting curves of the extended Zhang and Shang models have respective offsets of +0.5 and +1.0. (b) Decomposition of the variation of the experimental $G_{AP,N}(T)$ of α = 1.30 CMS MTJ into two components by fitting with the extended Zhang model: One is the inelastic tunneling term $\Delta G_{AP,N,in}(T)$ [Eq. (3.12c)], and the other is the elastic tunneling term $\Delta G_{AP,N,el}(T)$ [Eq. (3.12b)].

TABLE IV. Parameters of η ($K^{-3/2}$), $a = Q\cdot 2S/E_m$ (eV^{-1}), and E_c (meV) for the $Co_2Mn_{1.30}Si_{0.84}$ MTJ shown in Table I deduced from fitting $G_{AP,N}(T)$ by the Shang model, the extended Zhang model, and the original Zhang model. The thus-obtained parameters η and E_c for the antiparallel alignment are represented as η_{AP} and E_c^{AP}.

<table>
<tr><th>α in $Co_2Mn_\alpha Si_{0.84}$</th><th>Fitting model</th><th>η_{AP} ($K^{-3/2}$)</th><th>$a = Q\cdot 2S/E_m$ (eV^{-1})</th><th>E_c^{AP} (meV)</th><th>f(290 K)</th><th>$a\cdot f$(290 K)</th></tr>
<tr><td rowspan="3">1.30</td><td>Shang model</td><td>4.231×10^{-5}</td><td>−</td><td>−</td><td>−</td><td>−</td></tr>
<tr><td>Extended Zhang model</td><td>1.075×10^{-5}</td><td>1.032</td><td>0.178</td><td>4.947</td><td>5.11</td></tr>
<tr><td>Original Zhang model</td><td>−</td><td>1.577</td><td>0.331</td><td>4.330</td><td>6.83</td></tr>
</table>

Figure 3.7(b) decomposes the variation with T in the experimental G_{AP} of $\alpha = 1.30$ MTJ normalized by its value at 4.2 K, i.e., $\Delta G_{AP,N}(T) = G_{AP}(T)/G_{AP}(4.2\ K) - 1$, into a component arising from the elastic tunneling term $\Delta G_{AP,N,el}(T)$ [Eq. (3.12b)] and a component arising from the inelastic tunneling term $\Delta G_{AP,N,in}(T)$ [Eq. (3.12c)]. Although $\Delta G_{AP,N,in}(T)$ was larger than $\Delta G_{AP,N,el}(T)$, these two contributions were more or less comparable. This result of the analysis of the extended Zhang model for $G_{AP,N}(T)$ clearly indicates that the decrease in the TMR ratio at 290 K can be attributed to a static effect, i.e., spin-conserving elastic tunneling with decaying P with T, and a dynamic effect, i.e., spin-flip inelastic tunneling, as described above. This result also suggests the actual P value at 290 K would be higher than the P^{TMR}(290 K) value. Indeed, the P^{TD}(290 K) value for the $\alpha = 1.30$ MTJ as calculated from the η_{AP} value by the fitting of the extended Zhang model (Table IV) was 0.903, which was obviously higher than the P^{TMR}(290 K) of 0.791. Note that tentatively calculated P^{TD}(290 K) value from the η_{AP} value by the fitting of the Shang model was 0.755, which was comparable to the P^{TMR}(290 K). The lower P^{TD}(290 K) value by the Shang model than that by the extended Zhang model was reasonable because the Shang model ignored the contribution of inelastic tunneling. Note also that the P^{TD}(290 K) of 0.799 as calculated from η_P of the extended Zhang model in Sec. III A was much smaller than that as calculated from η_{AP} of the extended Zhang model. This difference in the absolute values of η_P and η_{AP} is ascribed to the simple relation of Eq. (3.6) phenomenologically describing the T dependence of P by a parameter η. Taking into account, however, that the dominant factor that decreases the TMR ratio at 290 K is the T dependence of $G_{AP}(T)$, the semi-quantitative comparison of the P^{TD}(290 K) values estimated from the η_{AP} values (rather than those from the η_P values) is more probable.

Figure 3.8 plots the fitting curves of the extended Zhang model [Eq. (3.12)] for the experimental $G_{AP,N}(T)$ for α ranging from 0.73 to 1.30. The extended Zhang model reproduced the $G_{AP,N}(T)$ for all of the CMS MTJs over a wide T range from 4.2 to 290 K. The best fit parameters and resulting f(290 K) and $a \cdot f$(290 K) are summarized in Table V. The quantities $\gamma_{AP} = G_{AP}(290\ K)/G_{AP}(4.2\ K)$, which represent the degree of the T dependence of G_{AP}, are also shown in Table V. The coefficients a for these MTJs were almost identical. Here, E_c for the antiparallel alignment also increased from 0.063 meV for Mn-deficient α = 0.73 to 0.18 meV for Mn-rich α = 1.30 as E_c for the parallel alignment increased. This dependence led to a slight decrease in the product $a \cdot f$(290 K) as α increased from Mn-deficient to Mn-rich.

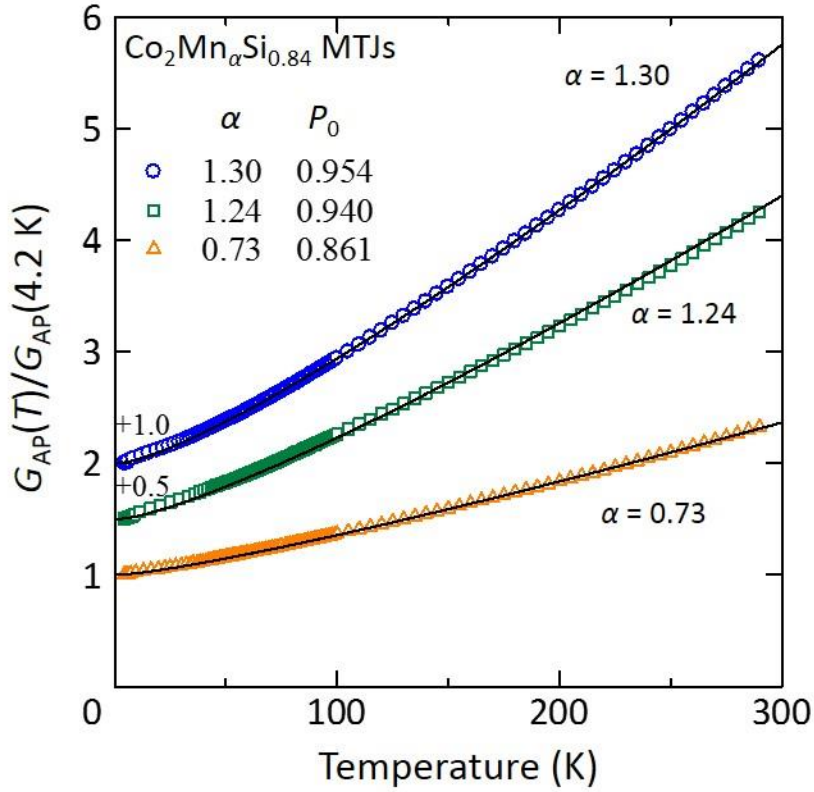

Fig. 3.8. Fitting curves (solid lines) for the experimental $G_{AP}(T)$ normalized by the respective values at 4.2 K by the extended Zhang model [Eq. (3.12)] for the CMS MTJs with various α in $Co_2Mn_\alpha Si_{0.84}$ electrodes. The experimental $G_{AP,N}(T)$ are the same as shown in Fig. 3.2(b) and are shown as open triangles, open squares, and open circles for α = 0.73, 1.24, and 1.30, respectively. The normalized $G_{AP}(T)$ for α = 1.24 and 1.30 have respective offsets of +0.5 and +1.0.

TABLE V. Parameters of η_{AP} ($K^{-3/2}$), $a = Q\cdot 2S/E_m$ (eV^{-1}), and E_c^{AP} (meV) for the CMS MTJs with various α shown in Table I deduced from fitting their respective $G_{AP,N}(T)$ by the extended Zhang model, and the resulting f(290 K) and $a\cdot f$(290 K). The quantities of $\gamma_{AP} = G_{AP}(290\ K)/G_{AP}(4.2\ K)$ and $1/\xi$ defined by $1/\xi = (1 + P_0^2)/(1 - P_0^2)$ are also shown.

α in $Co_2Mn_\alpha Si_{0.84}$	η_{AP} ($K^{-3/2}$)	$a = Q\cdot 2S/E_m$ (eV^{-1})	E_c^{AP} (meV)	f(290 K)	$a\cdot f$(290 K)	γ_{AP}	$1/\xi$
0.73	1.227×10^{-5}	1.014	0.063	5.984	6.07	2.33	6.74
1.24	1.113×10^{-5}	1.004	0.150	5.118	5.14	3.75	16.1
1.30	1.075×10^{-5}	1.032	0.178	4.947	5.11	4.60	21.1

Now let us turn to the origin of the stronger T dependence of $G_{\mathrm{AP,N}}(T)$ for higher P(4.2 K) [Fig. 3.2(b)], resulting in the larger γ_{AP} for higher P(4.2 K). Note that the factor, $[1 + P_0^2(1 - \eta_{\mathrm{AP}}T^{3/2})^2]/(1 - P_0^2) = C_{\mathrm{AP}}(T)$, in $\Delta G_{\mathrm{AP,N,in}}(T)$ [Eq. (3.12c)] can be approximated as $C_{\mathrm{AP}}(T) \approx [1 + P_0^2(1 - 2\eta_{\mathrm{AP}}T^{3/2})]/(1 - P_0^2)$, and the term $2\eta_{\mathrm{AP}}T^{3/2}$ can be neglected in the discussion on the α dependence of γ_{AP} because $2\eta_{\mathrm{AP}}T^{3/2}$ even at 290 K was much smaller than 1. Accordingly, we can replace the factor C_{AP}(T) by a constant $(1 + P_0^2)/(1 - P_0^2) = 1/\xi$, which is just the inverse of the coefficient appearing in $\Delta G_{\mathrm{P,N,in}}(T)$ for $2\eta_{\mathrm{P}}T^{3/2} << 1$. $1/\xi$ increases with P_0 and its values for the MTJs with various α are shown in Table V. This dependence originates from the fact that the inelastic tunneling term in G_{AP} at finite temperatures, $G_{\mathrm{AP,in}}(T)$, is proportional to the sum of $\rho_{\mathrm{M}}^2 + \rho_{\mathrm{m}}^2$, while G_{AP} at $T = 0$ K is proportional to the product $2\rho_{\mathrm{M}}\rho_{\mathrm{m}}$. Furthermore, the term $P_0^2[1 - (1 - \eta_{\mathrm{AP}}T^{3/2})^2]/(1 - P_0^2)$ in $\Delta G_{\mathrm{AP,N,el}}(T)$ [Eq. (3.12b)] can be approximated as $2P_0^2\eta_{\mathrm{AP}}T^{3/2}/(1 - P_0^2)$ because $\eta_{\mathrm{AP}}T^{3/2} << 1$. The coefficient $2P_0^2/(1 - P_0^2) = B_{\mathrm{AP}}$ is also an increasing function of P_0. Note that the coefficient of B_{AP} in $\Delta G_{\mathrm{AP,N,el}}(T)$ is close to the coefficient $1/\xi$ in $\Delta G_{\mathrm{AP,N,in}}(T)$ for high P_0.

We normalized B_{AP}, $1/\xi$, and $a\cdot f$(290 K) for various α by their values at $\alpha = 0.73$ and plotted them as a function of α in Fig. 3.9(a), which clearly shows significant increases in the normalized $1/\xi$ and B_{AP} as α increases from Mn-deficient to Mn-rich. This dependence originated from the increase in P_0, while the product $a\cdot f$(290 K) was almost independent of α even though it slightly decreased with increasing α. Thus, it was revealed that the dominant factors determining the α dependence of γ_{AP} were the coefficient $1/\xi$ in $\Delta G_{\mathrm{AP,N,in}}(T)$ and the almost equivalent coefficient B_{AP} in $\Delta G_{\mathrm{AP,N,el}}(T)$. Because of the similar values of $1/\xi$ and B_{AP} for high P_0, the dominant factor was $1/\xi$ (or equivalently B_{AP}). Figure 3.9(b) plots how γ_{AP} depends on $1/\xi$ for the CMS MTJs with $Co_2Mn_\alpha Si_{0.84}$ electrodes of this paper as well as for the CMS MTJs with $Co_2Mn_\alpha Si_{0.96}$ electrodes reported in Ref. [12], where the $G_{\mathrm{AP,N}}(T)$ data were analyzed using the original Zhang model. We reexamined the $G_{\mathrm{P,N}}(T)$ and $G_{\mathrm{AP,N}}(T)$ data of the $Co_2Mn_\alpha Si_{0.96}$ MTJs by using the extended Zhang model and found that the data could also be consistently explained by it. The almost linear dependence of γ_{AP} on $1/\xi$ for the two series of CMS MTJs also clearly shows the dominant factor for the larger γ_{AP} for higher P(4.2 K) was the coefficient $1/\xi$ which increased with increasing P(4.2 K). This result also indicates that the larger γ_{AP} for higher P(4.2 K) is the intrinsic spin-dependent tunneling property of MTJs [12], which was explained by the extended Zhang model.

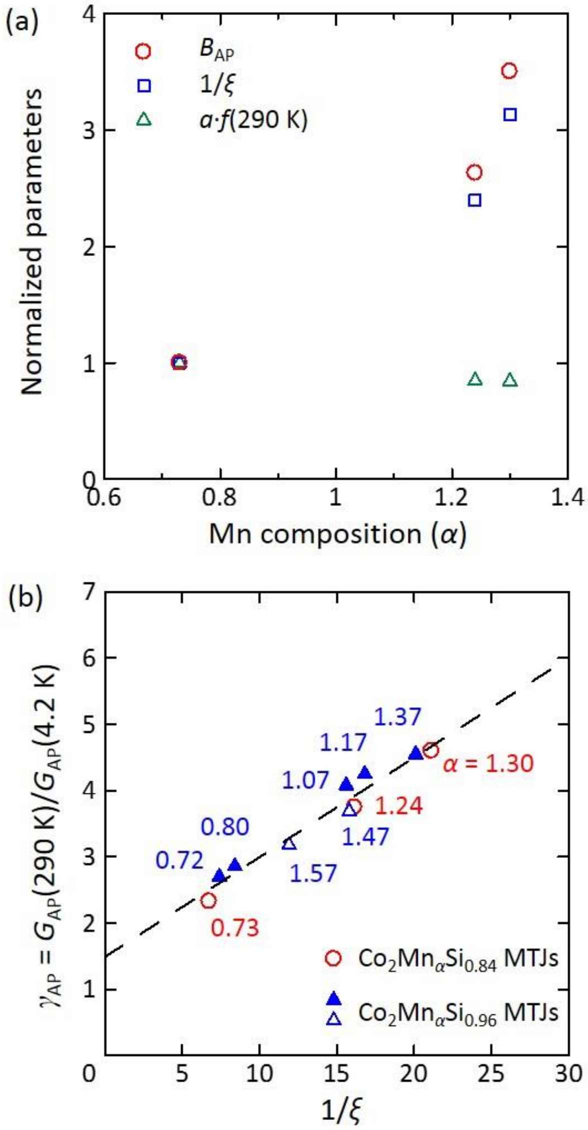

Fig. 3.9. (a) Dependence of the coefficient $B_{AP} = 2P_0^2/(1 - P_0^2)$, the parameter $1/\xi = (1 + P_0^2)/(1 - P_0^2)$, and the product $a \cdot f(290\ K)$ on Mn composition α in $Co_2Mn_\alpha Si_{0.84}$ electrodes, where these values are normalized by the respective values for $\alpha = 0.73$. (b) Dependence of the parameter $\gamma_{AP} = G_{AP}(290\ K)/G_{AP}(4.2\ K)$ on $1/\xi$ for CMS MTJs with $Co_2Mn_\alpha Si_{0.84}$ electrodes (open circles). Dependence of γ_{AP} on $1/\xi$ for CMS MTJs with $Co_2Mn_\alpha Si_{0.96}$ electrodes reported in Ref. [12] are also plotted (solid and open triangles), where solid triangles are for α being smaller than a certain critical α value, α_c, for $Co_2Mn_\alpha Si_{0.96}$ electrodes and open triangles are for α being larger than α_c [12].

3.3.3. Summary

In summary, the experimental $G_{AP}(T)$, including its stronger T dependence for higher P at 4.2 K, was also consistently explained with the extended Zhang model. Note that our findings that both spin-flip inelastic tunneling via a thermally excited magnon and spin-conserving elastic tunneling in which P decays with increasing T play key roles for the T dependence of G_P and G_{AP} are applicable to MTJs with a wide range of P_0. Our findings provide a unified picture of the origin of the T dependence of spin-dependent tunneling conductance of MTJs, including those with highly spin-polarized electrodes.

Chapter 4

Temperature dependence of spin-dependent tunneling conductance of magnetic tunnel junctions with $Co_2(Mn,Fe)Si$ electrodes

4.1. Motivation

As described in the introduction of this dissertation, giant TMR ratios were also demonstrated for CMFS MTJs by Liu *et al.* up to 2610% at 4.2 K and 429% at 290 K for CMFS MTJs with Mn-rich, lightly Fe-doped CMFS electrodes [16]. In addition, CMFS MTJs with (Mn + Fe)-rich, heavily Fe-doped $Co_2Mn_{0.73}Fe_{0.62}Si_{0.84}$ electrodes also exhibited a high TMR ratio of 368% at 290 K which was almost identical to that of 366% at 290 K exhibited by the $Co_2Mn_{1.30}Si_{0.84}$ MTJ although its TMR ratio of 1700% at 4.2 K is much smaller than that of 2110% at 4.2 K of the $Co_2Mn_{1.30}Si_{0.84}$ MTJ. This result indicated that the (Mn + Fe)-rich, heavily Fe-doped $Co_2Mn_{0.73}Fe_{0.62}Si_{0.84}$ MTJ showed a weaker T dependence of the TMR ratio than the $Co_2Mn_{1.30}Si_{0.84}$ MTJ. As discussed in Chapter 3 that the magnon cut-off energy increased with increasing the Mn composition from Mn-deficient to Mn-rich. These experimental results suggest the importance of clarifying the influence of replacing some Mn in CMS electrodes by Fe on the magnon lower cut-off energy in order to fully understand the origin of the *T* dependence of CMS and CMFS MTJs. Thus, we investigated $G_P(T)$ and $G_{AP}(T)$ of CMFS MTJs with $Co_2Mn_{\alpha'}Fe_{\beta'}Si_{0.84}$ electrodes in which α' was fixed at 0.73 and β' was systematically varied from 0 to 0.62.

We introduced smearing effect [Eq. 3.2] in the analysis of the experimental $G_P(T)$ of CMS MTJs in Chapter 3 and showed that it was required because that the variation of $G_P(T)$ became very small, being comparable to the variation in the $S_e(T)$ as P_0 increases. The contribution of the term $S_e(T)$ is closely related to the barrier height (φ) and the barrier thickness (t_{MgO}). The influence of this effect was discussed by analyzing two CMS MTJs with $Co_2Mn_{1.24}Si_{0.84}$ electrodes prepared in the same device fabrication process on the same MTJ epitaxial layer structure having intentionally varied nominal t_{MgO} values due to the wedged MgO barrier structure on a substrate. However, these two MTJs showed slightly different TMR ratios at 4.2 K, i.e., the slightly different P_0 values which could not be ignored for analyzing the $G_P(T)$. Although the experimentally observed features of GP(T) of these two MTJs described above were well explained by taking into consideration the two factors, i.e., the influence of the t_{MgO} value through the smearing factor, $S_e(T)$, and that of P_0 on $G_P(T)$, it is highly required to extract the effect of the smearing factor on $G_P(T)$ in a more direct way. Thus, we systematically investigated the influence of t_{MgO} through the factor of $S_e(T)$ for CMFS MTJs with (Mn + Fe)-rich, lightly Fe-doped $Co_2Mn_{1.19}Fe_{0.16}Si_{0.84}$ electrodes with various t_{MgO} values that showed almost identical TMR ratios at 4.2 K.

In this chapter, we will first show the behaviors of $G_P(T)$ and $G_{AP}(T)$ of the CMFS MTJs with $Co_2Mn_{0.73}Fe_{\beta'}Si_{0.84}$ electrodes, where β' was varied from 0 to 0.62. Then we will analyze these experimental $G_{P,N}(T)$ and $G_{AP,N}(T)$ using the extended Zhang model and compare the fitting results with those of CMS MTJs to clarify the influence of replacing some Mn in the CMS electrode by Fe on the magnon lower cut-off energy of the electrodes. After that, we will present the results of the t_{MgO} dependence of $G_P(T)$ and $G_{AP}(T)$, arising from the smearing effect, of CMFS MTJs with $Co_2Mn_{1.19}Fe_{0.16}Si_{0.84}$ electrodes exhibiting almost identical TMR ratios at 4.2 K.

4.2. Temperature dependence of spin-dependent tunneling conductance of magnetic tunnel junctions with $Co_2Mn_{0.73}Fe_{\beta'}Si_{0.84}$ electrodes

4.2.1. Layer structure

The layer structure (Fig. 4.1) and preparation procedure of the CMFS MTJs were essentially the same as in the case of the $Co_{50}Fe_{50}$ (CoFe)-buffered CMS MTJs described in Chapter 3, except that CMFS thin films were the lower and upper electrodes instead of CMS thin films. Quaternary alloy CMFS layers in the MTJ layer structure were prepared by radio-frequency magnetron cosputtering from nearly stoichiometric CMS, Mn, and Fe targets. The composition of the original CMS film prepared by sputtering from only the CMS target was Mn- and Si-deficient $Co_2Mn_{0.73}Si_{0.84}$. The composition of the CMFS film was determined by inductively coupled plasma analysis with an accuracy of 2−3% for each element, except Si, for which the accuracy was 5%. The film composition was varied by adjusting the relative amounts of sputtered Mn and Fe.

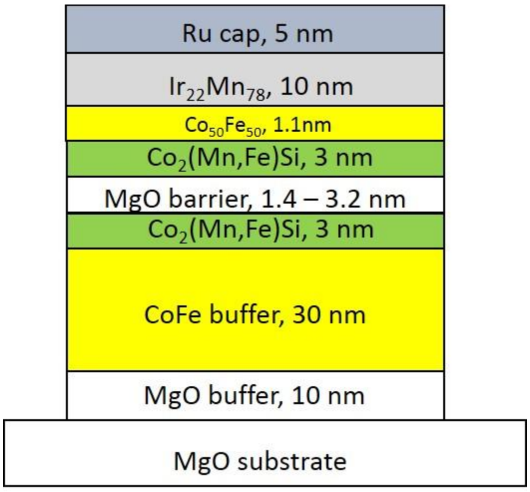

Fig. 4.1. Schematic diagram of the layer structure of $Co_{50}Fe_{50}$ (CoFe)-buffered $Co_2Mn_{\alpha'}Fe_{\beta'}Si$ (CMFS)/MgO/CMFS MTJ (CMFS MTJ) consisting of (from the substrate side) MgO buffer (10 nm)/CoFe buffer (30 nm)/CMFS lower electrode (3 nm)/MgO barrier (1.4−3.2 nm)/CMFS upper electrode (3 nm)/CoFe (1.1 nm)/$Ir_{22}Mn_{78}$ (10 nm)/Ru cap (5 nm), grown on a MgO(001) single-crystal substrate.

4.2.2. Experimental results

Figure 4.2(a) plots the experimental $G_P(T)$ normalized by the respective values at 4.2 K, $G_{P,N}(T) = G_P(T)/G_P(4.2\ K)$, of the CMFS MTJs having $Co_2Mn_{0.73}Fe_{\beta'}Si_{0.84}$ electrodes with various β' ranging from 0 to 0.62. Furthermore, Fig. 3.2(b) plots the experimental $G_{AP}(T)$ normalized by the respective values at 4.2 K, $G_{AP,N}(T) = G_{AP}(T)/G_{AP}(4.2\ K)$. The TMR ratio at 4.2 K of these CMFS MTJs increased with increasing β' from 0 to 0.62 (Table VI). The increase in the TMR ratio has been explained by the enhancement of half-metallicity due to the suppression of $Co_{Mn/Fe}$ antisites for a (Mn + Fe)-rich composition [16]. As a basis for the characterization and analysis of the experimental $G_P(T)$ and $G_{AP}(T)$, we deduced the spin polarization at 4.2 K, P(4.2 K), for these MTJs from the TMR ratios at 4.2 K by assuming the Julliere model [Eq. 3.1]. We also assumed that the lower and upper electrodes had an identical P. Table IV summarizes the deduced P(4.2 K) for the CMFS MTJs. As demonstrated by their high TMR ratios at 4.2 K, the CMFS MTJs with $Co_2Mn_{0.73}Fe_{\beta'}Si_{0.84}$ electrodes exhibited significantly high P values of up to 0.947 at 4.2 K corresponding to the experimentally obtained TMR ratio of 1750% at 4.2 K for $\beta' = 0.62$. We approximated P at 0 K, P_0, by P(4.2 K) in the following analysis. The crucial role of coherent tunneling [34,68] has been experimentally [11] and theoretically [69] demonstrated in CMS MTJs. Thus, the P deduced from Eq. (3.1) is the value determined by ρ_M and ρ_m arising from the electronic states contributing to coherent tunneling [11,17].

TABLE VI. TMR ratios at 4.2 and 290 K of CMFS MTJs with various β' in $Co_2Mn_{0.73}Fe_{\beta'}Si_{0.84}$ electrodes of which $G_{P,N}(T)$ and $G_{AP,N}(T)$ are shown in Fig. 4.2 along with the respective nominal MgO barrier thicknesses (t_{MgO}). The tunneling spin polarizations at 4.2 K, P(4.2 K), deduced from the Julliere model [Eq. (3.1)] with the respective TMR ratios at 4.2 K, are also shown. The tunneling spin polarizations at 0 K, P_0, could be approximated by the respective P(4.2 K) and could be used in the analysis.

β' in $Co_2Mn_{0.73}Fe_{\beta'}Si_{0.84}$	t_{MgO} (nm)	TMR ratio at 4.2 K	TMR ratio at 290 K	P(4.2 K)
0	2.65	574%	178%	0.861
0.27	2.79	1260%	285%	0.929
0.57	2.63	1690%	343%	0.946
0.62	2.51	1750%	355%	0.947

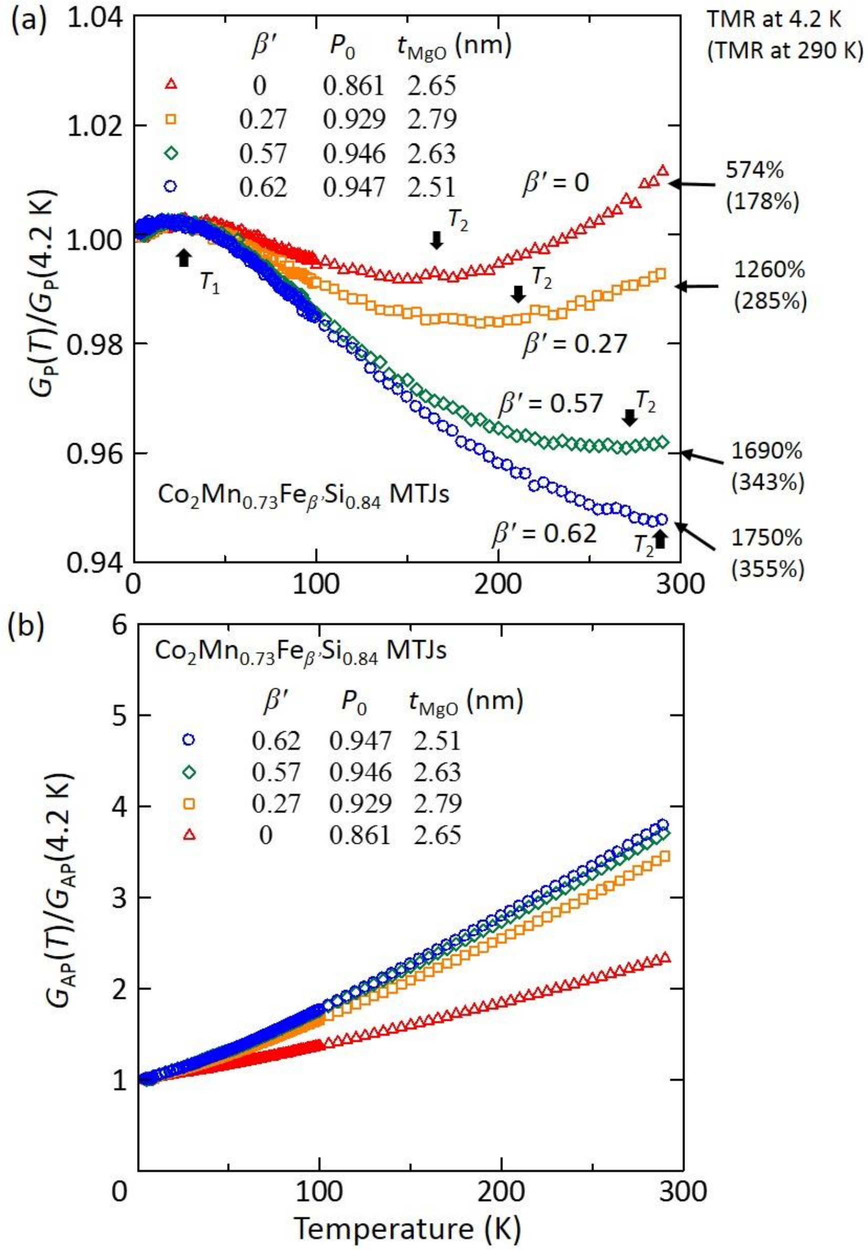

Fig. 4.2. (a) Normalized G_P and (b) G_{AP} as a function of T from 4.2 to 290 K for CMFS MTJs with various β' in $Co_2Mn_{0.73}Fe_{\beta'}Si_{0.84}$ electrodes, where G_P and G_{AP} are normalized by the respective values at 4.2 K.

As shown in Fig. 4.2(a), the $G_{P,N}(T)$ of these CMFS MTJs showed similar features as the CMS MTJs. The first feature is that the $G_{P,N}$ decreased with increasing T from $T = T_1$ of about 30 K to $T = T_2$ ranging from about 162 K for $\beta' = 0$ to 285 K for $\beta' = 0.62$. Then, it increased for $T > T_2$. The second feature is that T_2 increased as the TMR ratio at 4.2 K increased or equivalently P(4.2 K) increased. The third feature is that the maximum decrease in the experimental $G_{P,N}$ at T_2, defined as $\Delta G_{P,N}(T_2) = G_{P,N}(T_2) - 1$ increased in magnitude as P(4.2 K) increased.

Note that the experimental $G_{AP,N}(T)$ of the $\beta' = 0.57$ and $\beta' = 0.62$ MTJs were almost overlapped with each other because the TMR ratios of these two MTJs were in good agreement within 4% at both 4.2 K and 290 K. However, the $G_{P,N}(T)$ of these two MTJs showed a clear difference, which can be explained by the difference in the smearing effect arising from the difference in their t_{MgO} values.

4.2.3. Analysis and discussion

Figure 4.3 plots the fitting curves of the extended Zhang model [Eq. (3.7)] for the experimental $G_{P,N}(T)$ shown in Fig. 4.2(a). The extended Zhang model reproduced the apparently complicated $G_{P,N}(T)$ for a wide T range except for $T < T_1$. The parameters giving the best fit, including η_P, $a = Q \cdot 2S/E_m$, and E_c^P, where η_P and E_c^P are η and E_c for the parallel alignment, and the resulting f(290 K) and $a \cdot f$(290 K) are summarized in Table VII. The deduced parameters for these CMFS MTJs were also in the reasonable range. Although the deduced η_P values for $\beta' = 0$ to 0.62 did not show a clear dependence on β', E_c^P showed a distinct dependence on β' and increased with β' from $E_c^P = 0.31$ meV for (Mn + Fe)-deficient $\beta' = 0$ to $E_c^P = 0.87$ meV for (Mn + Fe)-rich $\beta' = 0.62$. This increase in E_c^P with β' suggests an increase in spin wave stiffness [70] with increasing β'.

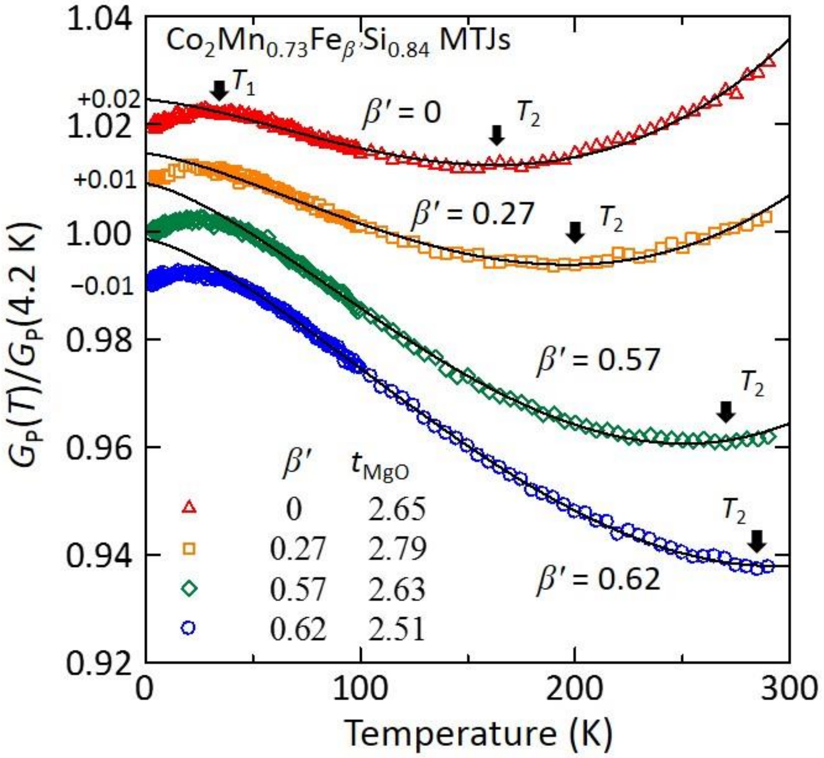

Fig. 4.3. Fitting curves of the extended Zhang model (solid lines) [Eq. (3.7)] for the experimental $G_P(T)$ normalized by the respective values at 4. 2 K of the CMFS MTJs with β' = 0 (open triangles), 0.27 (open squares), 0.57 (open diamonds), and 1.30 (open circles) in $Co_2Mn_{0.73}Fe_{\beta'}Si_{0.84}$ electrodes. The experimental data of $G_P(T)$ are the same as shown in Fig. 4.2(a). The data of the normalized $G_P(T)$ for β' = 0, 0.27, and 0.62 have respective offsets of +0.02, +0.01, and -0.01.

TABLE VII. Parameters of η ($K^{-3/2}$), $a = Q \cdot 2S/E_m$ (eV^{-1}), E_c (meV), and c_0 for the CMFS MTJs with various β' shown in Table VI deduced from fitting their respective normalized $G_P(T)$ [= $G_P(T)/G_P(4.2\ K)$] by the proposed extended Zhang model, and the resulting f(290 K) [Eq. (3.3f)] and $a \cdot f$(290 K). The thus-obtained parameters η and E_c for the parallel alignment are represented as η_P and E_c^P.

β' in $Co_2Mn_{0.73}Fe_{\beta'}Si_{0.84}$	Fitting model	η_P ($K^{-3/2}$)	$a = Q \cdot 2S/E_m$ (eV^{-1})	E_c^P (meV)	f(290 K)	$a \cdot f$(290 K)	c_0
0	Extended Zhang model	3.699×10^{-5}	3.004	0.311	4.392	13.2	0.005
0.27		3.146×10^{-5}	3.004	0.378	4.198	12.6	0.005
0.57		3.991×10^{-5}	3.008	0.530	3.863	11.6	0.009
0.62		3.770×10^{-5}	3.008	0.872	3.372	10.1	0.009

Figure 4.4 plots the fitting curves of the extended Zhang model [Eq. (3.12)] for the experimental $G_{AP,N}(T)$ for β' ranging from 0 to 0.62. The extended Zhang model well reproduced the $G_{AP,N}(T)$ for all of the CMFS MTJs over a wide T range from 4.2 to 290 K. The best fit parameters and resulting f(290 K) and $a \cdot f$(290 K) are summarized in Table VIII. The quantities $\gamma_{AP} = G_{AP}(290\ K)/G_{AP}(4.2\ K)$, which represent the degree of the T dependence of G_{AP}, are also shown in Table VIII. The coefficients a for these MTJs were almost identical. Here, E_c for the antiparallel alignment also increased from 0.063 meV for (Mn + Fe)-deficient β' = 0 to 0.35 meV for (Mn + Fe)-rich β' = 0.62 as E_c for the parallel alignment increased. This dependence led to a decrease in the product $a \cdot f$(290 K) as β' increased from (Mn + Fe)-deficient to (Mn + Fe)-rich.

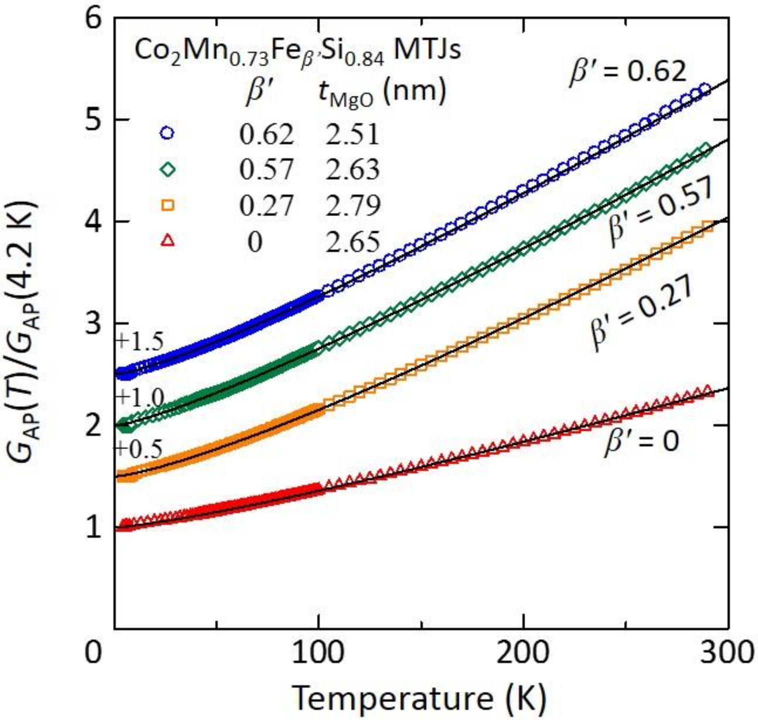

Fig. 4.4. Fitting curves (solid lines) for the experimental $G_{AP}(T)$ normalized by the respective values at 4.2 K by the extended Zhang model [Eq. (3.12)] for the CMFS MTJs with various β' in $Co_2Mn_{0.73}Fe_{\beta'}Si_{0.84}$ electrodes. The experimental $G_{AP,N}(T)$ are the same as shown in Fig. 4.2(b) and are shown as open triangles, open squares, open diamond, and open circles for β' = 0, 0.27, 0.57, and 0.62, respectively. The normalized $G_{AP}(T)$ for for β' = 0.27, 0.57, and 0.62 have respective offsets of +0.5, +1.0 and +1.5.

TABLE VIII. Parameters of η_{AP} ($K^{-3/2}$), $a = Q\cdot 2S/E_m$ (eV^{-1}), and E_c^{AP} (meV) for the CMFS MTJs with various β' in $Co_2Mn_{0.73}Fe_{\beta'}Si_{0.84}$ electrodes shown in Table VI deduced from fitting their respective $G_{AP,N}(T)$ by the extended Zhang model, and the resulting f(290 K) and $a\cdot f$(290 K). The quantities of $\gamma_{AP} = G_{AP}(290\text{ K})/G_{AP}(4.2\text{ K})$ and $1/\xi$ defined by $1/\xi = (1 + P_0^2)/(1 - P_0^2)$ are also shown.

β' in $Co_2Mn_{0.73}Fe_{\beta'}Si_{0.84}$	η_{AP} ($K^{-3/2}$)	$a = Q\cdot 2S/E_m$ (eV^{-1})	E_c^{AP} (meV)	f(290 K)	$a\cdot f$(290 K)	γ_{AP}	$1/\xi$
0	1.227×10^{-5}	1.014	0.063	5.984	6.07	2.33	6.74
0.27	1.056×10^{-5}	1.009	0.104	5.483	5.53	3.45	13.6
0.57	1.000×10^{-5}	1.074	0.324	4.353	4.67	3.70	17.9
0.62	1.000×10^{-5}	1.075	0.345	4.290	4.61	3.78	18.5

Now let us discuss the influence of replacing some Mn in the CMS electrode by Fe on the magnon lower cut-off energy of the electrode. Figure 4.5 plots the Mn+Fe composition, δ, dependence of the obtained parameters E_c^{P} and E_c^{AP} of the CMS and CMFS MTJs. It was found that the E_c^{P} and E_c^{AP} values of the CMFS MTJs increased with increasing the (Mn + Fe) composition, $\delta = \alpha' + \beta'$ (α' = 0.73 fixed), by increasing β' from E_c^{AP} =0.063 meV (E_c^{P} = 0.31 meV) for δ-deficient δ = 0.73 to E_c^{AP} =0.35 meV (E_c^{P} = 0.87 meV) for δ-rich δ = 1.35. This dependence of E_c values on δ was similar to that of the E_c values on the Mn composition, α, in the $Co_2Mn_{\alpha}Si_{0.84}$ electrodes described in Chapter 3. Note that, although the E_c values of the lightly Fe-doped CMFS with δ = 1.0 ($Co_2Mn_{0.73}Fe_{0.27}Si_{0.84}$) was comparable with that of the CMS MTJ having a comparable α value as δ = 1.0, the E_c values of the heavily Fe-doped CMFS MTJs with δ = 1.30 to 1.35 ($Co_2Mn_{0.73}Fe_{0.57}Si_{0.84}$ and $Co_2Mn_{0.73}Fe_{0.62}Si_{0.84}$) were distinctly larger than the CMS MTJ having a comparable α value of 1.30 as δ = 1.30 to 1.35. Thus, it was revealed that the E_c values, which influence the degree of the T dependence of G_P and G_{AP}, are correlated with the transition metal Y in Co_2YSi.

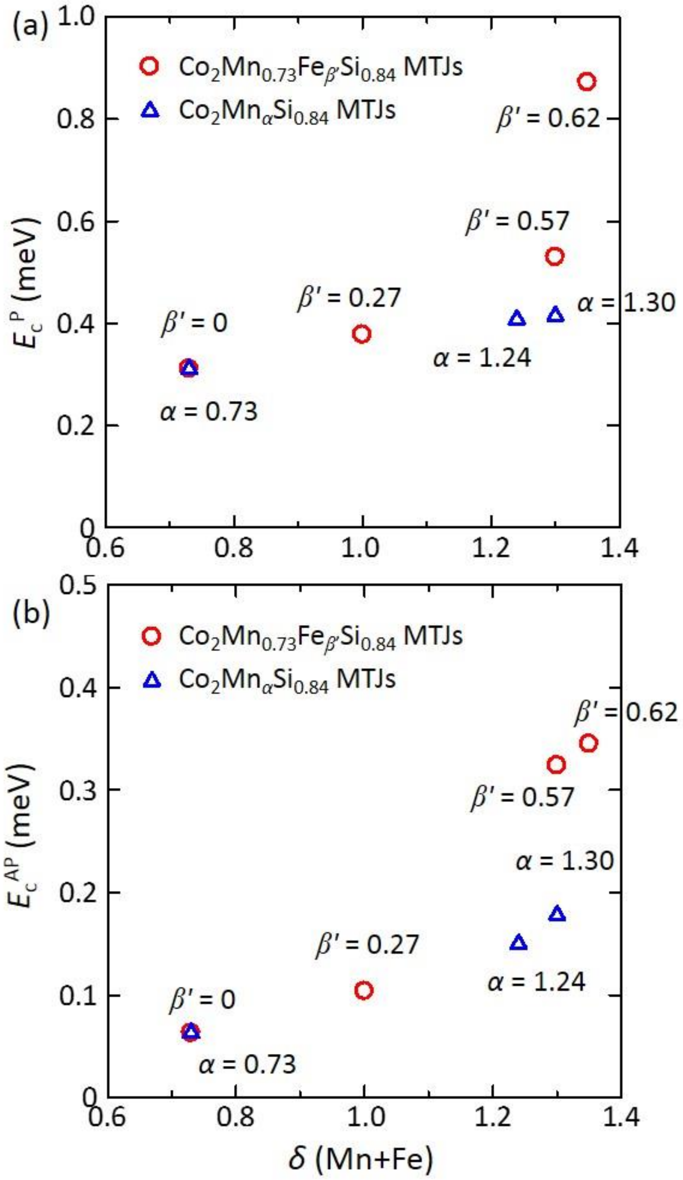

Fig. 4.5. Dependence of the coefficient E_c, representing the magnon cut-off energy, for both parallel and anti-parallel allignments, E_c^{P} and E_c^{AP}, on the (Mn + Fe) compositions in the CMS and CMFS electrodes.

Figure 4.6 plots how the γ_{AP} depends on $1/\xi$ for the CMFS MTJs with $Co_2Mn_{0.73}Fe_{\beta'}Si_{0.84}$ electrodes, the CMS MTJs with $Co_2Mn_{\alpha}Si_{0.84}$ electrodes, and the CMS MTJs with $Co_2Mn_{\alpha}Si_{0.96}$ electrodes [12], where $1/\xi = (1 + P_0^2)/(1 - P_0^2)$ and P_0 was was approximated by P(4.2 K) in the plot. The γ_{AP} versus $1/\xi$ plot of the CMFS MTJs with $Co_2Mn_{0.73}Fe_{\beta'}Si_{0.84}$ electrodes showed an almost linear dependence and its plot was almost overlapped with the linear dependence of the γ_{AP} versus $1/\xi$ plot of the CMS MTJs, except for the slightly smaller values for the heavily Fe-doped CMFS MTJs. The almost linear dependence of the γ_{AP} versus $1/\xi$ plot for these two series of CMS MTJs and one series of CMFS MTJs indicated that the dominant factor for the larger γ_{AP} for higher P(4.2 K) was the coefficient $1/\xi$ which increased with increasing P(4.2 K). The larger spin wave stiffness, represented by the larger E_c values, of the δ-rich and heavily Fe-doped CMFS than the Mn-rich CMS only provided a slight effect of reducing the degree of the T dependence of G_{AP} and that of TMR ratio in the case of MTJs with CMS and CMFS MTJs. This is because the effective factor E_c on $G(T)$ is $f(E_c)$ which is weakly dependent on the E_c values.

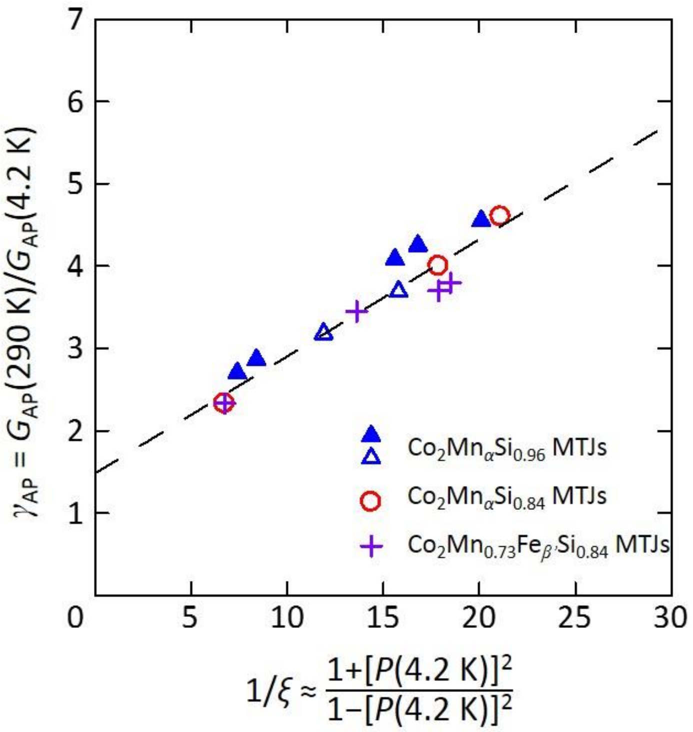

Fig. 4.6. Dependence of the parameter $\gamma_{AP} = G_{AP}(290\ K)/G_{AP}(4.2\ K)$ on $1/\xi = (1 + P_0^2)/(1 - P_0^2)$ and P_0 was approximated by $P(4.2\ K)$ for CMFS MTJs with $Co_2Mn_{0.73}Fe_{\beta'}Si_{0.84}$ electrodes (crosses), CMS MTJs with $Co_2Mn_{\alpha}Si_{0.84}$ electrodes (open circles), and the CMS MTJs with $Co_2Mn_{\alpha}Si_{0.96}$ electrodes (solid and open triangles), where solid triangles are for α being smaller than a certain critical α value, α_c, for $Co_2Mn_{\alpha}Si_{0.96}$ electrodes and open triangles are for α being larger than α_c [12].

4.3. Effect of MgO tunnel barrier thickness on the temperature dependence of G_P and G_{AP} of high-quality MTJs

4.3.1. Experimental results

Now let us turn to the effect of MgO tunnel barrier thickness on the T dependence of G_P and G_{AP} of MTJs. To do so, we investigated $G_P(T)$ and $G_{AP}(T)$ of high-quality CMFS MTJs prepared in the same device fabrication process on the same MTJ epitaxial layer structure with systematically varied t_{MgO} which featured almost identical giant TMR ratios at both 4.2 and 290 K. Thus, these MTJs exhibiting the almost identical giant TMR ratios are an ideal system to investigate the effect of t_{MgO} on the T dependence of G_P and G_{AP}. Figures 4.7(a) and 4.7(b) plot the experimental $G_P(T)$ and $G_{AP}(T)$ normalized by the respective values at 4.2 K, $G_{P,N}(T) = G_P(T)/G_P(4.2\text{ K})$ and $G_{AP,N}(T) = G_{AP}(T)/G_{AP}(4.2\text{ K})$, of the CMFS MTJs with various t_{MgO} values ranging from 2.38 nm to 2.96 nm. These MTJs showed giant TMR ratios of 2180% ± 1.6% at 4.2 K and 352% ± 1.6% at 290 K [Table IX]. Although the mean derivation of the TMR ratios of these MTJs was only within 1.6%, $G_{P,N}(T)$ of these MTJs showed a clear difference, which is ascribed to the various degree of the smearing effect of the Fermi distribution on $G_P(T)$ arising from the various t_{MgO} values. While the $G_{AP,N}(T)$ of these MTJs were almost overlapped with each other, indicating that the $G_{AP}(T)$ was almost independent of t_{MgO}. This is reasonable because the main factor that leads to the stronger T dependence of G_{AP} for an MTJ featuring a higher P_0 is spin-flip inelastic tunneling, which becomes larger for a larger P_0. Furthermore, the magnitude of the smearing factor is negligibly small compared with the significant increase in $G_{AP,N}(T)$ of MTJs with a high P_0 due to inelastic tunneling. While the increase in $G_{P,N}(T)$ of MTJs with a high P_0 is significantly suppressed, resulting in a significant influence of the smearing effect.

TABLE IX. TMR ratios at 4.2 and 290 K of CMFS MTJs with $Co_2Mn_{1.19}Fe_{0.16}Si_{0.84}$ electrodes of which $G_{P,N}(T)$ and $G_{AP,N}(T)$ are shown in Fig. 4.7 along with the respective nominal MgO barrier thicknesses (t_{MgO}). The tunneling spin polarizations at 4.2 K, P(4.2 K), deduced from Eq. (3.1) with the respective TMR ratios at 4.2 K, are also shown. The tunneling spin polarizations at 0 K, P_0, could be approximated by the respective P(4.2 K) and could be used in the analysis.

t_{MgO} (nm)	TMR ratio at 4.2 K	TMR ratio at 290 K	P(4.2 K)
2.38	2190%	344%	0.957
2.65	2130%	351%	0.956
2.96	2230%	360%	0.958

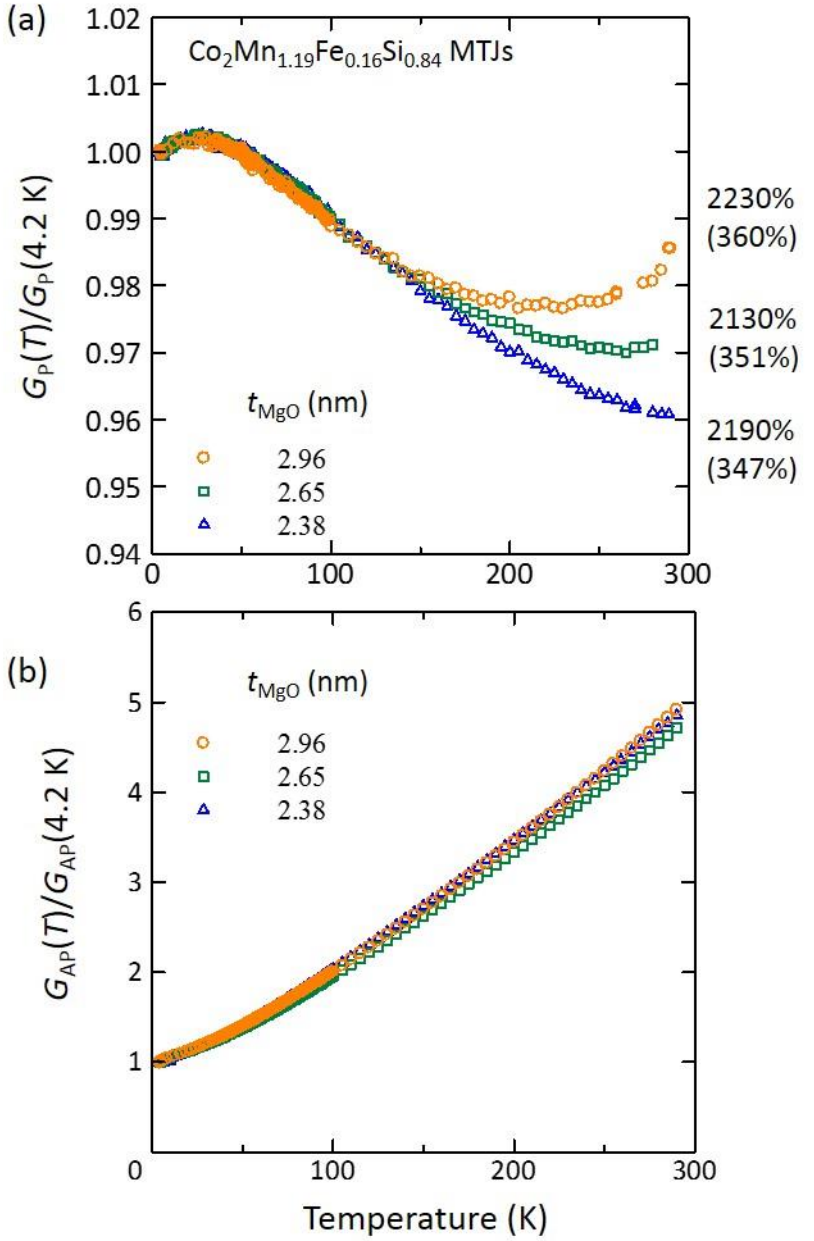

Fig. 4.7. (a) Normalized G_P and (b) G_{AP} as a function of T from 4.2 to 290 K for CMFS MTJs with lightly Fe-doped $Co_2Mn_{1.19}Fe_{0.16}Si_{0.84}$ electrodes prepared in the same device fabrication process on the same MTJ epitaxial layer structure but having different nominal t_{MgO} values of 2.38, 2.65 and 2.96 nm. Here, $G_P(T)$ and $G_{AP}(T)$ are normalized by the respective values at 4.2 K.

4.3.2. Analysis and discussion

Figure 4.8 plots the fitting curves of Eq. 3.7 for the $G_{P,N}(T)$ shown in Fig. 4.7(a). In the fitting, we first obtained the parameters $Q{\cdot}2S/E_m$, E_c^P, η_P and constant c_0 for the MTJ with a t_{MgO} of 2.65 nm from fitting the experimental $G_{P,N}(T)$ using the extended Zhang model (Eq. 3.7) and by assuming a φ value of 3.5 eV and the nominal t_{MgO} value of 2.65 nm for the coefficient C in $S_e(T) = CT/\sin(CT)$ with $C = 1.387 \times 10^{-3} t_{MgO}/\varphi^{1/2}$ [64]. Then it is reasonable to assume the other two MTJs with different t_{MgO} had the identical $Q{\cdot}2S/E_m$, E_c^P, η_P and φ values as those obtained for the t_{MgO} = 2.65 nm MTJ. This is because all these MTJs were prepared on the same epitaxial layer structure and in the same device process, and featured almost identical TMR ratios. Next, fitting for the $G_{P,N}(T)$ of the other two MTJs were done with two fitting parameters of a constant c_0 and a coefficient C. We deduced the t_{MgO} values of these two MTJs from the obtained C values. The deduced t_{MgO} values for these two MTJs from the obtained C values are in good agreement with the respective nominal values as listed in Table X. This result indicated the fitting was reasonably done. It also indicates the systematic change in the behavior of $G_P(T)$ for the various t_{MgO} could be ascribed to the smearing effect.

TABLE X. Parameters of η ($K^{-3/2}$), $a = Q{\cdot}2S/E_m$ (eV^{-1}), E_c (meV), and c_0 for the CMFS MTJs with lightly Fe-doped $Co_2Mn_{1.19}Fe_{0.16}Si_{0.84}$ electrodes shown in Table IX deduced from fitting their respective normalized $G_P(T)$ [= $G_P(T)/G_P$(4.2 K)] by the extended Zhang model. The thus-obtained parameters η and E_c for the parallel alignment are represented as η_P and E_c^P.

Nominal t_{MgO} (nm)	P(4.2 K)	Fitting model	η_P ($K^{-3/2}$)	$a = Q{\cdot}2S/E_m$ (eV^{-1})	E_c^P (meV)	c_0	t_{MgO} from fitting (nm)
2.38	0.957					0.005	2.36
2.65	0.956	Extended Zhang model	2.935×10^{-5}	3.006	1.06	0.007	2.65
2.96	0.958					0.008	2.97

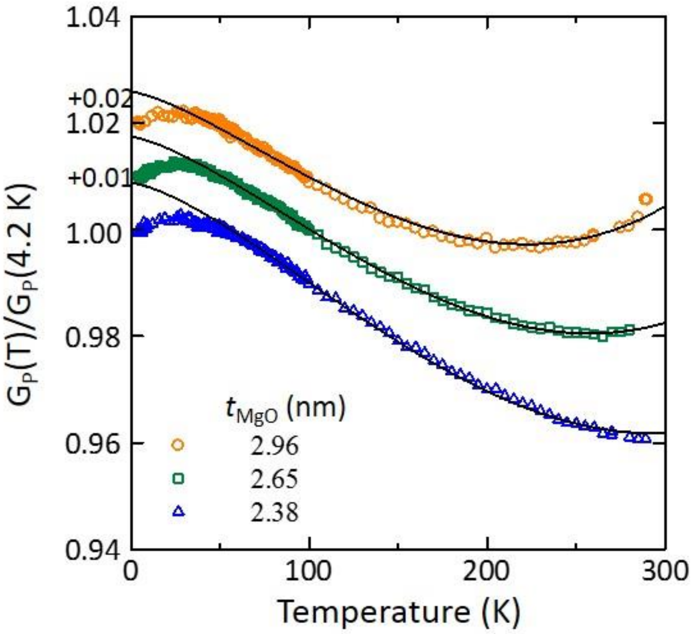

Fig. 4.8. Fitting curves of the extended Zhang model (solid lines) [Eq. (3.7)] for the experimental $G_P(T)$ normalized by the respective values at 4. 2 K of the CMFS MTJs with lightly Fe-doped $Co_2Mn_{1.19}Fe_{0.16}Si_{0.84}$ electrodes prepared in the same device fabrication process on the same MTJ epitaxial layer structure but having different nominal t_{MgO} values of 2.38 (open triangles), 2.65 (open squares) and 2.96 nm (open circles). The experimental data of $G_P(T)$ are the same as shown in Fig. 4.7(a). The data of the normalized $G_P(T)$ for t_{MgO} = 2.65 and 2.96 nm have respective offsets of +0.02 and +0.01.

We will now discuss the $G_{AP}(T)$ of these MTJs. No significant dependence of the $G_{AP}(T)$ of these MTJs on the t_{MgO} value could be ascribed to that the smearing factor at T = 290 K is at most 1.071 for the t_{MgO} =2.91 nm MTJ, while $G_{AP,N}$(290 K) is about 5, which is larger by two orders of magnitude. This resulted in no significant contribution of the smearing factor to $G_{AP,N}(T)$. Thus, we fitted the experimental $G_{AP,N}(T)$ of the CMFS MTJs with lightly Fe-doped $Co_2Mn_{1.19}Fe_{0.16}Si_{0.84}$ electrodes exhibiting almost identical TMR ratios at 4.2 K and 290 K but having different nominal t_{MgO} values using the extended Zhang model [Eq. (3.12)] without the smearing factor $S_e(T)$. Figure 4.9 plots the fitting curves for the experimental $G_{AP,N}(T)$ for the MTJs with various t_{MgO} values. The thus-obtained parameters were shown in Table XI, that $\eta_{AP} = 1.127 \times 10^{-5} \pm 3\%$, $a = Q\cdot 2S/E_m = 1.013 \pm 1\%$, and E_c^{AP} = 0.200 ± 8%. All the parameters showed a very small scattering, i.e., the obtained fitting parameters were almost identical between these MTJs, indicating that the fitting without the smearing factor was reasonable. Thus, it was concluded that the smearing effect is negligible in $G_{AP}(T)$ of these MTJs showing giant TMR ratios.

TABLE XI. Parameters of η_{AP} ($K^{-3/2}$), $a = Q\cdot 2S/E_m$ (eV^{-1}), and E_c^{AP} (meV) for the CMFS MTJs with lightly Fe-doped $Co_2Mn_{1.19}Fe_{0.16}Si_{0.84}$ electrodes, exhibiting almost identical TMR ratios at 4.2 K but having different nominal t_{MgO} values, deduced from fitting their respective $G_{AP,N}(T)$ by the extended Zhang model, and the resulting f(290 K) and $a\cdot f$(290 K). The quantities of $\gamma_{AP} = G_{AP}(290\ K)/G_{AP}(4.2\ K)$ and $1/\xi$ defined by $1/\xi = (1 + P_0^2)/(1 - P_0^2)$ are also shown.

Nominal t_{MgO} (nm)	η_{AP} ($K^{-3/2}$)	$a = Q\cdot 2S/E_m$ (eV^{-1})	E_c^{AP} (meV)	f(290 K)	$a\cdot f$(290 K)	γ_{AP}	$1/\xi$
2.38	1.101×10^{-5}	1.019	0.177	4.953	5.05	4.85	22.9
2.65	1.102×10^{-5}	1.024	0.215	4.759	4.87	4.71	22.3
2.96	1.177×10^{-5}	0.997	0.209	4.787	4.77	4.92	23.3

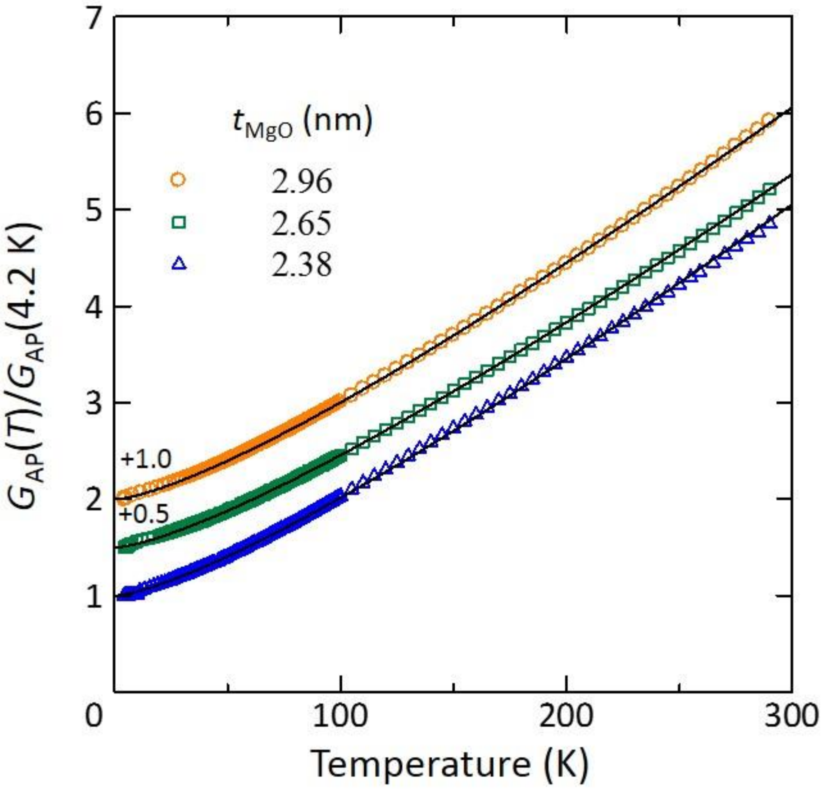

Fig. 4.9. Fitting curves (solid lines) for the experimental $G_{AP}(T)$ normalized by the respective values at 4.2 K by the extended Zhang model [Eq. (3.12)] for the CMFS MTJs with lightly Fe-doped $Co_2Mn_{1.19}Fe_{0.16}Si_{0.84}$ electrodes exhibiting almost identical TMR ratios at 4.2 K but having different nominal t_{MgO} values. The experimental $G_{AP,N}(T)$ are shown as open triangles, open squares, and open circles for t_{MgO} = 2.38, 2.65, and 2.96 nm, respectively. The normalized $G_{AP}(T)$ for t_{MgO} = 2.65 and 2.96 have respective offsets of +0.5 and +1.0.

4.4. Summary

We investigated the T dependence of spin-dependent tunneling conductances of CMFS MTJs with $Co_2Mn_{\alpha'}Fe_{\beta'}Si_{0.84}$ electrodes having a fixed Mn composition of α' = 0.73 and various Fe compositions of β' ranging from 0 to 0.62. We found that the magnon lower cut-off energy, E_c^P and E_c^{AP}, of (Mn + Fe)-rich CMFS MTJs with the Fe compositions, β', being comparable to α', i.e., CMFS with (β' = 0.57, $\alpha' + \beta'$ = 1.30) and (β' = 0.62, $\alpha' + \beta'$ = 1.35), were larger than those of Mn-rich CMS MTJs with $Co_2Mn_{\alpha}Si_{0.84}$ electrodes with α = 1.30. Thus, it was revealed that the magnon lower cut-off energy, which influences the T dependence of the TMR ratio, depends on the constituent transition-metal element Y in half-metallic Co_2YSi Heusler alloys. We also investigated the influence of t_{MgO} on $G_P(T)$ and $G_{AP}(T)$ of MTJs. To do so, we investigated high-quality CMFS MTJs prepared in the same device fabrication process on the same MTJ epitaxial layer structure that exhibited almost identical TMR ratios at 4.2 K that had systematically varied t_{MgO} values. We observed a distinct effect of the MgO tunnel barrier thickness on the $G_P(T)$ of MTJs, and contrastingly, no significant effect on the G_{AP} of MTJs with highly spin-polarized electrodes. These results were well explained by the extended Zhang model.

Chapter 5

Conclusion

We investigated the key tunneling mechanisms that determine the temperature (T) dependence of the spin-dependent tunneling conductances, G_P and G_{AP}, of MTJs. To do so, we measured the $G_P(T)$ and $G_{AP}(T)$ of high-quality CMS/MgO/CMS MTJs featuring systematically varied tunneling spin polarizations at 4.2 K [P(4.2 K)] (α in the $Co_2Mn_\alpha Si_{0.84}$ electrodes was varied) that exhibited giant TMR ratios. Although the T dependence of the normalized G_P [$G_{P,N}(T) = G_P(T)/G_P$(4.2 K)] was significantly weak compared with that of the normalized G_{AP} [= $G_{AP}(T)/G_{AP}$(4.2 K)], $G_{P,N}$ showed a notable T dependence in which it decreased with increasing T from T_1 of about 30 K to T_2 ranging from about 162 to 237 K, wherein T_2 depended on α; then it increased for $T > T_2$. Furthermore, T_2 increased and the maximum decrease in $G_{P,N}$ at T_2 increased as P(4.2 K) increased. These features indicated that an analysis of the experimental $G_{P,N}(T)$ is critical to elucidating the origin of the T dependence of the spin-dependent tunneling conductance. To explain these features of $G_{P,N}(T)$, we developed an extension of the Zhang model for $G_P(T)$ and $G_{AP}(T)$ that took into account both spin-conserving elastic tunneling wherein P decreases with increasing T, and in turn decreases G_P with T, and spin-flip inelastic tunneling via a thermally excited magnon that increases G_P with T. Accordingly, the complicated nonmonotonic behavior of the experimental $G_{P,N}(T)$ could be fitted with reasonable values of the parameters of the proposed model. The observed P(4.2 K) dependence of $G_{P,N}(T)$ was also consistently explained by the proposed model through a decrease in the contribution of spin-flip inelastic tunneling with increasing P(4.2 K). The normalized $G_{AP}(T)$, including its stronger T dependence for higher P(4.2 K), was also consistently explained. The proposed model provides a comprehensive understanding of $G_P(T)$ and $G_{AP}(T)$ of not only half-metallic MTJs but also MTJs with a wide range of P at 0 K.

We also investigated the T dependence of G_P and G_{AP} of CMFS MTJs with $Co_2Mn_{\alpha'}Fe_{\beta'}Si_{0.84}$ electrodes having a fixed Mn composition of α' = 0.73 and various Fe compositions of β' ranging from 0 to 0.62. We found that the magnon lower cut-off energy, E_c^{P} and E_c^{AP}, of (Mn + Fe)-rich CMFS MTJs with the Fe compositions, β', being comparable to α', i.e., CMFS with (β' = 0.57, α' + β' = 1.30) and (β' = 0.62, α' + β' = 1.35), was larger than those of Mn-rich CMS MTJs with $Co_2Mn_{\alpha}Si_{0.84}$ electrodes with α = 1.30. Thus, it was revealed that the magnon lower cut-off energy, which influences the T dependence of the TMR ratio, depends on the constituent transition-metal element Y in half-metallic Co_2YSi Heusler alloys.

Acknowledgements

I would like to express my deepest gratitude to Professor Masafumi Yamamoto for his constant support, supervision, thoughtful discussion and encouragement throughout my study in the Laboratory of Nanoscale Electron Devices. This work could not have been accomplished without his invaluable support and guidance.

I gratefully acknowledge Professor Tetsuya Uemura for his constant support, thoughtful discussion, and kind help during my doctoral course study.

I am grateful to Professor Akihisa Tomita and Professor Yasuo Takahashi for reviewing this dissertation and offering their helpful comments.

I want to give many thanks to senior students Hong-xi Liu, Yusuke Honda, Takafumi Akiho, and Kidist Moges Ayele for their guidance in operating the apparatuses and for valuable discussions. I also want to thank the other members of the Laboratory of Nanoscale Electron Devices for their collaborations in the experiments.

I would also like to thank my parents and fiancée for their heartfelt support, understanding and encouragement during my study in Japan.

Finally, I convey my great gratitude to the China Scholarship Council for the financial support during my study as a Doctoral student.

Reference

[1] S. A. Wolf, D. D. Awschalom, R. A. Buhrman, J. M. Daughton, S. von Molnár, M. L. Roukes, A. Y. Chtchelkanova, and D. M. Treger, Science **294**, 1488 (2001).

[2] I. Žutić, J. Fabian, and S. Das Sarma, Rev. Mod. Phys. **76**, 323 (2004).

[3] R. A. de Groot, F. M. Mueller, P. G. van Engen, and K. H. J. Buschow, Phys. Rev. Lett. **50**, 2024 (1983).

[4] C. Felser, G. H. Fecher, and B. Balke, Angew. Chem., Int. Ed. **46**, 668 (2007).

[5] K. Inomata, S. Okamura, R. Goto, and N. Tezuka, Jpn. J. Appl. Phys. **42**, L419 (2003).

[6] S. Kämmerer, A. Thomas, A. Hütten, and G. Reiss, Appl. Phys. Lett. **85**, 79 (2004).

[7] Y. Sakuraba, M. Hattori, M. Oogane, Y. Ando, H. Kato, A. Sakuma, T. Miyazaki, and H. Kubota, Appl. Phys. Lett. **88**, 192508 (2006).

[8] T. Ishikawa, T. Marukame, H. Kijima, K.-i. Matsuda, T. Uemura, M. Arita, and M. Yamamoto, Appl. Phys. Lett. **89**, 192505 (2006).

[9] T. Ishikawa, H.-x. Liu, T. Taira, K.-i. Matsuda, T. Uemura, and M. Yamamoto, Appl. Phys. Lett. **95**, 232512 (2009).

[10] M. Yamamoto, T. Ishikawa, T. Taira, G.-f. Li, K.-i. Matsuda, and T. Uemura, J. Phys.: Condens. Matter **22**, 164212 (2010).

[11] H.-x. Liu, Y. Honda, T. Taira, K.-i. Matsuda, M. Arita, T. Uemura, and M. Yamamoto, Appl. Phys. Lett. **101**, 132418 (2012).

[12] G.-f. Li, Y. Honda, H.-x. Liu, K.-i. Matsuda, M. Arita, T. Uemura, M. Yamamoto, Y. Miura, M. Shirai, T. Saito, F. Shi, and P. M. Voyles, Phys. Rev. B **89**, 014428 (2014).

[13] N. Tezuka, N. Ikeda, F. Mitsuhashi, and S. Sugimoto, Appl. Phys. Lett. **94**, 162504 (2009).

[14] T. Marukame, T. Ishikawa, T. Taira, K.-i. Matsuda, T. Uemura, and M. Yamamoto, Phys. Rev. B **81**, 134432 (2010).

[15] W. Wang, E. Liu, M. Kodzuka, H. Sukegawa, M. Wojcik, E. Jedryka, G. H. Wu, K. Inomata, S. Mitani, and K. Hono, Phys. Rev. B **81**, 140402(R) (2010).
[16] H.-x. Liu, T. Kawami, K. Moges, T. Uemura, M. Yamamoto, F. Shi and P. M. Voyles, J. Phys. D: Appl. Phys. **48**, 164001 (2015).
[17] K. Moges, Y. Honda, H.-x. Liu, T. Uemura, M. Yamamoto, Y. Miura, and M. Shirai, Phys. Rev. B **93**, 134403 (2016).
[18] K. Yakushiji, K. Saito, S. Mitani, K. Takanashi, Y. K. Takahashi, and K. Hono, Appl. Phys. Lett. **88**, 222504 (2006).
[19] T. Furubayashi, K. Kodama, H. Sukegawa, Y. K. Takahashi, K. Inomata, and K. Hono, Appl. Phys. Lett. **93**, 122507 (2008).
[20] Y. Sakuraba, K. Izumi, T. Iwase, S. Bosu, K. Saito, K. Takanashi, Y. Miura, K. Futatsukawa, K. Abe, and M. Shirai, Phys. Rev. B **82**, 094444 (2010).
[21] H. Narisawa, T. Kubota, and K. Takanashi, Appl. Phys. Express **8**, 063008 (2015).
[22] Y. Du, T. Furubayashi, T. T. Sasaki, Y. Sakuraba, Y. K. Takahashi, and K. Hono, Appl. Phys. Lett. **107**, 112405 (2015).
[23] T. Akiho, J. Shan, H.-x. Liu, K.-i. Matsuda, M. Yamamoto, and T. Uemura, Phys. Rev. B **87**, 235205 (2013).
[24] P. Bruski, Y. Manzke, R. Farshchi, O. Brandt, J. Herfort, and M. Ramsteiner, Appl. Phys. Lett. **103**, 052406 (2013).
[25] T. Saito, N. Tezuka, M. Matsuura, and S. Sugimoto, Appl. Phys. Express **6**, 103006 (2013).
[26] Y. Ebina, T. Akiho, H.-x. Liu, M. Yamamoto, and T. Uemura, Appl. Phys. Lett. **104**, 172405 (2014).
[27] T. Uemura, T. Akiho, Y. Ebina, and M. Yamamoto, Phys. Rev. B **91**, 140410(R) (2015).
[28] J. Kübler, A. R. Williams, and C. B. Sommers, Phys. Rev. B **28**, 1745 (1983).
[29] S. Ishida, S. Fujii, S. Kashiwagi, and S. Asano, J. Phys. Soc. Jpn. **64**, 2152 (1995).
[30] S. Picozzi, A. Continenza, and A. J. Freeman, Phys. Rev. B **66**, 094421 (2002).
[31] I. Galanakis, P. H. Dederichs, and N. Papanikolaou, Phys. Rev. B **66**, 174429 (2002).
[32] P. J. Webster, J. Phys. Chem. Solids **32**, 1221 (1971).

[33] M. Julliere, Phys. Lett. **54A**, 225 (1975).

[34] J. Mathon and A. Umerski, Phys. Rev. B **63**, 220403(R) (2001).

[35] W. E. Pickett and D. Singh, Phys. Rev. B **53**, 1146 (1996).

[36] S. Picozzi, A. Continenza, and A. J. Freeman, Phys. Rev. B **69**, 094423 (2004).

[37] I. Galanakis, K. Özdoğan, B. Aktaş, and E. Şaşıoğlu, Appl. Phys. Lett. **89**, 042502 (2006).

[38] B. Hülsen, M. Scheffler, and P. Kratzer, Phys. Rev. B **79**, 094407 (2009).

[39] K. Miyamoto, A. Kimura, Y. Miura, M. Shirai, M. Ye, Y. Cui, K. Shimada, H. Namatame, M. Taniguchi, Y. Takeda, Y. Saitoh, E. Ikenaga, S. Ueda, K. Kobayashi, and T. Kanomata, Phys. Rev. B **79**, 100405 (2009).

[40] T. Saito, T. Katayama, T. Ishikawa, M. Yamamoto, D. Asakura, T. Koide, Y. Miura, and M. Shirai, Phys. Rev. B **81**, 144417 (2010).

[41] Y. Miura, K. Abe, and M. Shirai, Phys. Rev. B **83**, 214411 (2011).

[42] R. Fetzer, J.-P. Wüstenberg, T. Taira, T. Uemura, M. Yamamoto, M. Aeschlimann, and M. Cinchetti, Phys. Rev. B **87**, 184418 (2013).

[43] M. Jourdan, J. Minár, J. Braun, A. Kronenberg, S. Chadov, B. Balke, A. Gloskovskii, M. Kolbe. H. J. Elmers, G. Schönhense, H. Ebert, C. Felser, and M. Kläui, Nat. Commun. **5**, 3974 (2014).

[44] R. Fetzer, B. Stadtmüller, Y. Ohdaira, H. Naganuma, M. Oogane, Y. Ando, T. Taira, T. Uemura, M. Yamamoto, M. Aeschlimann, and M. Cinchetti, Sci. Rep. **5**, 8537 (2015).

[45] J.-P. Wüstenberg, R. Fetzer, M. Aeschlimann, M. Cinchetti, J. Minár, Jürgen Braun, H. Ebert, T. Ishikawa, T. Uemura, and M. Yamamoto, Phys. Rev. B **85**, 064407 (2012).

[46] V. R. Singh, V. K. Verma, K. Ishigami, G. Shibata, A. Fujimori, T. Koide, Y. Miura, M. Shirai, T. Ishikawa, G. -f. Li, and M. Yamamoto, J. Appl. Phys. **117**, 203901 (2015).

[47] X. Kozina, J. Karel, S. Ouardi, S. Chadov, G. H. Fecher, C. Felser, G. Stryganyuk, B. Balke, T. Ishikawa, T. Uemura, M. Yamamoto, E. Ikenaga, S. Ueda, and K. Kobayashi, Phys. Rev. B **89**, 125116 (2014).

[48] R. Fetzer, S. Ouardi, Y. Honda, H.-x. Liu, S. Chadov, B. Balke, S. Ueda, M. Suzuki, T. Uemura, M. Yamamoto, M. Aeschlimann, M. Cinchetti, G. H. Fecher, and C. Felser, J. Phys. D: Appl. Phys. **48**, 164002 (2015).

[49] D. Asakura, T. Koide, S. Yamamoto, K. Tsuchiya, T. Shioya, K. Amemiya, V. R. Singh, T. Kataoka, Y. Yamazaki, Y. Sakamoto, A. Fujimori, T. Taira, and M. Yamamoto, Phys. Rev. B **82**, 184419 (2010).

[50] V. R. Singh, V. K. Verma, K. Ishigami, G. Shibata, T. Kadono, A. Fujimori, D. Asakura, T. Koide, Y. Miura, M. Shirai, G.-f. Li, T. Taira, and M. Yamamoto, Phys. Rev. B **86**, 144412 (2012).

[51] S. Ouardi, G. H. Fecher, S. Chadov, B. Balke, X. Kozina, C. Felser, T. Taira, and M. Yamamoto, Applied Physics A: Materials Science & Processing **111**, 395 (2013).

[52] S. Zhang, P. M. Levy, A. C. Marley and S. S. P. Parkin, Phys. Rev. Lett. **79**, 3744 (1997).

[53] C. H. Shang, J. Nowak, R. Jansen, and J. S. Moodera, Phys. Rev. B **58**, 2917 (1998).

[54] X.-F. Han, A. C. C. Yu, M. Oogane, J. Murai, T. Daibou, and T. Miyazaki, Phys. Rev. B **63**, 224404 (2001).

[55] V. Drewello, J. Schmalhorst, A. Thomas, and G. Reiss, Phys. Rev. B **77**, 014440 (2008).

[56] R. Shan, H. Sukegawa, W. H. Wang, M. Kodzuka, T. Furubayashi, T. Ohkubo, S. Mitani, K. Inomata, and K. Hono, Phys. Rev. Lett. **102**, 246601 (2009).

[57] S. S. P. Parkin, C. Kaiser, A. Panchula, P. M. Rice, B. Hughes, M. Samant, and S.-H. Yang, Nat. Mater. **3**, 862 (2004).

[58] T. Marukame and M. Yamamoto, J. Appl. Phys. **101**, 083906 (2007).

[59] A. A. Khan, J. Schmalhorst, G. Reiss, G. Eilers, M. Münzenberg, H. Schuhmann and M. Seibt, Phys. Rev. B **82**, 064416 (2010).

[60] V. Drewello, D. Ebke, M. Schäfers, Z. Kugler, G. Reiss, and A. Thomas, J. Appl. Phys. **111**, 07C701 (2012).

[61] D. Bang, T. Nozaki, D. D. Djayaprawira, M. Shiraishi, Y. Suzuki, A. Fukushima, H. Kubota, T. Nagahama, S. Yuasa, H. Maehara, K. Tsunekawa, Y. Nagamine, N. Watanabe, and H. Itoh, J. Appl. Phys. **105**, 07C924 (2009).

[62] Q. L. Ma, S. G. Wang, J. Zhang, Y. Wang, R. C. C. Ward, C. Wang, A. Kohn, X.-G. Zhang, and X. F. Han, Appl. Phys. Lett. **95**, 052506 (2009).

[63] M. Belmoubarik, H. Sukegawa, T. Ohkubo, S. Mitani, and K. Hono, Appl. Phys. Lett. 132404 (2016).

[64] R. Stratton, J. Phys. Chem. Solids **23**, 1177 (1962).

[65] J. G. Simmons, J. Appl. Phys. **34**, 1793 (1963).

[66] T. Marukame, T. Ishikawa, W. Sekine, K. Matsuda, T. Uemura, and M. Yamamoto, IEEE Trans. Magn. **42**, 2652 (2006).

[67] S. Yuasa, T. Nagahama, A. Fukushima, Y. Suzuki, and K. Ando, Nat. Mater. **3**, 868 (2004).

[68] W. H. Butler, X.-G. Zhang, T. C. Schulthess, and J. M. MacLaren, Phys. Rev. B **63**, 054416 (2001).

[69] Y. Miura, H. Uchida, Y. Oba, K. Nagao, and M. Shirai, J. Phys.: Condens. Matter **19**, 365228 (2007).

[70] S. Trudel, O. Gaier, J. Hamrle, and B. Hillebrands, J. Phys. D: Appl. Phys. **43**, 193001 (2010).

Appendix

Publication list

1. Publications related to this dissertation

1. Bing Hu, Kidist Moges, Yusuke Honda, Hong-xi Liu, Tetsuya Uemura, Masafumi Yamamoto, Jun-ichiro Inoue, and Masafumi Shirai, "Temperature dependence of spin-dependent tunneling conductance of magnetic tunnel junctions with half-metallic Co_2MnSi electrodes", Phys. Rev. B, vol. 94, 094428 (15pp), 2016.
2. B. Hu, Kidist. Moges, H. Liu, Y. Honda, T. Uemura and M. Yamamoto, "Temperature Dependence of Spin-Dependent Tunneling Conductance of Magnetic Tunnel Junctions with Highly Spin-Polarized Electrodes", 2015 International Conference on Solid State Devices and Materials (SSDM 2015), Extended Abstracts (USB memory), PS-12-6 (2pp), Sapporo, Japan, Sep. 28−30, 2015.
3. B. Hu, H. Liu, T. Kawami, Kidist Moges, Y. Honda, T. Uemura and M. Yamamoto, "Temperature dependence of spin-dependent tunneling resistances of Co_2MnSi-based and $Co_2(Mn,Fe)Si$-based magnetic tunnel junctions showing high tunneling magnetoresistances", IEEE International Magnetics Conference 2015 (Intermag 2015), Digests (USB Memory), GB-11 (2pp), Beijing, China, May 11−15, 2015.

2. Publications related to other research

1. Z. Yang, H. Qiu, B. Hu, G. Zou, "Structural and electrical properties of Ni films sputter-deposited on HCl-doped polyaniline substrates", Vacuum, vol. 99, 192 (4pp), 2014.
2. Y. Cao, R. Huang, B. Hu, H. Qiu, J. He, "Structural and electrical properties of Ag films sputter-deposited on HCl-doped and undoped polyaniline substrates", Mater. Chem. and Phys., vol. 143, 788 (6pp), 2014.

3. Presentations related to this dissertation

1. B. Hu, Kidist. Moges, H. Liu, Y. Honda, T. Uemura and M. Yamamoto, "Temperature Dependence of Spin-Dependent Tunneling Conductance of Magnetic Tunnel Junctions with Highly Spin-Polarized Electrodes", 2015 International Conference on Solid State Devices and Materials (2015).
2. B. Hu, H. Liu, T. Kawami, Kidist Moges, Y. Honda, T. Uemura and M. Yamamoto, "Temperature dependence of spin-dependent tunneling resistances of Co_2MnSi-based and Co_2(Mn,Fe)Si-based magnetic tunnel junctions showing high tunneling magnetoresistances", IEEE International Magnetics Conference 2015 (2015).
3. B. Hu, Kidist Moges, Y. Honda, T. Uemura, and M. Yamamoto, "Correlation between the temperature dependence of tunneling conductance of Co_2MnSi-based MTJs and their half-metallicity", 51st Conference of Hokkaido Chapter, The Japan Society of Applied Physics (2016).
4. B. Hu, Kidist Moges, Y. Honda, T. Uemura, M. Yamamoto, "Temperature dependence of spin-dependent tunneling conductance for the parallel configuration of Co_2MnSi and Co_2(Mn,Fe)Si-based MTJs", 157th Fall Annual Meeting 2015, The Japan Institute of Metals and Materials (2015).
5. B. Hu, Kidist Moges, H. Liu, Y. Honda, T. Uemura, and M. Yamamoto, "Temperature dependence of spin-dependent tunneling conductance for parallel configuration of Co_2MnSi MTJs with high spin polarization", 76th Autumn Meeting 2015, The Japan Society of Applied Physics (2015).

6. B. Hu, K. Moges, Y. Honda, T. Uemura, M. Yamamoto, "Characteristic temperature dependence of spin-dependent tunneling conductance of MTJs with highly spin-polarized electrodes", 39th Annual Conference on MAGNETICS in Japan (2015).
7. B. Hu, H. Liu, T. Kawami, K. Moges, T. Uemura, and M. Yamamoto, "Temperature dependence of spin-dependent tunneling resistances of Co_2MnSi and $Co_2(Mn,Fe)Si$ MTJs showing high tunneling magnetoresistances", 62nd Spring Meeting 2015, The Japan Society of Applied Physics (2015).